SAPIENZA
UNIVERSITÀ DI ROMA

# Simulation and tests of a new MicroMegas detector for the PADME experiment

Facoltà di Scienze Matematiche Fisiche e Naturali
Corso di Laurea Magistrale in Fisica


Candidate
Davide Quaranta
ID number 1895475

Thesis Advisor
Prof. Mauro Raggi

Co-Advisor
Dott.ssa Giada Mancini


Academic Year 2023/2024

Thesis defended on 28 October 2024
in front of a Board of Examiners composed by:

Prof. Roberto di Leonardo (chairman)
Prof. Claudio Conti
Prof. Giovanni Organtini
Prof. Francesco Zamponi
Prof. Marco Drago
Prof. Ugo Giuseppe Aglietti
Prof. Fabio Columbro

---

**Simulation and tests of a new MicroMegas detector for the PADME experiment**
Master's thesis. Sapienza – University of Rome



This thesis has been typeset by LaTeX and the Sapthesis class.

Author's email: quarantadavide16@gmail.com

## Abstract

The existence of Dark Matter is a long-standing open question in particle physics. For decades, the attention of the particle physics community has been focused on the WIMP model. This model interprets dark matter as being composed of massive particles with a mass between 1 and 100 GeV, which interact weakly with ordinary matter. Despite extensive efforts, no WIMPs have yet been observed so far, prompting the particle physics community to explore alternative dark matter models. One notable model is the Dark Sector scenario. In this framework, Standard Model (SM) particles and Dark Matter (DM) particles belong to two "separate worlds" that can interact with each other only through a so called "portal": a particle charged under both Standard Model and Dark Matter interactions. The "$X_{17}$ anomaly," as it is called, is currently one of the most interesting pieces of evidence for the existence of a new particle. The introduction of a new light neutral boson, with a mass around 17 MeV, called X17, can explain a series of anomalous observations made by the ATOMKI collaboration. These observations were made during their study of the multipolarity of Internal Pair Creation (IPC) nuclear transitions in $^{8}$Be, $^{4}$He, and $^{12}$C nuclei. In the decay of the nucleus, such a particle would be produced and subsequently decay into an $e^+e^-$ pair. However, almost a decade after the anomaly was first reported, the ATOMKI results have remained untested by other experiments. PADME has the unique opportunity to produce $X_{17}$ at resonance, through positron annihilation on a diamond target, due to the peculiar properties of the *Beam Test Facility* (BTF) in *Frascati National Laboratories* (LNF). For Run IV, PADME plans to upgrade the experimental apparatus with a tracker with high tagging efficiency, to distinguish neutral from charged final states. This allows to test the existence of $X_{17}$ through the ratio of the number of $e^+e^-$ final state events to the number of annihilations to a photon pair. This thesis will provide an account of the work carried out by the PADME collaboration with the help of the LNF Atlas Group, to construct and test the new detector. Chapter 1 starts by introducing the Dark Matter problem, outlining the WIMP paradigm and the Dark Sector alternative, with particular attention to the Dark Photon model. Subsequently, the $X_{17}$ anomaly will be then introduced, and a summary of the current status of ATOMKI results will be presented. In Chapter 2, an overview of the PADME experiment will be provided, including a description of its principal components and the search for $X_{17}$ that was conducted during Run III. The chapter concludes with an examination of the rationale behind the necessity of a tracker for the forthcoming PADME Run IV. A review of gaseous detectors and their operational principles can be found in Chapter 3, with particular focus on Micromegas detectors, which is the technology selected for the upgrade of the PADME apparatus. Chapter 4 will describe the experimental apparatus and tests carried out at LNF-BTF with the objective of studying the performance of the PADME tracker prototype. In Chapter 5, the development of a comprehensive GEANT4 simulation of the PADME Micromegas

is described, from the definition of the geometry to data-driven digitization. The chapter concludes with a discussion of the detector's spatial and angular resolution, as well as its capability for vertex reconstruction, based on Monte Carlo simulations.

# Contents

# Chapter 1

# Dark matter and dark sectors

The purpose of this chapter is to provide a general introduction to the problem of dark matter existence. Specifically, the two main current models will be described: the Weakly Interacting Massive Particle (WIMP) model and the Dark Sector model. Subsequently, the so-called "ATOMKI Anomaly" will be described. This concerns anomalous excesses in nuclear physics observables, which are consistent with the existence of a new neutral particle called X17. The role of X17 as a mediator in a dark sector-type theory will be examined, along with the properties this particle should possess to explain the results of these observations.

## 1.1 The dark matter problem

The nature of dark matter has been and continues to be one of the main open questions in particle physics. Its existence finds support in many experimental observations, especially in the context of astrophysics and cosmology. The first hint of the presence of a non-visible form of matter emerged in 1933 when Fritz Zwicky observed an anomaly in the dispersion velocity of galaxies within the Coma Cluster [1]. Later on, in 1980, Vera Rubin et al. reconsidered the hypothesis to account for the unexpected observations regarding the rotational velocity of galaxies [2]. The classical law of gravitation predicts that the rotational velocity of an object around the galactic centre increases linearly with the distance R as a consequence of Gauss' Theorem, as long as $R < R_0$, where $R_0$ is the radius of the galactic core. Conversely, when $R > R_0$, the rotational velocity is expected to have a $\sqrt{1/R}$ behaviour. However, measurements revealed an asymptotically constant velocity, which could be explained by the postulation of the presence of an additional source of mass surrounding visible matter, known as the "dark halo". Figure 1.1 shows an example of a rotational curve for the galaxy NGC 3198, in the Ursa Major constellation. These initial investigations indicated that dark matter interacts via the gravitational force but not under the electromagnetic force. In fact, if it did, it would emit radiation (X-rays, $\gamma$-rays,...), detectable by our telescopes.

Additional evidence for the existence of dark matter comes from gravitational

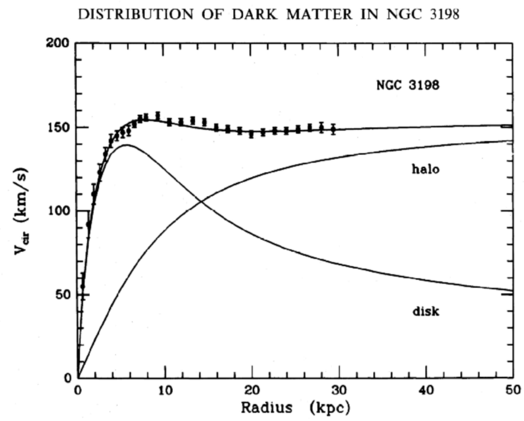


**Figure 1.1.** Rotational velocity as a function of the distance from the galactic center for the NGC 3198 galaxy. The solid line labeled "disk" represents the curve expected from the mass distribution inferred from the galaxy's luminosity. The solid line labeled "halo" represents the necessary contribution from the dark matter cloud surrounding the galaxy that would explain the experimental data (markers with error bars).

lensing. Gravitational lensing is an effect predicted by the general theory of relativity. According to this theory, massive objects can warp the structure of spacetime (more technically, the metric tensor changes) in such a way that light bends when passing near them. A schematic representation of this phenomenon is shown in Figure 1.2a. The path of the light coming from a source object, is deviated by an angle $\alpha$ as it travels towards an observer, owing to the presence of an heavy object in between them. Therefore, the observer perceives this light as coming from a different direction than the original one. The deflection angle depends both on the "lens" mass $M$ and on the impact parameter $b$ and is approximately equal to :

$$\alpha = \frac{4GM}{c^2 b} \tag{1.1}$$

with $c$ and $G$ being the speed of light and the gravitational constant. The study of gravitational lensing allows astronomers to compute the amount of mass in a particular region of space by measuring the distortion of the light coming from objects behind it. Discrepancies between the mass estimated from luminosity and that derived from gravitational lensing further support the hypothesis of invisible matter [3]. Other gravitational effects, such as those observed in the Bullet Cluster, lends additional support to this evidence [4].

In the field of cosmology, studying the expansion of the Universe provides insights into its composition. The connection between these two quantities is established through the Friedmann equation, which, in the case of a flat Universe, can be expressed as:

$$\frac{H(t)}{H(now)} = \Omega_{matter} + \Omega_{radiation} + \Omega_{dark\ energy} \tag{1.2}$$

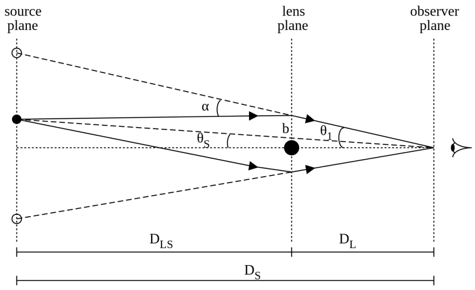


**(a)**

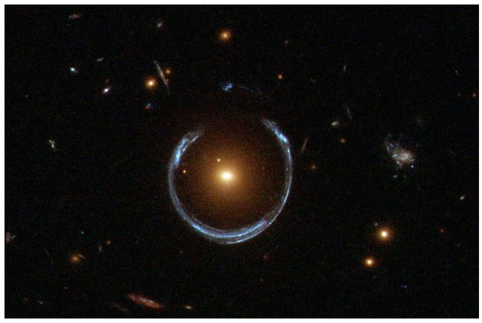

**(b)**

**Figure 1.2.** (Left) Schematic representation of gravitational lensing. A mass (lens) between an observer and a source bends the light coming from it by an angle $\alpha$. (Right) The "Einstein ring" phenomenon, a type of strong gravitational lensing which happens when two galaxies are almost perfectly aligned.

Here H represents the Hubble constant which embodies the information about the Universe expansion, while $\Omega$ indicates the fraction of energy present in the Universe that comes in a particular form; in our case for example, in the form of matter, radiation, and dark energy through the cosmological constant $\Lambda$. Clearly, if we evaluate Equation 1.2 at the present time, the sum of the energy fractions should sum up to 1:

$$1 = \Omega^0_{matter} + \Omega^0_{rad} + \Omega^0_{\Lambda} \tag{1.3}$$

where the superscript 0 indicates a quantity evaluated at the present moment. Measurements of the supernovae redshift allowed to estimate the present-day content of the Universe as $\Omega^0_m = 30\%$ and $\Omega^0_\Lambda = 70\%$ with a negligible contribution from $\Omega^0_{rad}$. However this is in contrast with various experiments, such as those analysing the Cosmic Microwave Background (CMB) temperature fluctuations, that estimated the Universe's baryonic matter fraction as $\Omega^0_b = 5\%$ [5]. Dark matter is believed to represent the missing $25\%$ and must therefore be non-baryonic.

Additionally, dark matter is expected to be mainly *cold*, namely non-relativistic, as inferred by analyses on matter density power spectra, including studies of CMB anisotropies and weak lensing maps [6]. Despite substantial evidence supporting the existence of dark matter, its composition remains a mystery. In the following, we briefly review the two main theoretical frameworks proposed to explain the nature of Dark Matter: the *Weakly Interacting Massive Particles* model (WIMP) and the Dark Sector model (DS). While other hypotheses exist, they are beyond the scope of this thesis.

### 1.1.1 The WIMP miracle

There is no precise definition of what a WIMP is, but the name suggests that the term is used to indicate particles that interact through the weak interaction of the Standard Model, or more generally with a coupling of the same order $g \sim 1$, and a

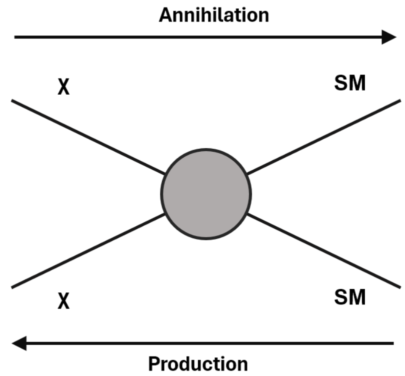


**Figure 1.3.** Scheme of processes affecting the dark matter number density. Following the arrow from left to right we have annihilation of dark matter into SM particles while, following the arrow from right to left we have dark matter production from SM particles' annihilation.

mass between $\sim$ 10 GeV to 10 TeV. The WIMP model has dominated dark matter searches for decades mainly for two reasons:

1. It could be addressed using well-established experimental techniques in the particle physics world.
2. It could explain the DM relic density obtained from cosmological observations using a language that was very familiar to the particle physics theoretical community.

In the early stages of the Universe Dark Matter ($\chi$) and SM particles were in thermal equilibrium and the annihilation process $\chi\chi \to$ SM SM compensated the production process SM SM $\to \chi\chi$ (see Figure 1.3). The rate of change in the number density of dark matter particles can be described using the Boltzmann equation [7]:

$$\frac{dn}{dt} = -3Hn - \langle\sigma_A v\rangle \left(n^2 - n_{\text{eq}}^2\right) \tag{1.4}$$

The first term contains the Hubble constant $H$ and is due to the Universe expansion which causes the number of particles per unit volume to decrease. The second term plays the role of a "feedback" term, causing $n$ to decrease if it is higher than the equilibrium density $n_{eq}$ and vice versa. The quantity $\langle\sigma_A v\rangle$ represents the velocity averaged dark matter annihilation cross section. The equilibrium condition is maintained until the interaction rate and the expansion rate become equal $n\,\langle\sigma_A v\rangle = H$, a phase known as *decoupling*. After this moment, dark matter particles cease to interact with one another because the expansion is too fast for them to find each other and annihilate. In the hypothesis that decoupling happened in the radiation dominated era:

$$H^2(t_{dec}) \simeq \frac{8\pi G}{3c^2}\varepsilon(t_{dec}) \sim \frac{T_{dec}^4}{M_{Pl}^2} \quad \Longrightarrow \quad n_{dec} \sim \frac{T_{dec}^2}{M_{Pl}\,\langle\sigma_A v\rangle} \tag{1.5}$$

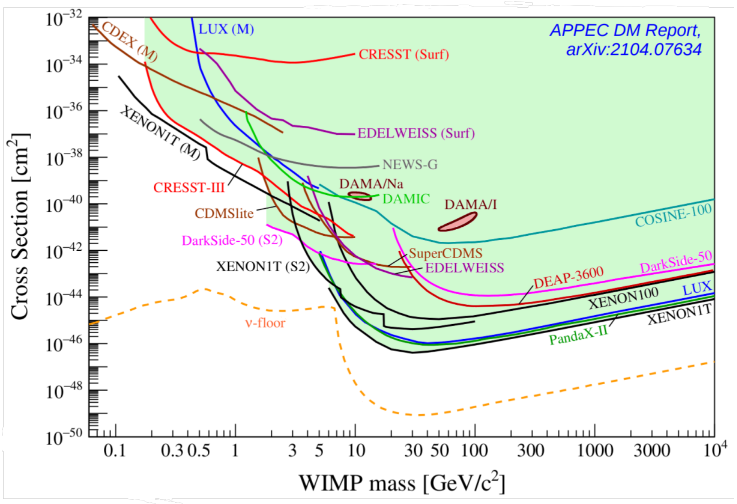


**Figure 1.4.** Exclusion plot for the WIMP parameter space. The green shaded area has been excluded. The orange dashed line indicates the irreducible neutrino floor background.

where $\varepsilon$ is the radiation energy density and $M_{Pl} = \sqrt{\hbar c/G}$ is the Planck mass. Since we said that WIMPs interact weakly, a rough order-of-magnitude estimate of the cross section is:

$$\sigma_A = G_F^2 M_X^2 \tag{1.6}$$

where $M_X$ is the WIMP mass and $G_F \approx 1.17 \times 10^{-5}$ GeV$^{-2}$ is the Fermi constant. Equation 1.6 shows that by tuning the mass of the dark matter particle, we can reproduce the number density at decoupling predicted by cosmology, this is the "WIMP miracle": a particle with a mass between 100 GeV and 1 TeV could account for all the dark matter. A great deal of effort has been dedicated over the years to probe the WIMP parameter space both in mass and cross section as can be seen in Figure 1.4. Experiments like DarkSide and XENON have placed dominant constraints on the high mass region, excluding cross sections as low as $10^{-46}$cm$^2$, while the CRESST experiment has provided the best upper limit in the low mass region. However, at the present moment, no WIMP signal has been found.

### 1.1.2 The dark sector paradigm

In light of the lack of promising outcomes from the ongoing investigations into WIMPs, there has been a resurgence of interest in exploring the potential of light dark matter (LDM) candidates. A broad range of models in this direction are the so called "Dark Sector" theories, wherein DM comprises a whole set of particles that are neutral under the Standard Model (SM) interactions but charged under a new "hidden" force. The connection between these two worlds would be represented by a mediator particle serving as a "portal" to the hidden sector. This particle would be charged under both at least one Stardard Model interaction and the new “dark force”, allowing dark sector particles to interact with Standard Model ones. Dark sectors theories are classified based on the type of mediator, some possibilities are the following [8]:

- Scalar mediator: A spin-0 particle could interact with the Higgs boson through three and four-fields operators:
$$\mathcal{L} \supset \mu S H^\dagger H + \lambda S^2 H^\dagger H \tag{1.7}$$

- Pseudoscalar mediator: a particle like the axion could interact with photons and fermions through:
$$\mathcal{L} \supset g_{a\gamma\gamma} \frac{\alpha}{2\pi} \frac{a}{f_a} F^{\mu\nu} \tilde{F}_{\mu\nu} + g_{aff} \frac{\partial_\mu a}{f_a} \bar{\psi}_f \gamma^\mu \gamma_5 \psi_f \tag{1.8}$$

- Neutrino mediator: a sterile neutrino, singlet under all the SM gauge groups, allows the Yukawa term:
$$\mathcal{L} \supset Y_N L H N \tag{1.9}$$

- Vector portal: a neutral vector particle $A'$ can interact with SM fermions via the following term:
$$\mathcal{L} \supset g' q_f \bar{\psi}_f \gamma_\mu \psi_f A'_\mu \tag{1.10}$$
where $g'$ is the coupling of the new interaction and $q_f$ is the charge of the fermions.

### 1.1.3 The vector portal: the dark photon

In the vector scenario, by analogy with the usual QED interaction term, the mediator $A'$ is also referred to as *dark photon*. This model will be the main focus of the following discussion due to its popularity in low-energy experiments and thorough study. One of the ways to introduce the dark photon is to postulate the existence of an additional $U(1)_D$ symmetry, responsible for the interaction between dark sector particles. Then the most general gauge-invariant Lagrangian that can be written includes a kinetic mixing term:

$$\mathcal{L} \supset \frac{1}{2} \frac{\epsilon}{\cos\theta_W} F'_{\mu\nu} B^{\mu\nu} \tag{1.11}$$

where $F'_{\mu\nu}$ and $B^{\mu\nu}$ are the dark photon and SM hypercharge field strengths, and $\theta_W$ is the weak mixing angle. A term of this kind is connected to a diagram like the one depicted on the left side of Figure 1.5. In an EFT approach this diagram can be obtained after integrating out the fields in the loop diagram on the right of Figure 1.5, giving us an estimate of the mixing parameter $\epsilon$:

$$\epsilon \sim \frac{g_Y g_D}{16\pi^2} \log\left(\frac{m_\Psi}{m_{\Psi'}}\right) \tag{1.12}$$

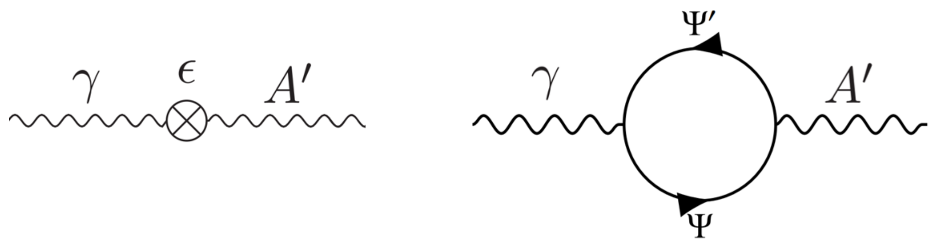


**Figure 1.5.** Left: effective interaction between dark photon $A'$ and SM photon. Right: interaction between dark photon and SM photon at the loop level.

where $\Psi$ and $\Psi'$ are a doublet of heavy fields charged under both $U(1)_Y$ and $U(1)_D$. The generation of the mixing at the loop level makes the mixing parameter naturally small. Despite its simplicity, the dark photon model can provide an explanation for several anomalous effects observed in the last few years. Among them we recall the excess of positron flux in cosmic rays by AMS-02, the gamma-ray emission spectrum from the Galactic Center by the Fermi Large Area Telescope and the anomalous magnetic moment of the muon.

### 1.1.4 Dark photon production

Starting from ordinary matter, the dark photon $A'$ can be produced via different channels:

- **Resonant production** ($e^+e^- \to A'$): in this process a particle-antiparticle, for example $e^+e^-$, annihilate and produce a dark photon (see Figure 1.6a). The cross section is proportional to $\epsilon^2\alpha$, in particular it follows a Breit-Wigner distribution [9]:

$$\sigma_{\text{res}} = \sigma_{\text{peak}} \frac{\Gamma_{A'}^2/4}{(\sqrt{s}-m_{A'})^2 + \Gamma_{A'}^2/4} \tag{1.13}$$

  where $\sigma_{\text{peak}} = 12\pi/m_{A'}^2$ is the cross-section at $m_{A'}$, and $\Gamma_{A'} = \frac{1}{2}m_{A'}\epsilon^2\alpha$ is the $A'$ width in the limit in which $m_e/m_{A'} \to 0$; this expression holds only if $A'$ is stable enough to be considered a particle, namely if $\Gamma_{A'}/m_{A'} \ll 1$, which is verified since $\epsilon \ll 1$.

- **Associated production** ($e^+e^- \to \gamma A'$) : this process happens via a t-channel diagram, proportional to $\epsilon^2\alpha^2$ (see Figure 1.6b). The differential cross section can be written as [9]:

$$\frac{d\sigma_{\text{nores}}}{dz} = \frac{4\pi\epsilon^2\alpha^2}{s}\left(\frac{s-m_{A'}^2}{2s}\frac{1+z^2}{1-\beta^2z^2} + \frac{2m_{A'}^2}{s-m_{A'}^2}\frac{1}{1-\beta^2z^2}\right) \tag{1.14}$$

where $z$ is the cosine of the angle between the $A'$ direction in the center of mass frame and the direction of the boost to the laboratory frame. In this reference frame $A'$ and the photon are produced back to back with a strongly forward/backward peaked angular distribution as can be seen from Equation 1.14. After boosting to the laboratory frame, the angular distribution of the dark photon is peaked in the forward direction, the more the larger the $A'$ mass value.

- **Bremsstralhung** ($e^- Z \to e^- Z\gamma$) : an electron scatters off a nucleus end then emits a dark photon. The emission can happen both as initial or final state radiation, shown respectively in Figure 1.7a and Figure 1.7b. The formula for the energy-angle cross section can be found using the Weiszsacker-Williams approximation, in which the scattering is treated as a Compton-like process. If the additional condition $m_e \ll m_{A'}$ holds, the result is [9]:

$$\frac{d\sigma}{dx} = \frac{8\alpha^3\epsilon^2\sqrt{1 - m_{A'}^2/E_0^2}}{m_{A'}^2(1-x)/x + m_e^2 x}\left(1 - x + \frac{x^2}{3}\right)\Phi \tag{1.15}$$

  where $x = E_{A'}/E_0$ is the fraction of the electron energy carried away by the dark photon and $\Phi$ is a function that parametrizes the structure of the nucleus. This process has the same coupling dependance of the associated production, with an additional suppression of $\alpha/m_{A'}^2$. The cross section has a maximum for $x \sim 1$, so the most favourable configuration is the one in which the emitted $A'$ carries away most of the beam energy.

- **Meson decays** : the dark photon can be produced in the decays of charged or neutral pseudoscalar (P) or vector (V) mesons for example $\pi^0 \to \gamma A'$ (shown in Figure 1.8a), $V^\pm \to \pi^\pm A'$, and $P^\pm \to \pi^\pm A'$. Due to its $m_{A'}^2$ dependance, the last process can only happen for a massive dark photon. The expression for the branching fraction of any of the mentioned channel can be computed by replacing $A_{\prime}$ with a photon in the final state and then correcting for the right phase space factor. For example in the case of a vector particle:

$$\begin{aligned} &\mathrm{BR}\left(V^\pm \to P^\pm A'\right) = \\ &\epsilon^2 \mathrm{BR}\left(V^\pm \to P^\pm \gamma\right) \frac{\left(m_V^2 - m_{A'}^2 - m_P^2\right)\sqrt{\left(m_V^2 - m_{A'}^2 + m_P^2\right)^2 - 4m_V^2 m_P^2}}{\left(m_V^2 - m_{A'}^2\right)^3} \end{aligned} \tag{1.16}$$

- **Drell-Yan process** ($q\bar{q} \to l^+ l^-$): a quark-antiquark pair annihilates into an $A'$ which subsequently decays into a lepton-antilepton pair (see Figure 1.8b). The "hard" quark-antiquark cross section will have an expression similar to Equation 1.13, but it needs to be multiplied by the branching ratio of $A'$ into the particular final state under consideration. Furthermore the coupling needs to be modified because of the fractional charge of quarks and the presence color factor. The hadronic cross section, eventually, also has to take into account the parton density function of the quark family that initiated the process.

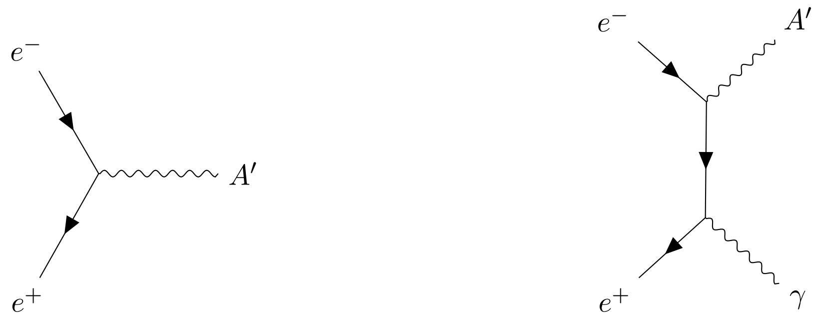


**(a)** **(b)**

**Figure 1.6.** (a) Feynman diagram for the resonant production of the dark photon $A'$. (b) Feynman diagram for the associated production process.

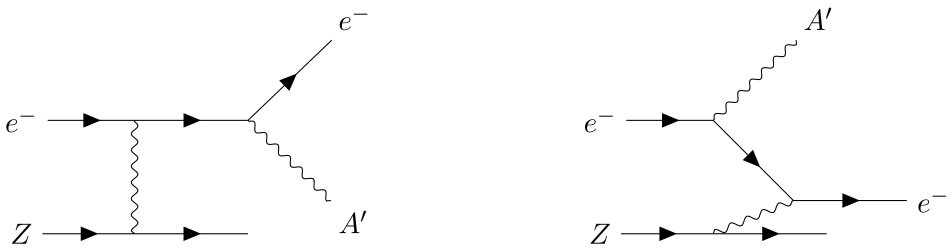


**(a)** **(b)**

**Figure 1.7.** Diagram showing electron Bremsstralhung with the emission an $A'$ as initial (a) of final (b) state radiation.

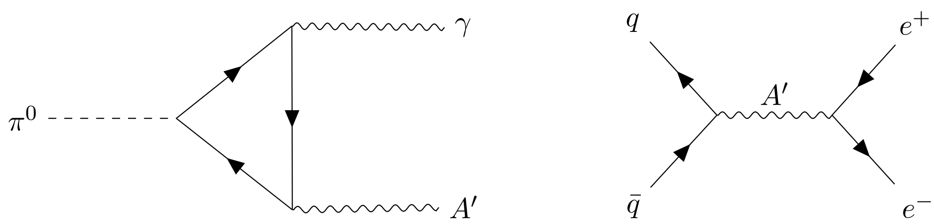


**(a)** **(b)**

**Figure 1.8.** (a) Feynman diagram for the production of $A'$ through meson decays, in particular for the case of a neutral pion (b) Diagram showing a Drell-Yan process mediated by the dark photon $A'$.

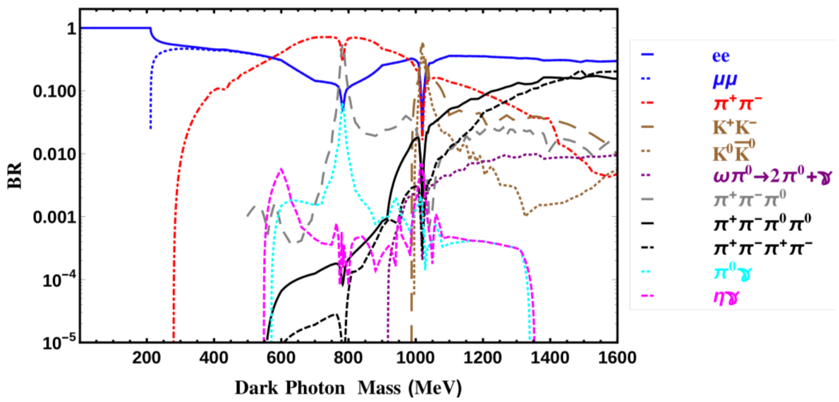


**Figure 1.9.** Branching ratios of dark photon for different channels as a function of its mass. Figure taken from [9].

### 1.1.5 Dark photon decays

In order to detect the dark photon, we need to use its decay channels, which are strictly connected to its mass hierarchy compared to dark fermions $\chi$. If $m_{A'} < 2m_{\chi}$, the decay to dark sector particles $\chi$ is kinematically forbidden and can only happen to SM particles. We will refer to this scenario as "visible decays". The partial width of the decay to SM particles is given by:

$$\Gamma_{A'\to l^+l^-} = \frac{1}{3}\alpha\epsilon^2 M_{A'}\sqrt{1-\frac{4m_l^2}{M_{A'}^2}}\left(1+\frac{2m_l^2}{M_{A'}^2}\right) \tag{1.17}$$

for a lepton/antilepton final state, while for hadrons it can be written as:

$$\Gamma_{A'\to \text{ had}} = \frac{1}{3}\alpha\epsilon^2 M_{A'}\sqrt{1-\frac{4m_\mu^2}{M_{A'}^2}}\left(1+\frac{2m_\mu^2}{M_{A'}^2}\right)\times\frac{\Gamma\left(e^+e^-\to \text{ hadrons }\right)}{\Gamma\left(e^+e^-\to\mu^+\mu^-\right)}\left(E=M_{A'}\right) \tag{1.18}$$

Different channels open up as the mass of $A'$ increases contributing to the total width, as depicted in Figure 1.9. If the dark photon exists, its signature would be a peak in the invariant mass of its decay products on top of the background, at the value $m_{A'}$. The proper lifetime of the decay into SM particles is given by:

$$c\tau = \frac{1}{\Gamma} = \frac{3}{N_{eff}m_{A'}\alpha\epsilon^2} \sim \frac{80\mu\text{m}}{N_{eff}}\left(\frac{10^{-4}}{\epsilon}\right)^2\left(\frac{100\text{MeV}}{m_{A'}}\right) \tag{1.19}$$

where $N_{eff}$ is the number of available decay channels for a specific value of the dark photon mass. For example $N_{eff} = 1$ if $m_{A'} < 2m_\mu$, while for $m_{A'} >= 2m_\mu$ the number of channels is $N_{eff} = 1 + R(m_{A'})$, and $R$ is the ratio between the cross section of $e^+e^-$ into hadrons and the one into $\mu^+\mu^-$. From Equation 1.19 we notice the dependance of the decay length on $\epsilon^2$, which allows the identification of a dark photon also looking for a displaced decay vertex in the small coupling region.

Alternatively, if $m_{A'} > m_{\chi\chi}$, the decay can happen via invisible channels, thus escaping detection. In such a case no invariant mass of the decay products of $A'$ can be measured, however the mass of $A'$ can still be inferred by missing energy/momentum techniques in kinematically constrained final states. If a dark photon exists a resonant signal on top of a smooth continuous background should be observed. The main challenge of this approach is the very high background rejection needed to exclude accidental spurious signals, for example final state SM particles escaping detector acceptance.

## 1.2 The X17 Anomaly

Starting from 2016 a research group of the ATOMKI laboratories, based in Debrecen, Hungary, published a series of results pointing out a high-significance anomaly in the proton capture reaction $^7\mathrm{Li}(p, e^+e^-)^8\mathrm{Be}$. The unexpected signal was an excess in the relative angle distribution between the electron and the positron originating from IPC decay of $^8$Be. One possible explanation for the observed data was the production and subsequent decay of a neutral boson with a mass of approximately 17 MeV, which has been referred to as X17. It has to be neutral because it decays to $e^+e^-$ and it has to be a boson because it is emitted in the transition between two levels with integer angular momentum $J$. This new light particle is one of the most promising candidates for new physics to emerge in recent years and has renewed interest towards dark sector-like theories. The experiment has recently been repeated with different nuclei and improved experimental equipment, confirming the anomaly's presence. This section provides an overview of the experiment and summarizes the collaboration's various results.

### 1.2.1 Introduction to IPC

When a nucleus is in an excited state, it usually decays to a lower energy state by emitting a photon, a process known as $\gamma$ decay. To respect the conservation of energy, the emitted photon needs to have an energy equal to the difference between the initial and final states energies of the decaying nucleus. However, more rarely, the nucleus de-excites by emitting a virtual photon, which then converts into an electron-positron pair; this process is called *Internal Pair Creation* (IPC). Such decay is only possible if the energy of the transition is at least $2m_e$, otherwise there is not enough energy to produce the two leptons in the final state. IPC transitions follow certain selection rules, based on the parity and the angular momentum $\ell$ carried away by the emitted photon. In particular, they can be divided into two cateogories: $E\ell$-type transitions (electric) and $M\ell$-type transitions (magnetic). Electric transition are related to changes in the charge density of the nucleus and change the parity by $(-1)^\ell$. Magnetic transitions, on the other hand, are connected to the current density of the nucleus carrying a change in parity of $(-1)^{\ell+1}$.

Let's consider for example the $^8$Be nucleus: Figure 1.10 shows the $^8$Be lowest energy levels, and represents with a red arrow the 17.64 MeV and 18.15 MeV

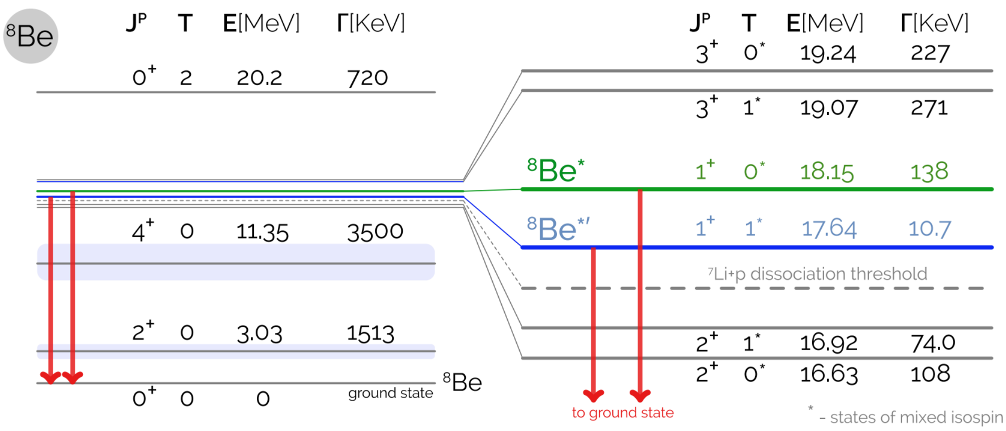


**Figure 1.10.** First levels of the $^8$Be nucleus. Red arrows represent the transitions at 17.64 MeV and 18.15 MeV to the ground state, which were studied in the first experiment by ATOMKI, where the anomaly was discovered. For each transition the spin-parity $J^P$, the isospin $T$, the energy and the width are reported.

transitions to ground state, the first studied at ATOMKI, in which the anomaly was observed. Both transitions occur between a level with spin-parity $J^P = 1^+$ and the $J^P = 0^+$ ground state. The change in angular momentum is $\ell = 1$ with no change in parity, so they are of the $M1$ type. The angular momentum of the emitted photon influences the angular distribution of the electron-positron pairs that it decays into. For this reason, IPC have been used in the nuclear physics field for decades because it enables the study of the multipolarity of nuclear transitions by measuring the distribution of the correlation angle $\vartheta_{e^+e^-}$, i.e. the angle between electron and positron. These distributions can be predicted with Rose theory [10] and they are characterized by a monotonically decreasing shape, peaking at $0°$ and rapidly falling as the correlation angle increases. IPC transitions can have a change in angular momentum of more than one unit, but this are suppressed as $\ell$ increases, so the decay happens preferentially through the lowest $\ell$ transition possible. Overall, internal pair creation (IPC) processes have reasonably high conversion coefficients (the ratio between decays via IPC and standard gamma emission), of the order of $10^{-3}$ to $10^{-4}$.

### 1.2.2 The ATOMKI Spectrometer

The ATOMKI spectrometer was built to study proton capture processes on a fixed target as follows:

$$p + {}^{A}_{Z}\mathrm{N} \rightarrow {}^{A+1}_{Z+1}\mathrm{N}^{*} \rightarrow {}^{A+1}_{Z+1}\mathrm{N} + e^{+}e^{-} \tag{1.20}$$

Initially, a 5 MV van de Graaff accelerator delivered the proton beam, which had a typical current of 1 $\mu$A. This was later replaced with a more stable 2 MV Tandem accelerator [11]. To excite a specific level of the product nucleus the beam needs to

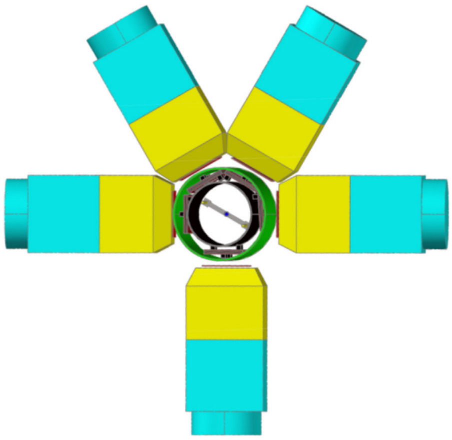

**Figure 1.11.** CAD drawing of the first version of the spectrometer. Figure taken from [12]

be tuned to the right energy. Under the assumption that the target nucleus is at rest and by using the conservation of four-momentum, this energy turns out to be:

$$E_p = \frac{m_{N^*}^2 - m_N^2 - m_p^2}{2m_N} \tag{1.21}$$

where $m_{N^*}^2$ is the mass of the excited nucleus, i.e the sum of the mass of the nucleons, the binding energy and the excitation energy. Figure 1.11 depicts the first version of the apparatus which is composed by [12]:

- A thin target in the center (blue dot in the figure) placed perpendicular to the beam, on which the proton beam impinges. In the experiment on $^8\mathrm{Be}$ the target was made of 15 $\mu g/\mathrm{cm}^2$ thick $\mathrm{LiF}_2$ and 700 $\mu g/\mathrm{cm}^2$ thick $\mathrm{LiO}_2$ targets evaporated on 10 $\mu$m Al backings.

- A carbon fiber vacuum chamber wall (black cylinder in the figure) with a radius of 3.5 cm and a thickness of 0.8 mm. This represents the main source of degradation in angular resolution due to multiple Coulomb scattering.

- 5 multiwire proportional chambers (MWPC) to detect the position of the hits of the leptons. They are placed around the target at $0°, 60°, 120°, 180°$, and $270°$. The angular resolution of this setup was $\Delta\vartheta \simeq 2°$.

- 5 $E - \Delta E$ telescopes, placed after the MWPC at the same angles. $\Delta E$ are thin ($38 \times 45 \times 1$ mm$^3$) plastic scintillator tiles, with minimum response to $\gamma$ radiation. The $E$ detectors are much larger ($78 \times 60 \times 70$ mm$^3$) and can stop almost all electrons and positrons up to 16 MeV energy.

- An High-Purity Germanium (HPGe) detector was placed 50 cm behind the target to detect gamma rays from the reaction $^7\mathrm{Li}(p, p'\gamma)$ (in the case of lithium target). This allows to continuously monitor the Li content of the target.

### 1.2.3 First anomaly observations in $^8$Be

The so called $^8$Be anomaly was first observed by the ATOMKI collaboration in 2016 during the study of the reaction [13]:

$$p + {}^7_3\mathrm{Li} \rightarrow {}^8_4\mathrm{Be}^* \rightarrow {}^8_4\mathrm{Be} + e^+e^- \tag{1.22}$$

The experiment focused on transitions to the $J^\pi = 0^+$ ground state of the 17.64 MeV $J^\pi = 1^+$ and the 18.15 MeV $J^\pi = 1^+$ levels. These resonances were populated using a proton beam energy of $E_p = 441$ keV and $E_p = 1.03$ MeV respectively. Given the narrow widths of these two excited states ($\Gamma = 12.2$ keV and $\Gamma = 168$ keV) compared to their energy difference, the probability of contamination between them is negligible. The distributions obtained for the correlation angle between $e^+$ and $e^-$ are illustrated in Figure 1.12.

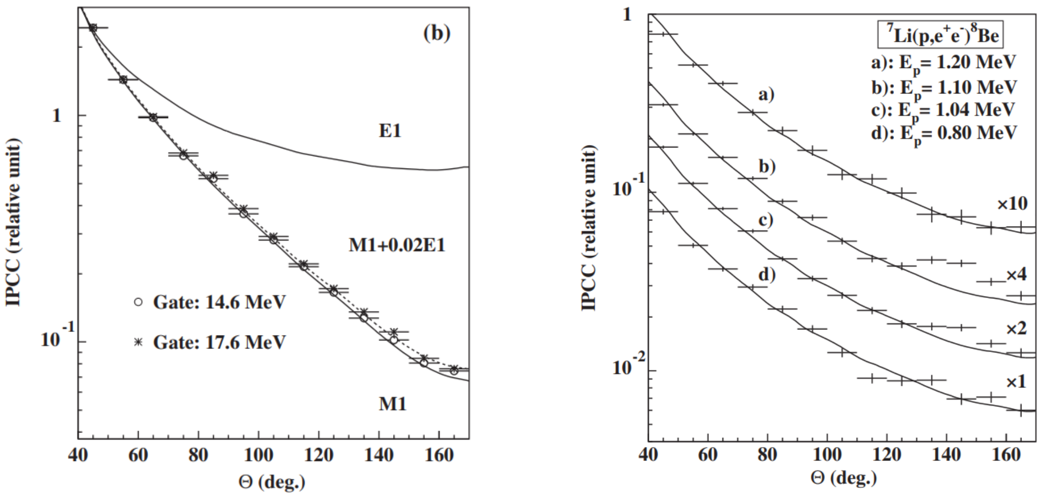


**Figure 1.12.** (Left) Correlation angle distribution for the 17.64 MeV transition. Data are represented with circles while simulation results are indicated with a solid line. (Right) Correlation angle distribution for the 18.15 MeV transition for four different beam energies.

Both transitions exhibit a deviation at large angles from the prediction of the simulation for values of the disparity parameter $y = (E_{e^-} - E_{e^+}) / (E_{e^-} + E_{e^+})$ ranging from -0.5 and 0.5. In the case of the 17.64 MeV transition this deviation can be explained by a small 0.2% E1 background component on top of the expected M1. This discrepancy arises from direct proton capture, i.e. not on resonance, which has mainly E1 multipolarity. Conversely, for the 18.15 MeV transition, the excess presents a peak-like shape that cannot be explained by the mixing of different multipolarities. The significance of the peak is at the $6.8\sigma$ level, making it highly unlikely to be a background fluctuation. Remarkably, the anomaly rises and falls as the beam energy scans across the resonance. The agreement with the data improves drastically by introducing a contribution due to a hypothetical neutral boson $X$ decaying into $e^+e^-$ in the fitting process. Such a boson, according to simulations,

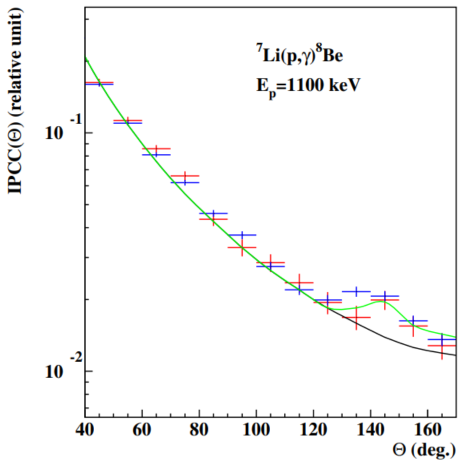


**Figure 1.13.** Angular correlation between $e^+e^-$ fro the 18.15 MeV transition at a beam energy of 1.1 MeV, blue markers refer to the first published results while red markers are the results obtained with the improved setup.

should give a contribution which is negligible for $|y| > 0.5$, a statement corroborated by spectra obtained for this range of $y$ values. Consequently, the correlation angle distribution can be expressed as a sum of the exponentially falling IPC and the signal distribution obtained by the simulation of the decay of a boson into $e^+e^-$:

$$PDF\left(e^+e^-\right) = N_{Bkgd} \times PDF(IPC) + N_{\text{Sig}} \times PDF(\text{ signal }) \tag{1.23}$$

where $N_{Bkgd}$ and $N_{Sig}$ are the fitted number of IPC and boson events, respectively. A $\chi^2$ analysis was performed to extract the mass of the hypothetical boson, yielding $m_X = 16.70 \pm 0.35(stat) \pm 0.5(syst)$ MeV. From the fit to the function in Equation 1.23 the branching ratio between IPC decay and X boson production was found to be R = $5.8 \times 10^{-6}$. To exclude the possibility that the anomaly was caused by an experimental effect not taken into account, the reaction was reinvestigated with an improved setup [14, 15]. With respect to the previous version, MWPC were replaced by 50 $\times$ 50 mm$^2$ double-sided silicon strip detectors (DSSD) with 3 mm wide strips and a thickness of 50$\mu$m. This also obviates the necessity for $\Delta E$ detectors, thus enabling the telescope to be situated in closer proximity to the interaction region. The entire electronics and data acquisition system was translated from the CAMAC to the VME standard and also the Van de Graaff accelerator was substituted in favour of a newer and more stable Tandem-type accelerator. An active shield made of 12 pieces of 1.0 cm thick plastic scintillator was installed above the spectrometer to suppress cosmic rays background by a factor 2.

Figure 1.13 shows the distribution of the correlation angle for the 18.15 MeV transition together with the best fit in the hypothesis of IPC plus boson decay. The best agreement between the data and the model is achieved for $m_X = 17.17(7)$ MeV, with an anomaly significance of $4.90\sigma$.

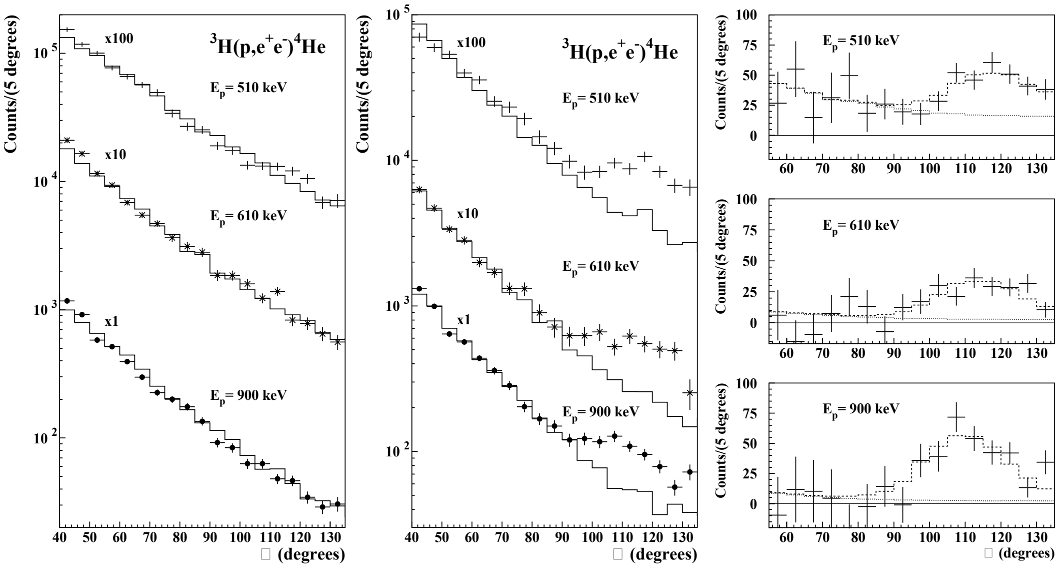


**Figure 1.14.** (Left) Correlation angle distribution for the "background" region for three different beam energies. (Center) Correlation angle distribution for the "signal" region. Experimental data is indicated with a marker while the solid black line represents the data from the simulation. (Right) Angular distribution after background subtraction, with the best-fit sum of IPC and X17 boson signal shown as a dotted histogram.

### 1.2.4 New evidencies of the anomaly in $^4\mathrm{He}$

As interest rose towards the unexpected results of the ATOMKI group, it was necessary to study the anomaly in different scenarios. One approach to constrain the quantum numbers of this new hypothetical particle is to explore various nuclei with levels possessing different $J^\pi$ combinations. Eligible nuclei should possess transitions with an energy at least as high as $m_X$ to enable $X$ boson production. For this reason, starting from 2019, the collaboration studied the reaction [16–18]:

$$p + {}^3_1\mathrm{H} \rightarrow {}^4_2\mathrm{He}^* \rightarrow {}^4_2\mathrm{He} + e^+e^- \tag{1.24}$$

Helium presents two excited states with suitable characteristics, one at $E_x = 20.21$ MeV ( $\mathrm{J}^\pi = 0^+$, $\Gamma = 0.50$ MeV) and another at $E_x = 21.01$ MeV ( $\mathrm{J}^\pi = 0^-$, $\Gamma = 0.84$ MeV) [18]. Unlike the Beryllium case, these levels have significantly larger widths, so that the two levels cannot be excited independently. In particular, the selected beam energies were $E_p = 510, 610$ and $900$ keV, resulting in excitation energies of $E_x = 20.21, 20.29$ and $20.49$ MeV, so that both levels were expected to be populated. The proton beam was directed at a $^3$H target, absorbed in a $4.2$ mg/cm$^2$ thick Ti layer evaporated on a $0.4$ mm thick molybdenum disk with $50$ mm diameter. To prevent tritium evaporation, the target was also cooled at liquid $\mathrm{N}_2$ temperature. Additionally, the number of telescopes was increased from $5$ to $6$ to eliminate any potential geometrical artifact that could have been responsible for the previous observed excess. The results are depicted in Figure 1.14. The left panel displays the angular distribution for the "background" region, which is clearly in good agreement with the simulated data. Instead, the right panel presents the same plot for the "signal" region, revealing a large excess around $\vartheta \simeq 115°$. The "background" signal corresponds to a cut in energy between 14 and 18 MeV, while the "signal" region comprehends the range from 18 to 22 MeV. The experimental data were fitted using the following intensity function:

$$INT = N_{EPC} \times PDF(EPC) + N_{IPC} \times PDF(IPC) + N_{Sig} \times PDF(Sig) \quad (1.25)$$

where the various probability density functions (PDFs) were simulated with GEANT3, and the various $N$ are the fitted parameters. The signal PDF depends parametrically on the X17 boson mass. Therefore, by letting it be a free parameter, the optimal mass can be identified. The results of the fit for the different beam energies are shown in Table 1.1

**Table 1.1.** Internal Pair Creation Coefficients (IPCC), branching ratio $B_x$, mass and confidence level derived from the fit for all the three beam energies [14].

| $E_p$ (keV) | IPCC $\times 10^{-4}$ | $B_x$ $\times 10^{-6}$ | Mass (MeV/$c^2$) | Confidence |
|---|---|---|---|---|
| 510 | 2.5(3) | 6.2(7) | 17.01(12) | $7.3\sigma$ |
| 610 | 1.0(7) | 4.1(6) | 16.88(16) | $6.6\sigma$ |
| 900 | 1.1(11) | 6.5(20) | 16.68(30) | $8.9\sigma$ |
| Averages | | 5.1(13) | 16.94(12) | |
| $^{8}$ Be values | | 6 | 16.70(35) | |

### 1.2.5 Further confirmation in $^{12}$C

To this point, the two experiments on $^{8}$Be and $^{4}$He have provided supporting evidence for the existence of the new X17 particle. However, the quantum numbers, in particular the parity properties, have not yet been definitively determined, as both the vector/axial-vector and pseudoscalar hypotheses could potentially explain the anomaly. This topic will be addressed in detail in subsection 1.3.1. Feng et collaborators, in [19] suggested to the ATOMKI collaboration to study the E1 decay to the $0^+$ ground state of the 17.2 MeV J$^\pi = 1^-$ state in $^{12}$C. To produce this resonant state the $^{11}$B(p, $\gamma$)$^{12}$C reaction was used with a beam energy of $E_p = 1.388$ MeV and a current of 2$\mu$A, twice as much as in previous experiments. The large level width ($\Gamma = 1.15$ MeV) allows the use of a thicker 2mg/cm$^2$ $^{11}$B target evaporated onto a 5 $\mu$m Ta foil. The reaction was studied at 5 different proton energies $E_p = 1.50$, 1.70, 1.88, 2.10, 2.50 MeV, chosen to compensate for the energy loss in the target, which was around 300 keV.

A clear excess was observed at $\vartheta \simeq 160°$ whose strength rises and falls as the beam energy scans across the resonance. The anomaly is statistically significant at

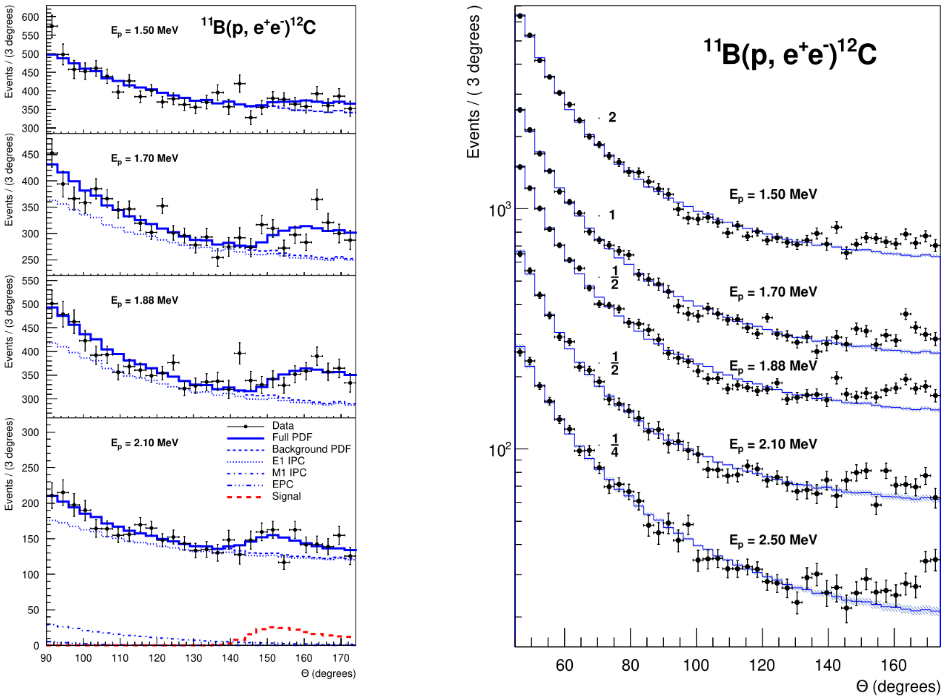


**Figure 1.15.** (Left) Angular correlation of IPC pairs for the 17.2 transition of $^{12}$C at different proton energies (Right) Angular correlation after background subtraction.

the 3$\sigma$ level in the off-resonance region and at the 7-8$\sigma$ in the on-resonance region. Subsequently, the experimental data were fitted with an intensity function, as was done in previous experiments, in order to extract the number of background events, $N_{Bkgd}$ and the number of signal events $N_{Sig}$. The mass of X17 was estimated by allowing it to be a free parameter in the fit for each beam energy. The average of these values is $m_X$ = 17.03 ± 0.11(stat.) ± 0.20(syst.) while the mean value for the branching ratio is found to be $B_X$ = 3.6(3) $\times 10^{-6}$ which agrees well with the previous results. This observation of the anomaly supports the vector nature of X17.

### 1.2.6 Latest results on Giant Dipole Resonance

The ATOMKI collaboration has recently concentrated its efforts on the *Giant Dipole Resonance* (GDR) of beryllium [20]. The GDR is the broad peak observed in the $\gamma$-ray absorption cross-section of numerous nuclei, typically occurring between 13 and 25 MeV. Its origin is attributed to the collective motion of neutrons and protons within the nucleus itself. Beryllium has a giant dipole resonance around an excitation energy of 22 MeV with $J^\pi = 1^-$, which can decay both to the $0^+$ ground state and to the $2^+$ first excited state [21]. For this experiment the resonance was induced with a proton beam of energy $E_p = 4$ MeV. A 1mg/cm$^2$ thick $^7Li_2O$ target was used to maximise the yield of IPC pairs due to the large width ($\Gamma$ = 5.3 MeV) of the resonance. The target was evaporated onto a 10$\mu$m thick Ta foil.

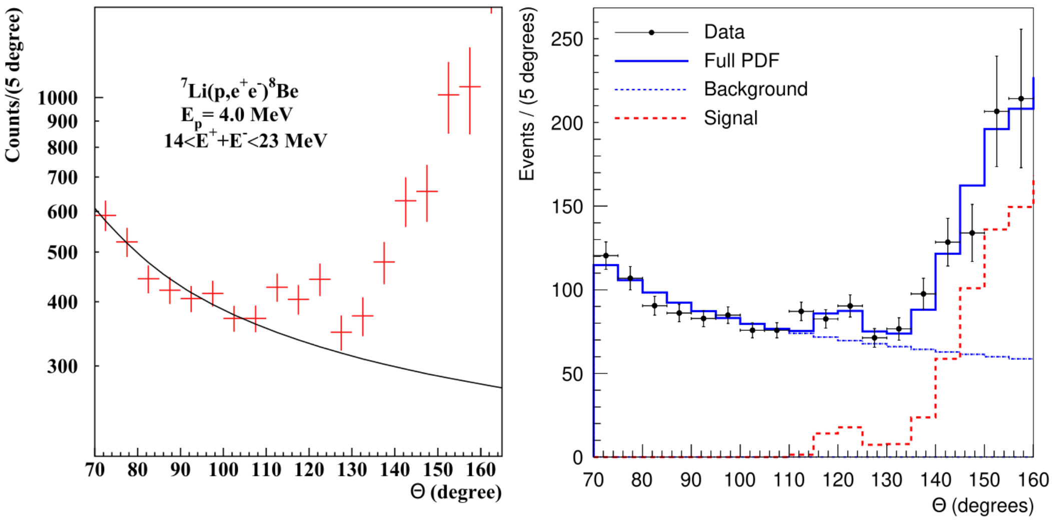


**Figure 1.16.** (Left) Angular correlation of IPC pairs for the GDR of $^8$Be at a bombarding energy of 4 MeV (Right) Angular correlation after background subtraction, the fit is represented by the solid blue histogram.

The number of telescopes of the spectrometer was reduced from 6 to 2 placed at an angle of 110° from each other, in order to avoid possible distortion due to the detector arrangement. This configuration permitted a reduction in the diameter of the carbon fibre tube from 70 mm to 48 mm and the placement of the telescope in close proximity to the target, thereby optimising the solid angle coverage. The absence of detectors in the vertical direction also resulted in a significant reduction in sensitivity to the cosmic ray background.

A peak-like excess was observed around 120°, as can be seen in Figure 1.16, accompanied by an even stronger excess around 160°. The presence of two peaks was interpreted as the production of X17 both in the transition to the ground state and the transition to the first excited state. The relative height of the peaks is compatible with the much stronger $\gamma$ decay of GDR to the first excited state than to the ground state, as evident from previous measurements [21]. The intensity function used in the fit took this into account and has the following expression:

$$\begin{aligned} INT\left(e^+e^-\right) = \quad & N_{E1} \times PDF(E1) + N_{M1} \times PDF(M1) + \\ & N_{\text{Sig}} \times \alpha_{\text{ground}} \times PDF(\text{ sigground }) + \\ & N_{\text{Sig}} \times \left(1 - \alpha_{\text{ground}}\right) \times PDF(\text{ sig 2 plus }) \end{aligned} \tag{1.26}$$

where $\alpha_{ground}$ is the fraction of X17 produced in the decay to the ground state. On the right side of Figure 1.16 the results of the fit can be seen to agree well with the experimental data. The value determined for the X17 mass is in this case $m_X = 16.94 \pm 0.47(\text{stat.})$ MeV. As in the case of $^{12}$C, the observation of this anomaly in an E1 transition lends support to the vector nature of X17. It should be noted that, at the present moment, the results on the GDR are not published yet and thus they should be regarded with care.

## 1.3 The dark sector hypothesis

All of the anomalies observed by the ATOMKI collaboration so far can be explained by introducing a new neutral boson with 17 MeV mass, emitted in the transition of excited nuclei, which decays in $e^+e^-$ pairs. The small mass of this hypothetical particle permits its accomodation within dark sector models, wherein it would serve to mediate a fifth fundamental interaction of Nature. In the absence of a nuclear physics explanation, a particle physics interpretation is attractive because of the striking agreement of the process kinematics with the experimental results obtained from different nuclei. To this end, we will first describe in more detail the production process of X17 [19]. A proton beam collides on a fixed target to form an excited nucleus through the reaction $p + A \to N^*$. The decay of the excited nucleus proceeds via the emission of the X boson which then decays to electron-positron pairs through $N^* \to N_0 X$ and then $X \to e^+e^-$. The beam energy required for resonant production is the one in Equation 1.21 and the excited nucleus is created with a velocity $\beta_{N^*} = p_p/(E_p + m_A)$ in the laboratory frame. Resonant production is consistent with the experimental observation that the strength of the anomaly varies as the beam scans through the resonance. After production of the excited nucleus, it decays to a lower energy state by emitting the X boson. In the rest frame of $N^*$, the boson has an energy of :

$$E_X = \frac{m_{N^*}^2 + m_X^2 - m_{N_0}^2}{2m_{N^*}} \approx m_{N^*} - m_{N_0} \tag{1.27}$$

where the approximation in the last step holds because $m_X \ll m_{N^*}$ and $m_{N^*} - m_{N_0} \ll m_{N_0}$. Moreover this also explain why the anomaly was not observed in calibration atoms where the transition energy was less than the boson mass. The speed of X in the rest frame of $N^*$ is $v_X = \sqrt{1 - (m_X/E_X)^2}$. Since all result from ATOMKI provice an X mass around 17 MeV (see Table 1.2), we can assume the speed of the emitted electron and positron to be $v_e \simeq 1$. For all the nuclei of interest the following inequality holds:

$$v_{N_*} \lesssim 0.01 \ll v_X < v_e \approx 1 \tag{1.28}$$

so the excited nucleus can be considered at rest in the laboratory frame. The electron and the positron are produced back-to-back in the reference frame where X is at rest. If the decay is isotropic (for example when X has spin 0) the angular distribution will have a maximum at $\cos(\vartheta) = 0$, where $\vartheta$ is the angle relative to the $\hat{z}$ direction, chosen to be parallel to the X velocity. In this case the boost will be perpendicular to the $e^+/e^-$ direction, and the particles are bent towards the boost direction by

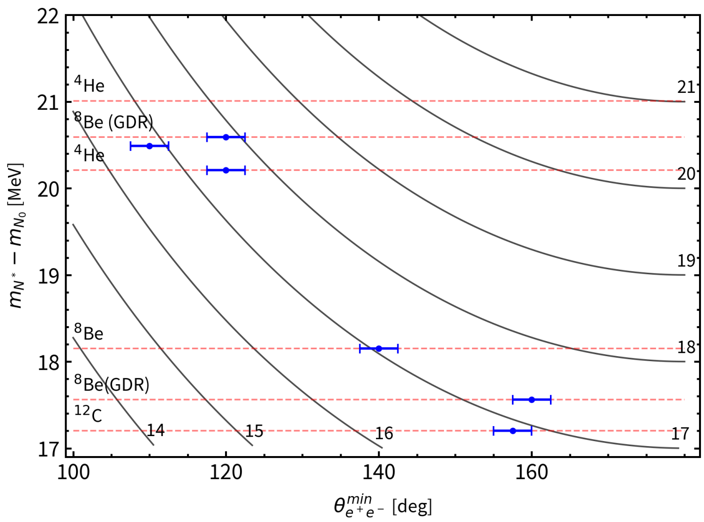


**Figure 1.17.** Nuclear mass splitting $m_{N^*} - m_{N_0}$ as a function of the minimum opening angle $\vartheta^{min}_{e^+e^-}$ for different assignments of the X boson mass. Blue points indicate the angle at which the peak of the anomaly was observed with an error corresponding to the bin size used in the Atomki papers. Figure adapted from [19] adding newer results.

the same amount. This results in a peak in the lab frame angular distribution at a specific minimal angle $\vartheta_{min}$, correlated to the energy available to X:

$$\vartheta^{min}_{e^-} = -\vartheta^{min}_{e^+} = \tan^{-1}\left(\frac{m_X}{p_X}\right) \quad \Rightarrow \quad \vartheta^{min}_{e^+e^-} \approx 2\tan^{-1}\left(\frac{m_X}{m_{N^*} - m_{N_0}}\right) \tag{1.29}$$

where in the last step we used Equation 1.27. Therefore such a production mechanism for the $X$ boson will manifest as an excess of events at $\vartheta^{min}_{e^+e^-}$ on top of the IPC distribution. In Figure 1.17, a contour plot based on Equation 1.29 is shown for different values of $m_X$. The various observations for different nuclei are all kinematically compatible with the production and subsequent decay of a boson with a mass around 17 MeV, which further corroborates the hypothesis of a new particle.

**Table 1.2.** Average best fit mass value for the different nuclei studied by the ATOMKI group.

| $N$ | $m_X$ (MeV) | $B_X(\times 10^{-6})$ |
|---|---|---|
| $^8$Be | $17.01 \pm 0.16$(stat) $\pm 0.20$(syst) | 6(1) |
| $^4$He | $16.94 \pm 0.12$(stat) $\pm 0.21$(syst) | 5.1(13) |
| $^{12}$C(17.23) | $17.03 \pm 0.11$(stat) $\pm 0.20$(syst) | 3.6(3) |
| $^8$Be(GDR) | $16.95 \pm 0.48$(stat) | ... |

At this point it is useful to recap the all the elements supporting a particle physics explanation of the ATOMKI anomaly [22]:

1. The excesses are all statistically significant. This means that it is very unlikely for them to be a background fluctuation and disappear by collecting more data.

2. The anomaly rises and falls as one tunes the proton beam energy to scan across the resonance.

3. The excesses are not generic deviations from the expected IPC predictions, but have a definite peak-like shape at an angle $\vartheta^{min}_{e^+e^-}$.

4. The positions of these bumps shift in accordance with the nuclear mass splitting, in agreement to what would occur for a boson decaying into an electron-positron pair.

### 1.3.1 Dynamical evidencies

We saw how an explanation of the anomalies observed by the ATOMKI collaborations is kinematically consistent with the production of a boson with a mass around 17 MeV which then decays into an electron-positron pair. The next step is to consider the dynamics of this process and gain some information on the $X$ particle spin and parity properties. For the sake of argument, we will assume that parity conservation is not violated, even though there is no compelling reason why $X$ could not have mixed parity. Conservation of angular momentum and parity implies the following conditions [19]:

$$\begin{aligned} J_* &= L \oplus J_0 \oplus J_X \\ P_* &= (-1)^L P_0 P_X \end{aligned} \tag{1.30}$$

where L is the final state angular momentum and $J_*^{P^*}$, $J_0^{P_0}$, $J_X^{P_X}$ refer respectively to the spin-parity of $N_*$, $N_0$ and $X$. For all transitions, except for $^8$Be(GDR→ $2^+$), the final nuclear state has $J_0^{P_0} = 0^+$ so the previous expressions become:

$$\begin{aligned} J_* &= L \oplus J_X \\ P_* &= (-1)^L P_X \end{aligned} \tag{1.31}$$

The possible spin-parity assignments obtained by direct application of the previous formulae are the following and are summarised in Table 1.3:

- **$^8$Be (18.15)** : the excited state has $J_*^{P_*} = 1^+$, so if $J_X = 0$ then $L = 1$ and can only be $P_X = -1$. Alternatively, if $J_X = 1$ then $L = 0, 1, 2$ and $P_X = 1, -1, 1$ respectively. Therefore X can be a pseudoscalar or a vector produced in a P-wave, an axial-vector produced in S or D-wave.

- **$^4$He (20.49)** : in the case of Helium we have to analyse both the 20.21 and the 21.01 MeV transitions because the anomaly has been observed at an intermediate energy of 20.49 MeV. For the $0^-$ state, if $J_X = 0$ then $L = 0$, and

$P_X = -1$. If $J_X = 1$, then $L = 1$ and $P_X = 1$. This means that $X$ can either be a pseudo-scalar produced in an S-wave of an axial-vector produced in a P-wave. For the $0^+$ state, the parity is opposite so the same results hold with the substitution scalar/pseudoscalar and vector/axial-vector.

- **$^{12}$C (17.2)** : for Carbon $J_*^{P_*} = 1^-$, so the same results obtained for $^8$Be hold with the replacement scalar/pseudoscalar and vector/axial-vector.
- **$^8$Be (GDR)** : for the transition from the GDR to the ground state, the spin-parity values are the same as in the Carbon case and the same results are true. For the transition to the first $2^+$ excited state, all of the parity assignments are compatible in principle [1].

**Table 1.3.** Possible spin-parity assignment of the $X$ boson compatible with the decays of $^8$Be, $^4$He and $^{12}$C [19]. The values for $^8$Be GDR have been computed by the author using Equation 1.31.

| $N_*$ | $J_*^\pi$ | $J^\pi$ (f.s) | Scalar $X$ | Pseudoscalar $X$ | Vector $X$ | Axial Vector $X$ |
|---|---|---|---|---|---|---|
| $^8$Be (18.15) | $1^+$ | $0^+$ | ... | ✓ | ✓ | ✓ |
| $^4$He (21.01) | $0^-$ | $0^+$ | ... | ✓ | ... | ✓ |
| $^4$He (20.21) | $0^+$ | $0^+$ | ✓ | ... | ✓ | ... |
| $^{12}$C (17.23) | $1^-$ | $0^+$ | ✓ | ... | ✓ | ✓ |
| $^8$Be (GDR→ g.s.) | $1^-$ | $0^+$ | ✓ | ... | ✓ | ✓ |
| $^8$Be (GDR→ $2^+$) | $1^-$ | $2^+$ | ✓ | ✓ | ✓ | ✓ |

[1] The possible spin-parity values of X17 for the GDR decay of $^8$Be are not present in literature yet, so they have been computed by the author using Equation 1.31.

# Chapter 2

# The PADME Hunt for X17

The PADME experiment (Positron Annihilation into Dark Matter Experiment) is a fixed target experiment designed to search for the dark photon $A'$ through the associated production process:

$$e^+e^- \to A'\gamma \tag{2.1}$$

A beam of positrons collides with the atomic electrons of an active diamond target, assumed to be at rest, where the reaction takes place. The final state photon is detected by an Electromagnetic Calorimeter (ECal) while the dark photon $A'$ escapes undetected. The observable of interest is the missing mass of the system, computed via the formula:

$$M^2_{miss} = (P_{e^+} + P_{e^-} - P_\gamma)^2 \tag{2.2}$$

This quantity should present a peak centred at the dark photon mass $M_{A'}$ in the case it exists [23]. This chapter is devoted to the detailed description of PADME experimental apparatus in its original configuration used for Run I and II, which took place in 2018 and 2020 respectively. The modification to the setup needed for the X17 search carried on during Run III, concluded in 2022, will also be discussed in order to highlight its limitations and show why the introduction of a gas-based tracker would be beneficial for the upcoming Run IV, scheduled for January 2025.

## 2.1 The DAΦNE Beam Test Facility

The PADME experiment is located in the Beam Test Facility (BTF) of the INFN Frascati National Laboratories. The BTF is part of the larger DAΦNE $\phi$-factory accelerator complex, which consists of an electron and positron LINAC, a 510 MeV accumulator ring where electrons and positrons are stacked and stored before being injected into the two 510 MeV main rings. The BTF is typically used for detector calibration purposes, as it can provide a wide range of particle multiplicities down to single-electron mode, with an energy between 50 and 800 MeV, a bunch length of 10 ns and a maximum repetition rate of 50 Hz. Accelerated particles from the LINAC

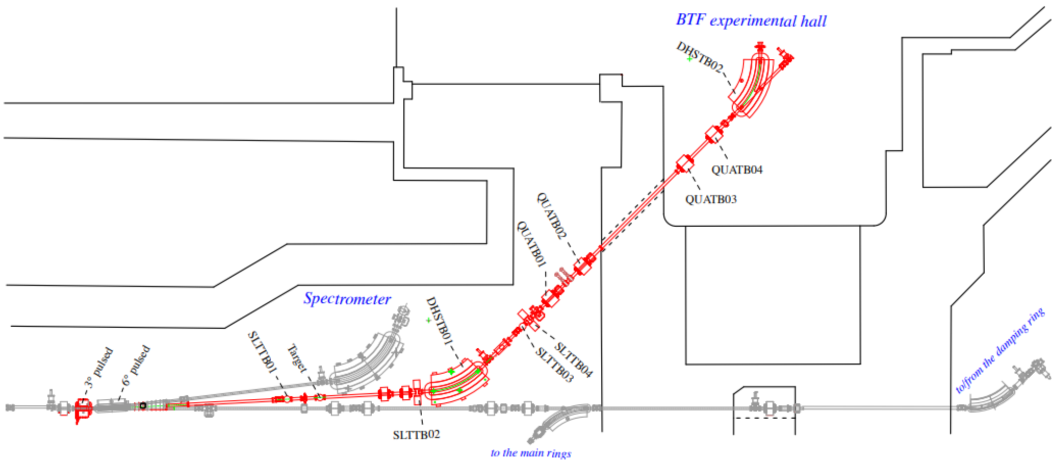


**Figure 2.1.** Layout of the transfer line from the LINAC to the Main Rings, to the BTF, and to the spectrometer line.

can be deflected to the BTF by a $45°$ bending magnet (DHSTB01 in Figure 2.1). One bunch per second is directed to a spectrometer line where a hodoscope is used to monitor the momentum of the beam. Two operational modes are possible :

- *Parasitic mode*: Only bunches which are not injected into the main DAΦNE rings are sent to BTF. This mode limits the range of possible beam properties to those compatible with collider operation.
- *Dedicated mode*: In this mode the beam configuration is completely under BTF control, and specific user-required beam properties can be obtained.

The available beam properties in both modes are summarized in Table 2.1. The LINAC accelerates electrons coming from a thermionic electron gun, and the positron beam is produced following a technique based on the SLAC scheme:

- *Primary positron beam*: a Tungsten-Rhenium target with adjustable thickness (about $2X_0$) is interposed in the electron beam trajectory after the first 5 accelerating sections of the LINAC. The positrons produced in the interactions are collected and directed towards the remaining part of the LINAC, where they are further accelerated.
- *Secondary positron beam*: the electron beam is intercepted by a Copper target placed just behind the magnet that deviates the beam towards BTF. It has three available thicknesses, 1.7, 2 or 2.3 $X_0$. This produces a secondary beam with a wide range of energies, from LINAC energy down to few MeV.

After crossing DHSTB01 dipole the beam is focused by 2 pairs of quadrupoles before reaching the DHSTB02 dipole which eventually deflects the beam towards the PADME experiment. PADME requirements on beam properties include: a

**Table 2.1.** Possible beam parameters available at BTF in different operation modes. *According to DAΦNE status.

| Parameter | Values | | | |
|---|---|---|---|---|
| Maximum flux | $3.125 \cdot 10^{10}\ \mathrm{s}^{-1}$ | | | |
| Spot size (hor.) | $0.7 - 55$ mm | | | |
| Spot size (vert.) | $0.7 - 25$ mm | | | |
| Divergence | $1 - 2$mrad | | | |
| Parameter | Parasitic mode | | Dedicated mode | |
| Pulse duration | 10 ns | | $1.5 - 40$ ns | |
| Repetition rate | Variable* | | $1 - 49\ \mathrm{s}^{-1}$ | |
| | Target in | Target out | Target in | Target out |
| $e^-$Energy (MeV) | $25 - 500$ | 510 | $25 - 700$ | $250 - 730$ |
| $e^+$Energy (MeV) | $25 - 500$ | 510 | $25 - 500$ | $250 - 530$ |
| Energy spread | 1% at 500MeV | 0.5% | 0.5% | 0.5% |
| Intensity | $1 - 10^5$ | $10^7 - 10^{10}$ | $1 - 10^5$ | $10^3 - 10^{10}$ |

bunch length of 250 ns, a small transverse dimension of $\sim$ 1mm, an energy spread smaller than 1% and a number of positrons per bunch of the order of $10^4$. The need for an extended bunch length was to reduce pile-up probability while keeping a high number of $e^+$ per bunch. The tight constraints on emittance and energy spread allow for the precise knowledge of the initial state 4-momentum, which affects the resolution in the missing mass through Equation 2.2.

## 2.2 The PADME experiment retrospective

The PADME experiment is composed of different subdetectors, all serving a different purpose, which we will describe in detail in the next few sections. A scheme of the apparatus is shown in Figure 2.2. Positrons coming from the BTF beam collide on a thin *Active Diamond Target*, and the products of this collision reach the region downstream the target. A *Dipole Magnet* defines a region in which final state charged particles, for example emerging from SM BhaBha scattering, are deflected towards the sides of its gap where the *EVeto* and *PVeto* detectors are placed. Non-interacting beam positrons are deflected by the magnetic field towards a *TimePix-based beam monitor*. The photons are detected by an electromagnetic calorimeter at a distance of $\sim$ 3.5 m downstream of the target. The calorimeter is built with a hole in the center to be insensitive to the high yield of bremsstrahlung photons, which are concentrated at small angles. A fast Cherenkov-based calorimeter, the *Small Angle Calorimeter* covers this region. The region between the target and the calorimeter is occupied by a vacuum vessel kept at a pressure of $10^{-6}$ bar to minimize the particle interaction with air. The vacuum chamber ends with a circular convex 2.5 mm thick carbon fiber window, to minimize the Coulomb scattering of particles directed onto the calorimeter. Event candidates are selected by requiring the presence of a single cluster in the electromagnetic calorimeter and no other coincident signal in the charged particle vetoes and in the Small Angle Calorimeter. In Run III to be able to discriminate between charged leptons and photons, a *Charged Particle Tagger* was installed just before the electromagnetic calorimeter.

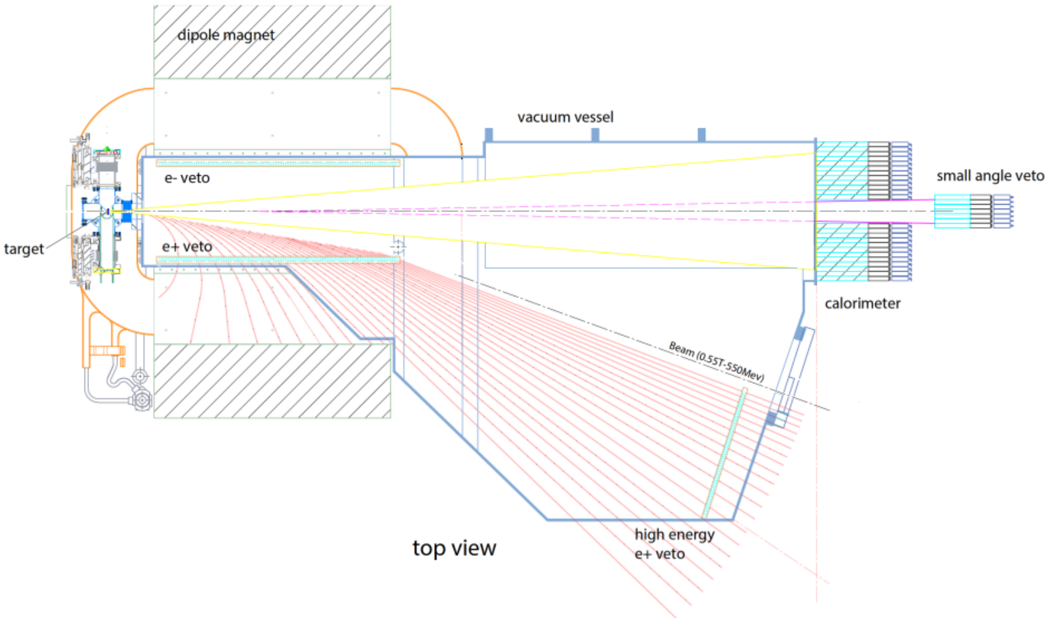


**Figure 2.2.** Schematic of the PADME apparatus, in the configuration used in Runs I and II [24].

### 2.2.1 Diamond Active Target

The PADME target is made up of a $100\mu$m thick diamond film, with an area of $2 \times 2\text{cm}^2$, grown using a process called *Chemical Vapour Deposition* (CVD) [25]. In this technique a mixture of gases containing the material to be deposited (in the case of diamond usually methane and hydrogen) fills a vacuum chamber and it is heated to a high temperature. A small natural crystal is placed inside the same chamber and acts as a seed around which the diamond layer grows. The choice of a carbon-based material is driven by the dependence of the Bremsstrahlung cross-section on the atomic number Z, which increases with $Z^2$, while the annihilation cross section grows with Z. The target is used both to provide the electrons for the annihilation process and to monitor the positron beam. The readout is obtained using electrodes made by "graphitisation" of the CVD diamond surface. The electrodes have been obtained by focusing an ArF excimer laser on the diamond, moved by an automated two-arm system in the $L^3$ laboratory of the Università del Salento and INFN Lecce.

Each side has 19 strips, with a length of $1.9$ cm, $0.85$ mm width and a pitch[1] of $1$ mm, aligned in orthogonal directions on the two sides to measure the X and

[1] Pitch is defined as the distance between two consecutive readout elements, in this case between two neighboring strips.

Y beam properties. The strips are connected to the readout contacts by spots of Araldite glue. An image of the active target mounted on the chip containing the front-end electronics is shown in Figure 2.3a. The readout of the strips is performed by two AMADEUS chips containing 16-channels charge preamplifiers [25]. The signal is digitized, as the rest of the PADME detectors, by the CAENV1742 switched-capacitors ADC, featuring a 12-bit depth and a sampling rate of $1-5$GS/s. An example signal from one strip can be seen in Figure 2.3b. The position of the beam on the diamond target is measured by computing the charge centroid and the resolution is evaluated to be $\sim 0.6$ mm from the RMS of the charge centroid distribution obtained for about 1000 events with a multiplicity of around 20000 positrons per bunch. at an energy of $545$ MeV. The response to different bunch multiplicities was calibrated using a Lead Glass Cherenkov calorimeter, by measuring the charge collected by the active target as a function of the number of particles per bunch. The relationship between these two quantities is linear and allows the luminosity of the experiment to be measured to a $1\%$ precision.

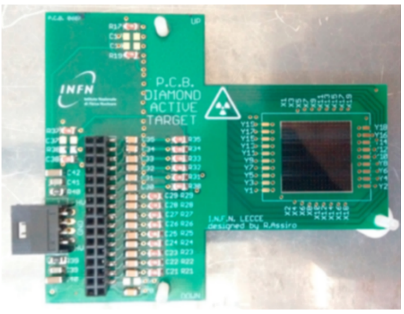


(a)

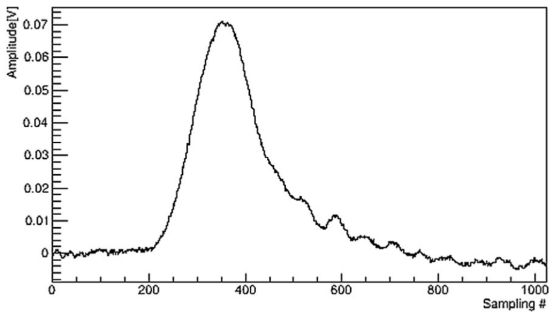


(b)

**Figure 2.3.** (a) Image of the active diamond target mounted on the PCB containing the front-end electronics. (b) Digitized waveform of the signal of a single active target strip.

### 2.2.2 Electromagnetic Calorimeter

The Electromagnetic Calorimeter (ECal) is the heart of the PADME Experiment [26]. Its role is to detect photons in the final state, whether originating from the associated production signal or the two-photon annihilation process. It is composed by 616 BGO bismuth-germanate crystals, with a volume of $2.1 \times 2.1 \times 23.0$ cm$^3$, placed $\sim 3.5$ m behind the target and arranged in a cylindrical shape with a radius of approximately $29$ cm. The dimensions of the crystals are chosen to maximize the shower containment, with a length of $\sim 20X_0$ and a transverse dimension of around $1$ Moliére radius, ensuring a lateral shower containment of almost $90\%$ [source PDG]. A summary of BGO properties can be found in Table 2.2. The crystals were recovered from the L3 experiment, and cut to the proper size and shape. An accelerated annealing process, intended to heal them from the opacity induced by extended exposure to radiation, was also performed. After the refurbishing,

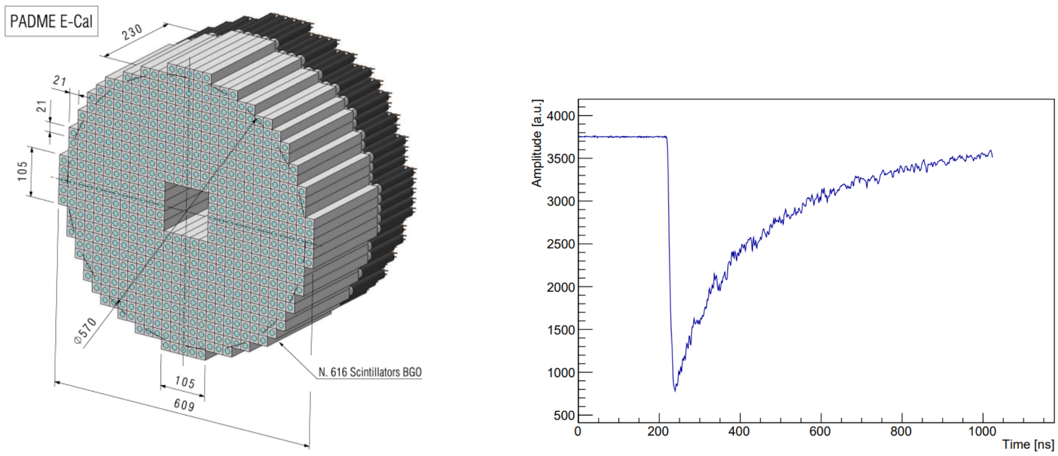


**(a)** **(b)**

**Figure 2.4.** (a) CAD rendering of PADME electromagnetic BGO calorimeter. The PMTs are shown in black. (b) Example of digitized waveform of one of the ECal crystals.

the crystals were coated with three layers of reflective paint, and glued to the photomultipliers, one for each crystal. To avoid crosstalk, the crystals are separated by $50\ \mu$m black Tedlar foils. The calorimeter is built with a central hole of $105 \times 105$ mm$^2$. This is because the decay time of the BGO scintillation light $\tau_{BGO} \sim 300$ ns is too long to bear the Bremsstrahlung photons rate, concentrated at small angles with respect to the beam beam direction. Figure 2.4a shows a rendering of the ECal structure, with the BGO crystal drawn in gray and the PMTs behind, in black.

The readout of the crystals is achieved with the XP1911 type B photomultipliers (PMTs) from HZC Photonics, which are particularly suited for this purpose given their sensitivity to light at $480$ nm, where the BGO spectrum exhibits maximum. The signal is digitized using a CAEN V1742 digitiser, which provides 1024 12-bit samples at a rate of $1$ GS/s.

The first $200$ ns of the acquisition are used for baseline evaluation, leaving a $3\tau_{BGO}$ time to sample the scintillation pulse. An example pulse is shown in Figure 2.4b. The integral of the signal can be used to measure the total energy deposited by the impinging particle. The energy resolution of the calorimeter was studied by using a variable energy beam provided by Frascati BTF on a smaller $5 \times 5$ crystals matrix. The relative resolution obtained was fitted according to the well known formula:

$$\frac{\sigma(E)}{E} = \frac{a}{\sqrt{E[\mathrm{GeV}]}} \oplus \frac{b}{E[\mathrm{GeV}]} \oplus c \tag{2.3}$$

Results give $a = 2\%$, $b = 0.003\%$, $c = 1.1\%$, compatible with the values provided by the original L3 calibration. The calorimeter is not only important to accurately measure particle energy, but it also provides the coordinate of the impact point, used to measure the photon direction assuming the target as its starting point.

Purely from geometrical consideration the expected position resolution is around $2.1$ cm / $\sqrt{12} \simeq 6$ mm. Actually the impact position is measured from a charge weighted average of the hit crystals belonging to the same cluster, improving the space resolution to 3 mm. This, combined with the target-ECal distance, translates into an angular resolution of $\sim 1$ mrad. Further details on the clustering algorithm used can be found in [27].

**Table 2.2.** Properties of BGO inorganic scintillator crystals.

| | $\rho$ (g/cm$^3$) | $X_0$ (cm) | $R_M$ (cm) | $\frac{dE}{dx}$ (MeV/cm) | $\lambda_I$ (cm) | $\tau_{\text{decay}}$ (ns) | $\lambda_{\max}$ (nm) | $n$ |
|---|---|---|---|---|---|---|---|---|
| BGO | 7.13 | 1.12 | 2.23 | 9.0 | 22.8 | 300 | 480 | 2.15 |

### 2.2.3 Small Angle Calorimeter

The Small Angle Calorimeter (SAC), shown in Figure 2.5a, is placed behind the ECal central hole to cover the angular region $\theta \lesssim 1^\circ$ and has a square matrix structure made of $5 \times 5$ $PbF_2$ crystals, each with a transverse dimension of $30 \times 30$ mm$^2$ and a length of $140$ mm. It is used to veto 2 and 3-$\gamma$ events where one photon hits the calorimeter and the others escape through the calorimeter hole. Lead fluoride is a Cherenkov radiator: when a photon strikes the crystal, the charged particles produced in the electromagnetic shower development emit Cherenkov photons. This type of radiation is instantaneous and has no decay time. Thanks to a fast photomultiplier tube a very short signal with a length of around $5$ ns is obtained, allowing the SAC to sustain a much larger rate of photons compared to ECal. This is of primary importance since the Bremsstrahlung rate in the central region can reach a few hundred MHz. The readout is performed with Hamamatsu R13478UV photomultiplier tubes. A test beam on a prototype of this detector,

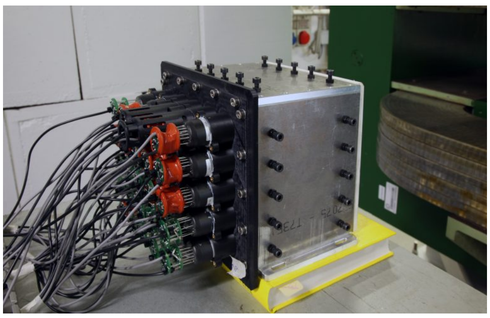

(a)

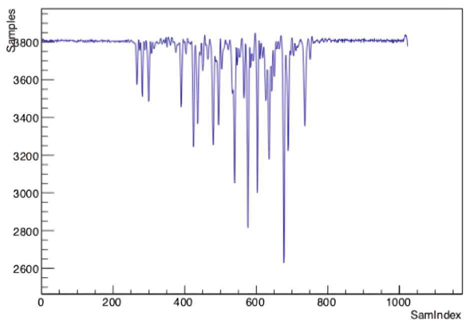


(b)

**Figure 2.5.** (a) Image of PADME Small Angle Calorimeter before installation in the setup. (b) Digitized waveform of the signal of the SAC. The peaks are different photons hitting the crystals in a 250 ns window.

described in detail in [28], found a time resolution of $81$ ps with a double-peak

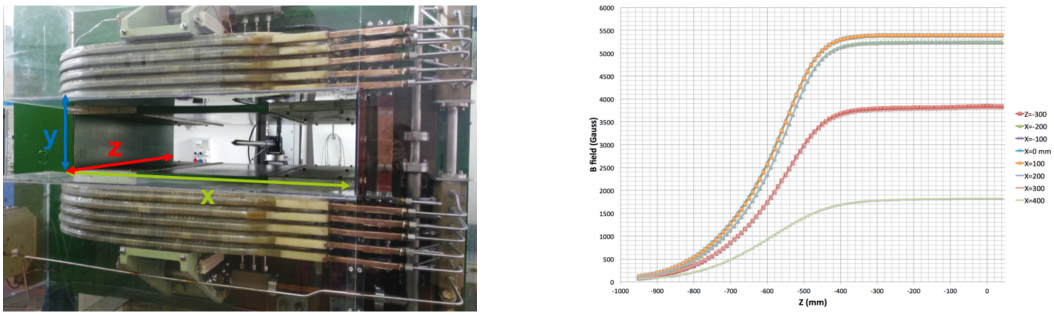


**(a)** **(b)**

**Figure 2.6.** (a) Image of the PADME dipole highlighting the coordinate system of the experiment. (b) Magnetic field map measured at LNF with a Hall probe.

separation capability of $1.8$ ns. The single crystal energy resolution was $10\%$ for an electron beam of $545$ MeV. In the full detector however the escaping energy is collected by the neighbouring crystals thus improving the energy resolution.

### 2.2.4 Dipole Magnet

The PADME dipole magnet is placed between the target and the ECal. It is used for two different reasons:

1. To deflect away from the SAC positrons that do not interact in the target. With a bunch length of $250$ ns and $10^4$ $e^+$/bunch, the rate of positrons in the SAC would reach $40$ GHz, completely overwhelming the detector.

2. To deflect in the charged particle vetoes (see subsection 2.2.5) positrons losing a small fraction of their energy in the target due to Bremsstrahlung, or electrons and positrons from BhaBha scattering. This allows to veto the presence of charged particles in single-photon events, thus rejecting background.

Given the geometrical layout of the PADME experiment, to bend the beam out of the calorimeter acceptance, which is around $\pm 100$ mrad, a minimum integrated magnetic field of $BL_{min} \simeq 0.42$ Tm is needed. Fortunately this requirement was matched by a spare dipole magnet belonging to the SPS transfer line with a length of $\approx 1$ m. In order not to reduce the calorimeter acceptance the dipole has to have a vertical gap of at least $20$ cm. The magnetic field that could be reach with power supplies available at LNF for this value of the gap is $0.9$ T, well above the PADME requirement [24]. A figure of the final PADME magnet, along with its support structure is shown in Figure 2.6a together with the magnetic field map measured in Frascati after the magnet shipping from CERN (Figure 2.6b).

### 2.2.5 Charged particle vetoes

PADME has 3 charged particle detectors for background vetoing: the Positron Veto (*PVeto*) and the Electron Veto (*EVeto*) are placed respectively on the right and left internal wall of the dipole magnet; the High Energy Positron Veto (*HEPVeto*) instead covers a region of the vacuum vessel between the magnet end and the beam dump (see Figure 2.2). The first two are $1$ m long detectors made of 96 plastic scintillating bars, with size $10 \times 10 \times 180$ mm$^3$ mainly intended to veto energetic Bremsstrahlung and possible BhaBha final state radiation. They could also be used to search for visible decays of the dark photon. The HEPVeto instead is made of 16 scintillating bars, mainly used to reject Bremsstrahlung events with low-energy photons in the final state. In Bremsstrahlung processes the energy of the photon and of the positron should sum up to the initial energy and therefore in the case of low-energy photons, the positrons have an energy near the one of the beam and hence they have a smaller curvature radius, ending up in the HEPVeto and not in the PVeto. The scintillating bars are oriented with the long side parallel to the magnetic field direction and slightly tilted by and angle of $0.1$ rad on their longitudinal axis (see Figure 2.7b). The emitted light is collected by Hamamatsu 13360 silicon photo-multipliers coupled to the bars through an optical wavelength shifter (WLS). Analogue to digital conversion happens by means of CAEN V1742 modules tuned at $2.5$ GS/s sampling rate. The two most important PADME requirements on these detectors are a very good time resolution ($< 1$ ns) to properly match a Bremsstrahlung photon in the calorimeters with the positron that initiated the process. The second requirement is an efficiency of $99\%$ in order to achieve a sufficiently low contamination of Bremsstrahlung in the candidate signal sample. These properties were measured using a $500$ MeV single-electron beam at LNF-BTF, yielding a time resolution of $800$ ps and an inefficiency lower than per-mille level. Further details on the testing procedure can be found in [29].

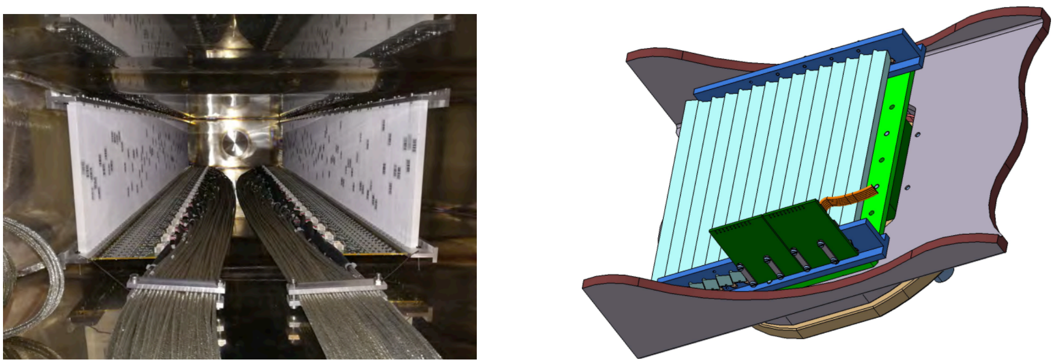

**(a)** **(b)**

**Figure 2.7.** (a) Photo of the placement of the EVeto (on the left) and PVeto (on the right) inside the PADME vacuum chamber. (b) CAD drawing of the prototype used for testing the vetoes performances. The slight tilt of the bars can be appreciated.

**Figure 2.8.** The twelve TimePix3 chips after installation in the PADME apparatus.

### 2.2.6 TimePix3 Array Beam Monitor

To measure the beam properties, as number of positrons, beam time profile and beam spot size, an array of $6 \times 2$ TimePix3 chip was placed where non-interacting beam positrons are deflected by the dipole magnet.

The TimePix3 chips have been developed at CERN and feature a matrix of $256 \times 256$ silicon pixel with size of $55 \times 55$ $\mu$m$^2$. Time-of-Arrival (ToA) and Time-over-Threshold can be acquired separately for each pixel. Each chip can be operated in two modes: frame-mode, in which the integrated ToA/ToT over a defined interval of time is acquired; data-driven mode, where data from each pixel is continuously streamed. The TimePix3 Array control and data acquisition application was developed from scratch to overcome limitation of vendor-provided software [30]. For the first two PADME runs, the clock of this detector was separated from that of the rest of PADME apparatus due to technical limitations and the matching between bunches was done offline, exploiting the TimePix3 timestamp and beam batch counting. Figure 2.8 shows the the full TimePix3 Array installed in the experimental apparatus.

### 2.2.7 Electron Tagger: ETag

During Run III, the PADME collaboration concentrated its efforts on the investigation of the Atomki Anomaly (see section 1.2). Since X17 is supposed to decay into $e^+e^-$ pairs, it must be possible to produce it by the reverse process, that is to say by electron-positron annihilation. In order to allow charged particles to reach the ECal the PADME dipole magnet was switched off during Run III. To distinguish charged particles from photons, a new detector, the Electron Tagger (ETag), has been installed in front of the ECal. The detector is made of 18 thin BC-408 plastic scintillator slabs with dimensions $4 \times 60 \times 0.5$ cm$^2$. This material has a radiation

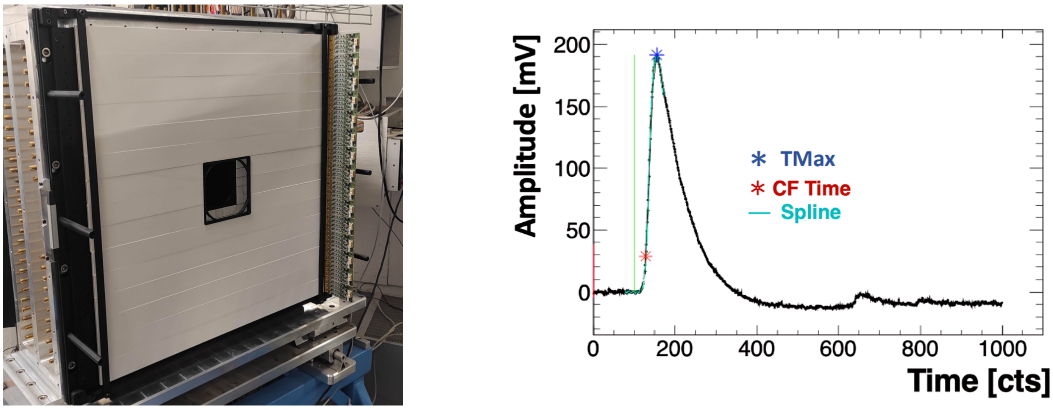


**(a)** **(b)**

**Figure 2.9.** (a) The ETag assembled in front of the electromagnetic calorimeter. (b) Example ETag digitized waveform.

length $X_0 \simeq 43$ cm [see Luxium Solutions], so for the chosen thickness it is practically unaffected by the passage of photons. Charged particles, however, lose energy in the material exciting its atoms, thus producing scintillating light with a decay time of $\tau_{BC-408} \simeq 2.1$ ns, suitable for the expected rate of BhaBha events. Readout is made with Hamamatsu S13360-3050PE Silicon PhotoMultipliers (SiPM) placed on both side of each slab. An image of the ETag can be seen in Figure 2.9 together with an example signal.

## 2.3 PADME Run III

PADME Run III took place in the autumn of 2022 and was dedicated to the X17 search through the resonant production process $e^+e^- \to X_{17} \to e^+e^-$ [31]. For positrons impinging on the electrons of the diamond target, assumed to be at rest, the resonant condition is:

$$E_{beam} = \frac{M_X^2}{2m_e} \tag{2.4}$$

The DAΦNE BTF is able to provide positrons with the required energy $\sim 280$ MeV and to change it in the nearby region, controlling the energy spread to the level of $\sigma_E \simeq 0.7$ MeV. To probe the $X_{17}$ mass region suggested by Atomki nuclear experiments (see Table 1.2), a fine scan procedure was carried in the $\sqrt{s}$ interval [16.2, 17.3] MeV, corresponding to $5\sigma$ below and $4\sigma$ above the predicted $X_{17}$ mass. The scan was performed in energy step of $\simeq \sigma_E$ and with a statistics of $\sim 10^{10}$ positrons on target per scan point. Given the very narrow prediction for the $X_{17}$ width (around $10^{-5}$ eV), if this particle exists an excess of $e^+e^-$ final states should appear in a single bin of the scan of $N(e^+e^-)/N_{PoT}$ vs $\sqrt{s}$ (actually this is true only neglecting the electron motion in the target as we will mention later).

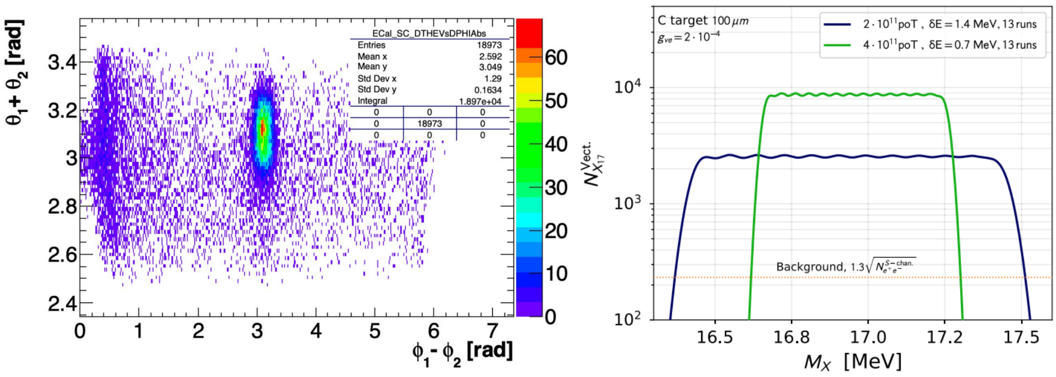


**(a)** **(b)**

**Figure 2.10.** (a) $\theta_1 + \theta_2$ vs $\phi_1 - \phi_2$ in the center of mass frame for off-resonance data. (b) Number of expected $X_{17}$ as a function of $\sqrt{s}$.

The selection of the signal candidates is based on the requirement of two in-time clusters in the ECal, compatible with two-body kinematics. The information coming from the ETag is not currently used in the analysis yet. Then the four-momenta of the selected two-leptons events are boosted to the centre of mass frame and a cut in the $|\theta_1 + \theta_2|$ vs $|\phi_1 - \phi_2|$ plane is imposed to select only events compatible with back-to-back kinematics (see Figure 2.10a). $\theta$ and $\phi$ are respectively the angle of the particle momentum with respect to the beam direction and the angle of the transverse component of the momentum with respect to the x-axis. In the hypothesis of vector nature for $X_{17}$, a coupling of the order of $g_{ve} \sim 2 \cdot 10^{-4}$, can translate into thousands of produced $X_{17}$ bosons, resulting in excess at the $\%$ level. To appreciate such a small deviation it is crucial to keep the uncertainties under control, in particular the one on the number of positrons on target ($N_{PoT}$). In order to do so, the positron flux is measured by means of an OPAL LeadGlass crystal placed downstream of the setup. Since the mass region to investigate was very well known, precision over statistics was favoured and the number of positron per bunch was lowered to $\sim 2.5 \times 10^3$ to reduce pile-up probability. In Figure 2.10b, the expected number of produced $X_{17}$ particles in the vector nature case is shown. A measurement of charged leptons direction and momentum is difficult to perform using the information coming from EVeto and PVeto. For this reason it was decided to switch off the dipole magnet and let charged particle reach the ECal. This required the presence of a charged particle tagger (described in subsection 2.2.7) in front of the calorimeter to distinguish photons from electrons and positrons, allowing to bring the background from $2\gamma$ events to a negligible level.

The remaining background is caused by SM BhaBha scattering, which shares with the $X_{17}$ signal the exact same final state and has two main contributions: *s*-channel and *t*-channel (when computing the matrix element of the process, actually an interference term also appear, but its contribution can be proven to be negligible). While *t*-channel can be distinguished kinematically, since in most of the

**Table 2.3.** Number of expected events for different final states for $10^{10}$ positrons on target.

| BG process | No. of Ev. | No. of Ev. in Acc. | Acc. |
|---|---|---|---|
| $e^+e^- \to e^+e^-(t-\text{ ch. })$ | $5.4 \times 10^7$ | $6.9 \times 10^4$ | 0.13% |
| $e^+e^- \to e^+e^-(s-ch).$ | $3.2 \times 10^4$ | $6.4 \times 10^3$ | 20% |
| $e^+e^- \to \gamma\gamma$ | $2.9 \times 10^5$ | $1.3 \times 10^4$ | 4.5% |
| $e^+e^- \to X_{17} \to e^+e^-$ | 1250 | 250 | 20% |

cases the primary beam positron conserves almost its entire energy and the target electron remains almost at rest, the $s$-channel shares completely its kinematics with the$X_{17}$ signal, representing therefore an irreducible background. A summary of the expected number of signal and background events for a single scan point is included in Table 2.3. The projected limits both for the vector hypothesis and for the pseudoscalar (ALP) hypothesis are shown in Figure 2.11. Analysis of the data collected in this Run is currently ongoing at the moment of writing the present chapter.

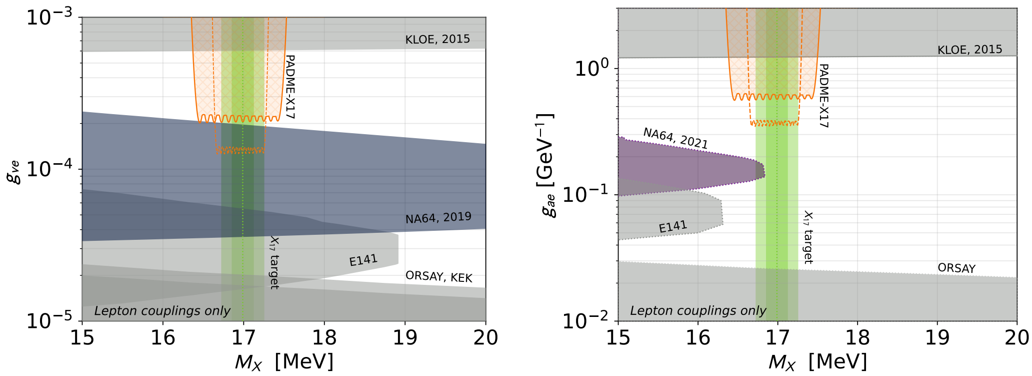


**(a)** **(b)**

**Figure 2.11.** (a) Projected 90% C.L. sensitivity of PADME Run III on the $g_{ve}$ vector coupling in the hypothesis of X17 vector nature. (b) Projected 90% C.L. sensitivity of PADME Run III on the $g_{ae}$ axial coupling in the hypothesis of X17 pseudoscalar nature.

## 2.4 A tracker for Run IV: Why?

In Run III, the achievable precision in the measurement of $N(e^+e^-)/N_{PoT}$ was limited by the luminosity uncertainty. Using the ratio between the number of events in two different channels, leads to a cancellation of the systematics related to $N_{PoT}$ thus overcoming this limitation. Therefore, for Run IV, it was decided to search for an excess in the $N(e^+e^-)/N(\gamma\gamma)$ ratio. In this context is crucial to achieve an excellent discrimination power between charged and neutral final states. A statistics increase is also needed to reach the final sensitivity in Run IV, due to the effect of the electrons motion in the target atoms which smears the center of mass energy. This effect was considered negligible in the first analysis, but as showed in Figure 2.10b it leads to a reduction of the peaks of the scan by a factor 3. The sensitivity $S/\sqrt{B}$ is thus reduced by a factor $\sqrt{3}/3 \sim 0.5$. To bring the sensitivity to the level shown in Figure 2.11, a factor 4 more statistics is then required. For this reason, the number of bins of the scan will be reduced to account for the widening due to atomic motion, and the beam intensity will be doubled.

### 2.4.1 Limits of the ETag detector

The current ETag detector does not meet the requirements needed by PADME for Run IV. The higher rate, due to the increased beam intensity, would lead to an over-occupancy of the ETag slabs, resulting in a high dead time. In fact, as can be seen in Figure 2.9b the width of the collected pulse is long roughly a quarter of the bunch length ($65$ cts correspond to $25$ ns in plot). For this reason, a few hits per bunch are enough to make the detector blind. Figure 2.12 shows the expected number of hits per bunch on the ETag slabs in the hypothesis of a doubled number of positrons per bunch ($\sim 6000$), which I obtained with the full GEANT4 PADME simulation. The predicted rate is well above $1$ hit/bunch, especially for the central slabs where the occupancy reaches $10$ hits/bunch. This has an impact on the tagging efficiency of ETag. Given the large surface area of the slabs, a charged particle hitting any part of a slab while a photon is crossing the same slab is enough for the photon to be incorrectly identified as a charged particle. In addition to this, the ETag cannot help in improving the spatial resolution, a quality that would be of great impact in tightening the cuts in the $\theta - \phi$ plot discussed earlier, thus reducing the number of background events in the candidate events sample.

### 2.4.2 Advanges of the tracker solution

To simultaneously meet PADME requirements for Run IV, a gaseous detector used as a tracker stands as the optimal solution. The use of gas as the active detector material has a twofold advantage. On one hand, it provides the lowest possible material budget due to the very low density of gases (of the order of some mg/cm$^3$), helping to prevent spatial resolution degradation due to Coulombian multiple scattering. On the other hand, the absorption length $\lambda$ for photons of the $\sim$ MeV energy, can be as high as $10^4$ cm for gases at STP, as can be estimated by the following formula [32]:

$$\frac{1}{\lambda_{STP}} \simeq 26.87 \cdot \sigma(\text{Mb}) \tag{2.5}$$

where $\sigma$ represents the cross section for photon interactions, which is dominated by Compton scattering and pair production for energies above the MeV scale.

A gaseous detector does not only provide efficient particle identification between charged particles and photons, but can also improve the spatial resolution of the

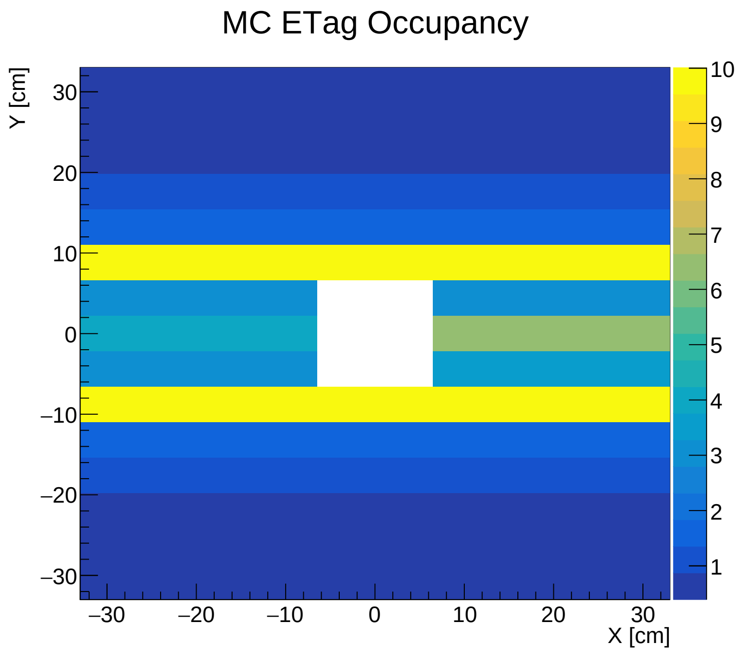


**Figure 2.12.** Average number of hits per bunch on the ETag obtained simulating 100 bunches of 6000 positrons each inside PADME Geant4 MonteCarlo.

PADME setup if a readout plane featuring high segmentation is exploited in the form of strips or pads. In particular, MicroPattern Gaseous Detectors (MPGDs) can have a readout granularity of the sub-mm level, hence reducing the spatial resolution from the $3$ mm of the ECal almost by a factor $10$. A finer segmentation also prevents tagging inefficiencies like those occurring in the ETag, where a photon could be confused with a charged particle that crossed another part of the detector at the same time.

The tracking capabilities of a gas-based detector also permit the reconstruction of the invariant mass of the final state without any assumptions about the vertex position and the measurement of the vertex position itself. These are two qualities that were previously absent in PADME, but which could now be exploited. Some estimate of these quantities will be provided in chapter 5 using the chamber simulation developed as a part of this thesis work. For these reasons PADME chose to develop a Micromegas to replace the current ETag for Run IV, in collaboration with the LNF ATLAS group.

In Figure 2.13, the results of a simple toy Monte Carlo simulation are shown. I generated a sample of $10^6$ Bhabha scattering events and the position of the impact point of the final state particles at the calorimeter front face was recorded. The position of the impact point was smeared using a Gaussian distribution with a standard deviation corresponding to the ECal spatial resolution or the tracker resolution. For the tracker, a segmentation of the readout plane at the level of $0.4$ mm was used. Then, the reconstructed four-vectors of the events inside the acceptance were boosted to the center of mass frame. The effect of Coulomb scattering due to the PADME carbon window was also taken into account. It can be seen that the use of the tracker can improve the resolution by a factor $\simeq 4$ in both $\theta$ and $\phi$ in the center of mass frame. The characteristics of this detector and its operating principle will be discussed in the following chapters.

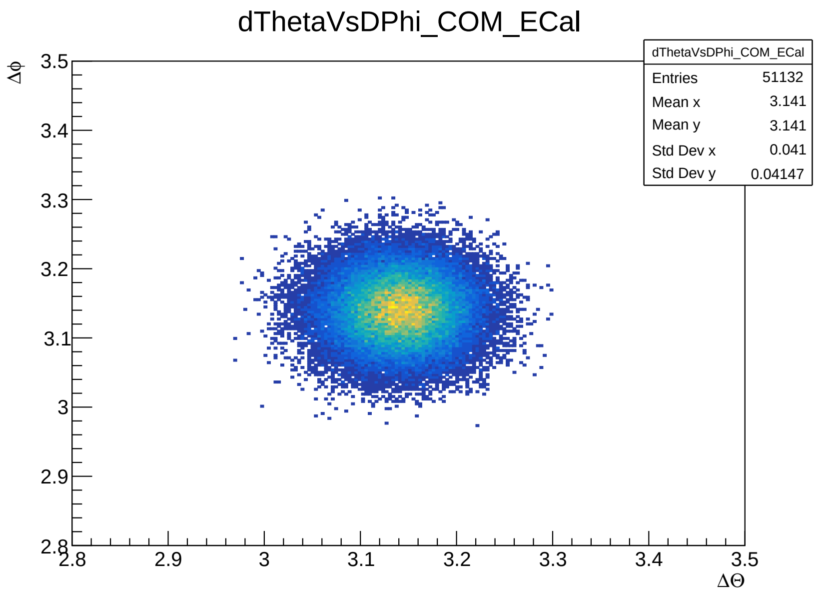


**(a)**

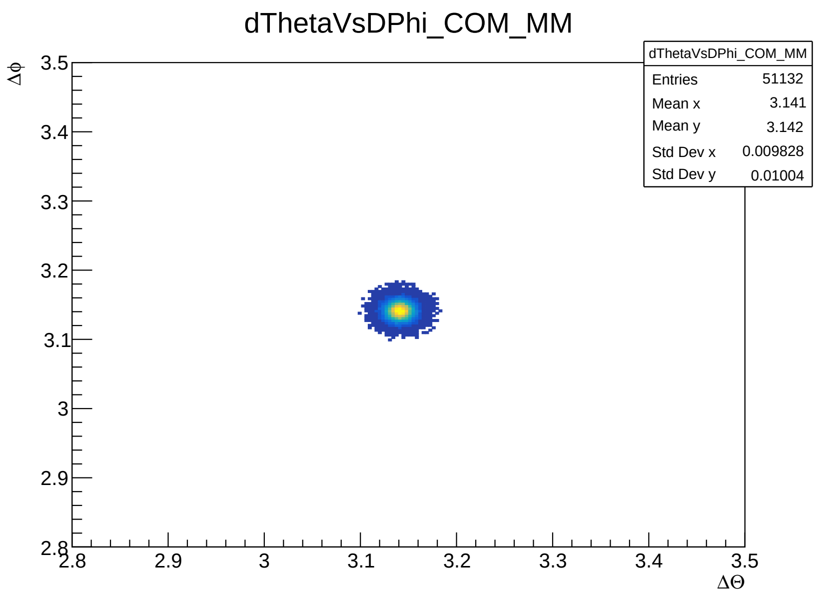


**(b)**

**Figure 2.13.** $\theta_1 + \theta_2$ vs $\phi_1 - \phi_2$ distribution for a sample of $10^6$ BhaBha scattering events including the effect of ECal spatial resolution (a) and tracker spatial resolution (b).

# Chapter 3

# Gas Detectors and the MicroMegas technology

## 3.1 Introduction to gas based detectors

Gaseous detectors are a widely used technology for particle detection and have been a crucial tool for particle physics in the 20th century. Their use began with the work of Rutherford and Townsend in the early 20th century on the interactions of charged particles in a gas. A major advancement occurred in the 1960s with the development of the multi-wire proportional chamber by Georges Charpak, which earned him the Nobel Prize and revolutionized particle tracking. Over the decades, gas detectors have continuously evolved and innovated, leading to the variety of devices used in today's high-energy physics experiments.

### 3.1.1 Ionization Energy Loss

All gas detectors are based on the same physical principle: when a charged particle passes through a medium, it deposits a certain amount of energy in it. The average energy loss from ionization, the process by which the lost energy is transferred to an electron of the material, ripping it of its atom, is described by the well-known Bethe-Bloch equation [33]:

$$\left\langle -\frac{dE}{dx} \right\rangle = Kz^2 \frac{Z}{A} \frac{1}{\beta^2} \left[ \frac{1}{2} \ln \frac{2m_e c^2 \beta^2 \gamma^2 W_{\max}}{I^2} - \beta^2 - \frac{\delta(\beta\gamma)}{2} \right] \tag{3.1}$$

where $Z, A, I$ are the atomic number, atomic mass, and mean excitation energy (in eV) of the absorber material respectively; $z$ is the charge of the incident particle and $W_{max}$ is the maximum possible energy transfer to an electron in a single collision (in MeV). K is a dimensionful constant whose value is around $0.307\ \mathrm{MeV\ mol^{-1}\ cm^2}$. This relation holds at the percent level for moderately relativistic heavy particles, in the range $0.1 \lesssim \beta\gamma \lesssim 1000$. The function for positive muon impinging on a Copper target is shown in Figure 3.1. A similar relation exists for the case in which

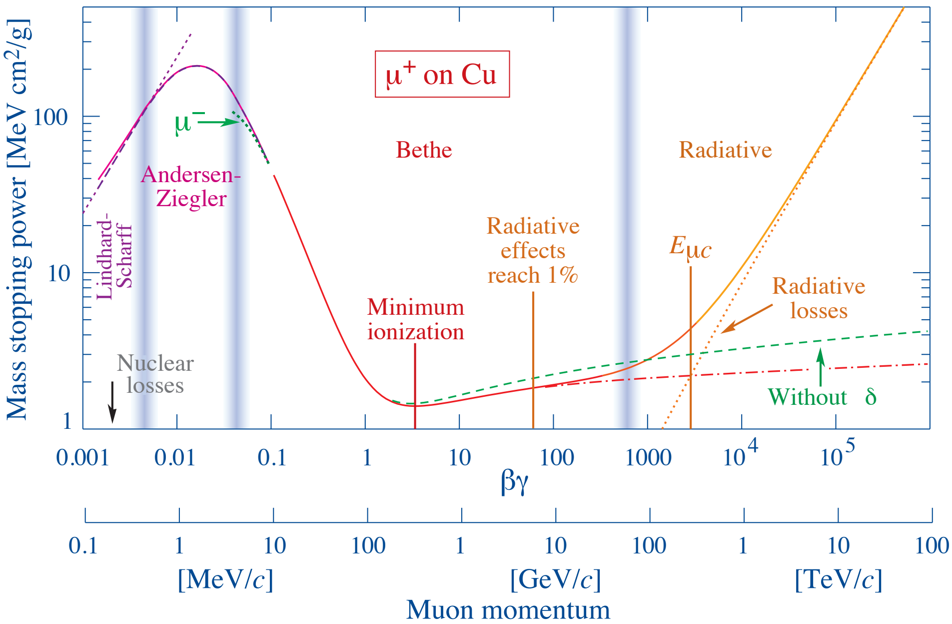


**Figure 3.1.** Average energy loss of a positive muon in a Copper target. The Bethe-Bloch model is valid in the region delimited by the vertical blue bands with the label "Bethe".

the incident particle is an electron or a positron, with the differences being due to kinematics (the collision happens between particles of the same mass), spin and charge. The distance of these ionizing collisions is random and occurs with a *mean free path* $\lambda$ defined as follows:

$$\lambda = \frac{1}{\sigma n} \tag{3.2}$$

where $\sigma$ is the cross section of the process and $n$ the number density of electrons in the target material. Usually $\lambda$ is around the $\mathrm{mm}$ scale at *Normal Temperature and Pressure conditions* (NTP) [1]. The number of the ion pairs formed along a distance L is thus distributed as a Poisson distribution with a mean value $\mu = L/\lambda$. When an electron is ejected from its atom via ionization, it can have sufficient energy to ionize other atoms, we refer to this as *secondary ionizations*. To quantify the required energy for the creation of an electron-ion pair in a particular gas, we use the ratio between the initial kinetic energy of the particle and the total number of pairs created:

$$W_I = \frac{E_i}{N_T} \tag{3.3}$$

This can be related to the energy loss via the following relation:

$$W_I \langle N_T \rangle = L \left\langle \frac{dE}{dx} \right\rangle \tag{3.4}$$

A summary of ionization properties of various gasses can be found in Table 3.1.

[1] NTP = 20 °C and 1 atm.

**Table 3.1.** Properties of different gasses at normal temperature and pressure. $E_X, E_I$ are respectively the first excitation energy and ionization energy; $W_I$ is the average energy needed for creation of ion pair; $dE/\,dx|_{\min}$, $N_P, N_T$ represent the differential energy loss, primary and total number of electron-ion pairs per $\mathrm{cm}$, for unit charge MIP. These values should be taken only as approximate [33].

| Gas | Density<br>mg $\mathrm{cm}^{-3}$ | $E_x$<br>eV | $E_I$<br>eV | $W_I$<br>eV | $dE/\,dx\|_{\min}$<br>keV$\mathrm{cm}^{-1}$ | $N_P$<br>$\mathrm{cm}^{-1}$ | $N_T$<br>$\mathrm{cm}^{-1}$ |
|---|---|---|---|---|---|---|---|
| $H_2$ | 0.084 | 10.8 | 13.6 | 37 | 0.34 | 5.2 | 9.2 |
| He | 0.179 | 19.8 | 24.6 | 41.3 | 0.32 | 3.5 | 8 |
| Ne | 0.839 | 16.7 | 21.6 | 37 | 1.45 | 13 | 40 |
| Ar | 1.66 | 11.6 | 15.7 | 26 | 2.53 | 25 | 97 |
| Xe | 5.495 | 8.4 | 12.1 | 22 | 6.87 | 41 | 312 |
| $CH_4$ | 0.667 | 8.8 | 12.6 | 30 | 1.61 | 28 | 54 |
| $C_2H_6$ | 1.26 | 8.2 | 11.5 | 26 | 2.91 | 48 | 112 |
| $C_4H_{10}$ | 2.49 | 6.5 | 10.6 | 26 | 5.67 | 90 | 220 |
| $CO_2$ | 1.84 | 7.0 | 13.8 | 34 | 3.35 | 35 | 100 |
| $CF_4$ | 3.78 | 10.0 | 16.0 | 35-52 | 6.38 | 52-63 | 120 |

It should be noted, however, that the Bethe-Bloch theory only describes the average energy loss of a charged particle inside a material. Event by event the lost energy fluctuates around the average following a distribution first studied by Landau in the forties [34], and depending on the material thickness and atomic properties. For thin gas absorbers, the distribution shows a characteristic asymmetric tail for large values. The formula for the distribution has an integral form with imaginary integration boundaries, so for simplicity we report a well-known approximation due to Moyal [32]:

$$f(\lambda) = \frac{1}{\sqrt{2\pi}} \mathrm{e}^{-\frac{1}{2}\left(\lambda + \mathrm{e}^{-\lambda}\right)} \tag{3.5}$$

where $\lambda$ is the energy loss normalized to the most probable energy loss:

$$\lambda = \frac{\Delta E - \Delta E_{\mathrm{MP}}}{\xi}, \quad \xi = K \frac{Z}{A} \frac{\rho}{\beta^2} x \tag{3.6}$$

### 3.1.2 Transport of electrons and ions

In the absence of an external force, electrons ejected from the atom by ionization would be quickly reabsorbed by the gas molecules. For this reason gaseous detectors use an electric field to collect these charges and produce a signal in the form of an induced charge on electrodes (see section 3.2). One of the simplest type of such a detector is a parallel plate counter, shown in Figure 3.2: the gas volume is placed between the two electrodes that provide the electric field; the produced electron-ion pairs move towards the electrodes (electrons to the anode, positive ions to the cathode) and the induced charge is read as a current via an amperometer.

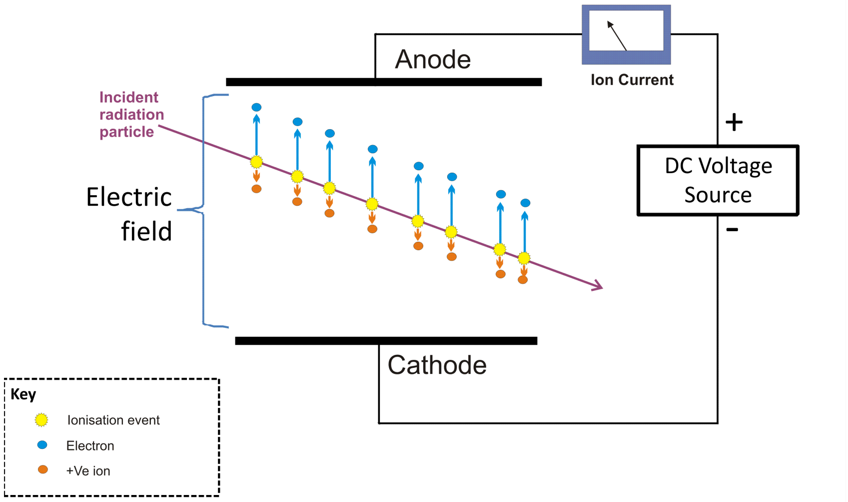


**Figure 3.2.** Schematic drawing of a parallel-plate counter gaseous detector and its functioning.

In other kinds of detectors the electrodes are segmented, namely they are divided in pieces in the form of wires, strips or pads. These are the so called *position sensitive* detectors because by measuring the amount of charge collected on the different elements we can infer where the particle has passed. The strength of the drift field defines the operation mode of the detector: for relatively weak fields we are in the so called *recombination region* where the field is not strong enough to prevent electrons to be captured by the gas molecules. Most gas-based detectors work in the *proportional region* in which the charge collected depends linearly on the applied voltage; if the field grows large we eventually reach the *Geiger-Muller* region in which electrons from ionization can gain enough energy to initiate an avalanche, leading to a multiplication of charge. This last operation mode is the one used in many radiation counter devices known in fact as Geiger-Muller counters.

Actually, as the ionization products travel to the electrodes under the influence of the Lorentz force, they bounce off other molecules. On average, this effect can be modelized macroscopically by introducing a "viscosity" term in the equation of motion [35]:

$$m\frac{d\vec{v}}{dt} = q(\vec{E} + \vec{v} \times \vec{B}) - K\vec{v} \tag{3.7}$$

where $q$ and $m$ are the particle charge and mass and $\vec{v}$ is called *drift velocity*. The constant $K$ has the dimensions of a mass divided by a time, then it is convenient to define a characteristic time $\tau = m/K$, which at the microscopic level can be seen as the typical time between collisions. The net result is the reaching of an equilibrium condition where the drift velocity is constant. In the absence of a magnetic field, this condition reads as follows:

$$q\vec{E} = \frac{m}{\tau}\vec{v} \tag{3.8}$$

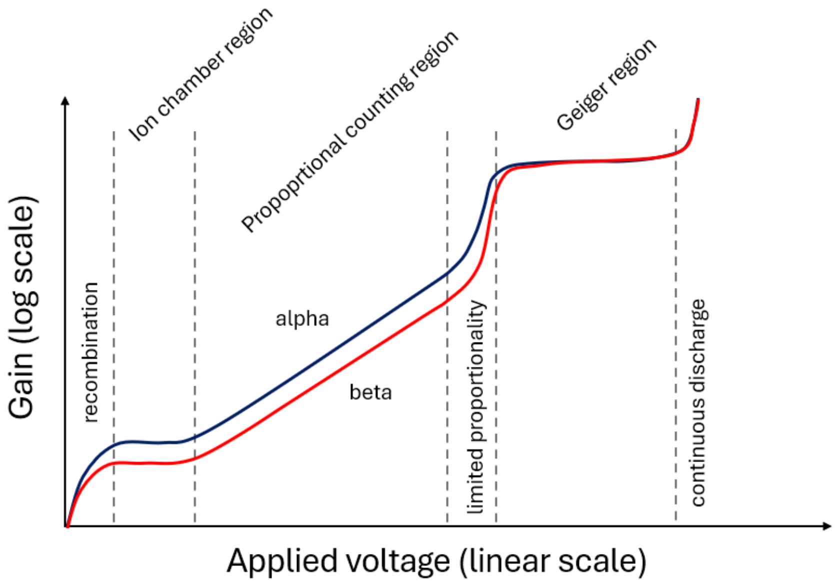


**Figure 3.3.** Gain versus applied electric field. Different regimes are separated by vertical dotted lines.

And therefore the drift velocity can be written as:

$$\vec{v} = \frac{q}{m}\tau\vec{E} \tag{3.9}$$

Another way of expressing this is by using the notion of mobility $\mu$:

$$\mu = \frac{q}{m}\tau \quad \Longrightarrow \quad \vec{v} = \mu\vec{E} \tag{3.10}$$

Let us for a moment consider only the drifting electrons. At the microscopic level, the electrons have an instantaneous velocity $\vec{u}$ which has a random direction due to the light mass of the electron, and an additional drift velocity $\vec{v}$ due to the acceleration by the electric field between two collision. The equilibrium condition we mentioned earlier is reflected at the microscopic level too if we consider the following argument. During a drift distance $x$ the electric field gives to the electron an energy $T = qEx$. In the same length a number of collisions $n = x/(v\tau)$ happen, in each of which a fraction $\lambda$ of the electron energy is lost due to recoil or by ionization. Therefore the equilibrium energy due to the electric field $\varepsilon_E$ can be defined as:

$$\frac{x}{v\tau}\lambda\varepsilon_E = qEx \tag{3.11}$$

In normal conditions the Compton wavelength of the electron $\lambda = \hbar c/mc^2$ is much smaller than the distance between gas molecules; this allows us to employ a classical treatment and examine the scattering process in an atomistic manner. Therefore the characteristic time $\tau$ becomes:

$$\frac{1}{\tau} = N\sigma u \tag{3.12}$$

where the cross section is denoted with $\sigma$ and $N$ is the number density of gas molecules. By combining (3.9), (3.11) and (3.12) in the limit in which the thermal energy of the electron is much lower than the one due to electric field acceleration so that:

$$\varepsilon = \frac{1}{2}mu^2 = \frac{3}{2}k_B T + \varepsilon_E \simeq \varepsilon_E \tag{3.13}$$

we obtain the expressions for both instantaneous and drift velocity:

$$\begin{aligned} v^2 &= \frac{eE}{mN\sigma}\sqrt{\frac{\lambda}{2}} \\ u^2 &= \frac{eE}{mN\sigma}\sqrt{\frac{2}{\lambda}} \end{aligned} \tag{3.14}$$

Note that in principle the fractional energy loss $\lambda$ and the cross section $\sigma$ depend on the energy $\epsilon$ of the electron. For the drift of ions the story is somehow different, primarily because of their larger masses compared to electrons. To see this, consider the scattering between two particles with masses $m$ and $M$, the first being the drifting particle and the second a gas molecule. In the laboratory frame the particle $M$ is at rest and $m$ has a momentum $P$. Limiting to non-relativistic elastic scattering, in the center of mass frame the following relations hold:

$$\vec{p}_m = -\vec{p}_M \quad \text{and} \quad |\vec{p_i}| = |\vec{p_f}| = m|\vec{v}| \tag{3.15}$$

where $\vec{v}$ is given by $\vec{v} = P/(M+m)$. The four-momentum transfer squared is Lorentz invariant and in the center of mass frame is:

$$(\mathbf{p}'_m - \mathbf{p}_m)^2 = -2p_m^2(1-\cos(\theta^*)) \tag{3.16}$$

This is equal to the four-momentum transfer squared of the particle at rest in the laboratory:

$$(\mathbf{p}'_M - \mathbf{p}_M)^2 = -2ME_{kin}^M \tag{3.17}$$

Averaging over all angles in the *Center of Mass* frame (COM) we get:

$$E_{\text{kin}}^M = \frac{p^2}{M}(1-\cos\theta^*) \quad \Longrightarrow \quad \langle E_{kin}^M \rangle = \frac{p_m}{M} \tag{3.18}$$

And finally the fractional energy loss becomes the ratio between this kinetic energy and the kinetic energy of the incoming particle:

$$\lambda = \langle E_{kin}^M \rangle \frac{2m}{M} = \frac{2mM}{(M+m)^2} \tag{3.19}$$

For an electron $m \ll M$ so the loss is small, of the order of $10^{-4}$; but for ions $m \simeq M$ and the fractional loss becomes $\frac{1}{2}$. This means that for an ion almost all the energy gained through the electric field is lost in the next collision and therefore the energy of the ions is basically only the thermal one. Typical values for the drift velocity are 10 cm/$\mu$s for electrons and 10 cm/ms for ions.

### 3.1.3 Diffusion

There is another important aspect in the description of how a gas-based detector works; as mentioned earlier, electrons and ions move towards the electrodes with an average drift velocity. However, due to their thermal energy, their spatial distribution will spread over time. This phenomenon is called *diffusion* and in the simplest model is described with a gaussian PDF having a $\sigma$ increasing with time:

$$\mathcal{N} = \left(\frac{1}{\sqrt{2\pi\sigma^2}}\right)^3 e^{-r^2/(2\sigma^2)} \quad \text{with} \quad \sigma^2 = 2Dt \tag{3.20}$$

where $D$ is called *diffusion coefficient* and $r^2 = x^2 + y^2 + (z - ut)^2$ for a drift along the $z$ direction. Notice that the standard deviation is proportional to $\sqrt{t}$ which represents a reminiscence of the random walk nature of this phenomenon. In our microscopic model the diffusion coefficient is given by:

$$D = \frac{2}{3}\frac{\varepsilon}{m}\tau \tag{3.21}$$

and by using (3.10) and $t = L/v$:

$$\sigma = \left(\frac{4}{3}\frac{\epsilon}{q}\frac{L}{E}\right)^{\frac{1}{2}} \tag{3.22}$$

From (3.22) it is clear that the effect of diffusion grows with large drift distances $L$ and decreases by using stronger electric fields. At this point we analyzed the ionization mechanism and how the drifting particles travel to the electrodes. The amount of charge released would create a signal that is too weak to be detected or handled by regular electronic devices. So, we need to amplify the signal to make it stronger and easier to work with. This will be the topic of the next section.

### 3.1.4 Amplification of primary ionization

Before using electronics, we can obtain amplification by multiplying the number of drifting particles inside the detector itself. Applying a strong enough electric field, the electrons produced by primary ionization can collide with other gas molecules, producing additional free electrons. This multiplication phenomenon, known as an *avalanche*, was discovered by Townsend in the early 1900s during his studies on gas interactions.

Different detectors produce avalanches in different ways. In wire chambers for example, the cathode is made of thin wires set to a specific voltage and the electric field has the form:

$$E = \frac{\lambda}{2\pi\varepsilon_0}\frac{1}{r} \tag{3.23}$$

The avalanche occurs naturally as the drifting electrons travel towards the wire, where the field increases. In other detectors, like in Micromegas or Time Projection Chambers the amplification takes place in a narrow region near the electrodes where a stronger electric field, of the order of tens of kV/cm, is used. In the simplest model, we can assume that the infinitesimal change in the number of electrons over an infinitesimal distance $ds$ in the avalanche is:

$$dN = \alpha N ds \tag{3.24}$$

where $\alpha$ is called the first Townsend coefficient and represents the probability per unit length for an electron to generate secondary electrons in the avalanche development.

No analytical expression can predict the Townsend coefficient, which is usually measured for each gas mixture. Integrating the above expression in the hypothesis of constant $\alpha$ we obtain the number of electrons in the avalanche after a distance $d$:

$$N = N_0 e^{\alpha d} \tag{3.25}$$

$\alpha$ is typically not a constant but depends on the electric field. While $\alpha$ also depends on the properties of the gas, we assume these to remain constant within the detector volume. Thus, the proper integration yields:

$$N/N_0 = \exp \int_{s_{\min}}^{a} \alpha(s)\mathrm{d}s = \exp \int_{E_{\min}}^{E(a)} \frac{\alpha(E)}{\mathrm{d}E/\mathrm{d}s}\,\mathrm{d}E \tag{3.26}$$

where $E_{min}$ is the minimum threshold field required to start an avalanche and $a$ is the final point of the trajectory. The gain is defined as the ratio $G = N/N_0$ with $N_0$ being the initial number of electrons. Photons play an important role in the description of the avalanche because the ionization and excitation cross-sections are of similar magnitude. When gas atoms or molecules relax to a lower energy state, they usually emit a photon in the UV region. If the energy of these photons is high enough they can ionize other gas molecules creating electrons that will evolve in another avalanche.

These photons can travel beyond the typical spatial extent of the avalanche, potentially compromising the detector's spatial resolution. To overcome this problem, the so called *quenching gases* are added to the gas mixture. They are organic compounds with a high photon absorption cross-section across a wide range of frequencies, thus limiting unwanted ionizations from photons to occur.

## 3.2 Signal formation mechanism

We briefly mentioned earlier that in gas detectors the signal is due to the current induced on the electrodes by the drifting particles. In this section we want to analyze more in detail the principles and the laws describing signal formation. However,

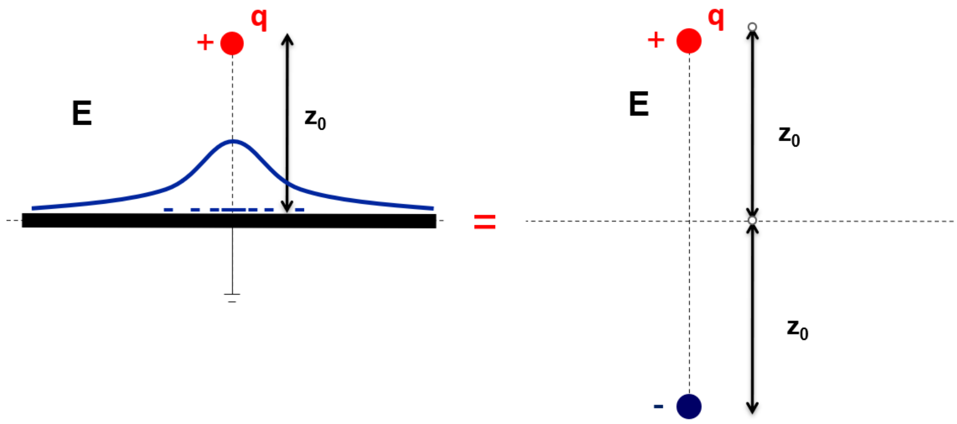


**Figure 3.4.** Configuration with grounded metallic plate and positive charge at a distance $z_0$ and its equivalent configuration via mirror charge. Figure adapted from the CERN Detector Seminar held by Werner Riegler in 2008.

the equation describing the current depends on the particular geometry of the electrodes, and can easily become too complicated to be computed analytically. For this reason numerical solutions obtained by simulations programs (i.e. *Garfield*++) are often used. We will only sketch how this process works, and describe the simple case of a drift tube. It is well known that moving charges induce a current on conductive bodies. For example if we consider a grounded metallic plate, with $V = 0$, and a charge $q$ at a distance $z_0$ from it, the electric field on the conductor surface is found by solving the Poisson equation for the potential via the *mirror charge* method. This consists in finding a proper electrostatic configuration which mimics the one we want to solve but which is simpler to study. In our case we place a mirror charge $-q$ in $-z_0$ so that the potential in the position of the plate is null by construction (see Figure 3.4). The electric field on the plate will then be:

$$E_z(x, y) = -\frac{qz_0}{2\pi\varepsilon_0 \left(x^2 + y^2 + z_0^2\right)^{\frac{3}{2}}} \qquad E_x = E_y = 0 \tag{3.27}$$

Using Coulomb's theorem $\sigma = \epsilon_0 E$ we find the surface charge distribution on the conductor. The total induced charge, found by integrating $\sigma$ over the plate volume correspond exactly to $-q$. If the electrode is segmented, namely it is divided into smaller units like strips for example, the charge distribution does not appreciably change. Now suppose that the charge $q$ moves along a trajectory **x**(t), in this case the charge induced on each element of the plate will change with time, thus resulting in a current between the electrodes and ground as can be seen in Figure 3.5.
The general problem of finding the induced current on a set of electrodes is formulated using the well-known Ramo's Theorem. Before reaching that point, lets consider N electrodes, each set to a voltage $V_n$. The charges $Q_n$ on the electrodes

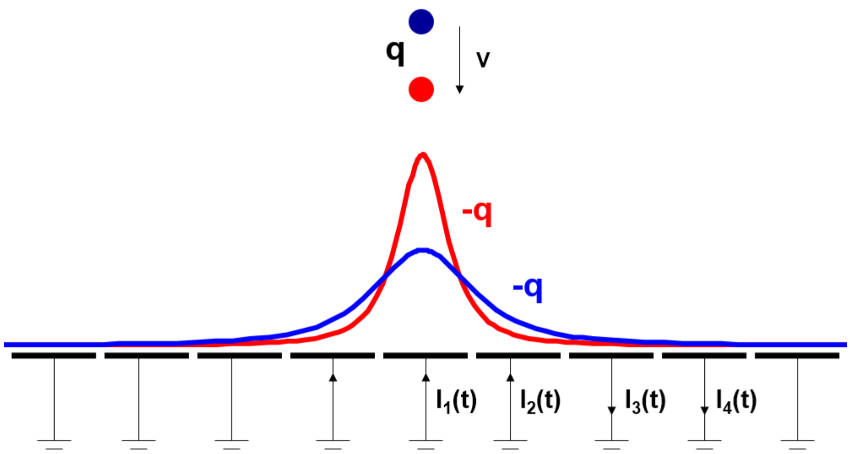


**Figure 3.5.** Current induced by a moving charge on a segmented electrode connected to ground. Credits to Werner Riegler, CERN Detector Seminar (2008).

are connected to the voltages by the capacitance matrix in the following way [36]:

$$Q_n = \sum_{m=1}^{N} c_{nm} V_m \tag{3.28}$$

Since the capacitance matrix elements only depend on the specific electrodes geometry, the same relation holds for another set of voltages $\bar{V}_n$ and the corresponding charges $\bar{Q}_n$ in such a way that we can write:

$$\sum_{n=1}^{N} Q_n \bar{V}_n = \sum_{n=1}^{N} \bar{Q}_n V_n \tag{3.29}$$

This represent the statement of the so called *reciprocity theorem*. To prove Ramo's Theorem take a set of $N$ grounded electrodes in the presence of a point charge $q$ and imagine it sitting on an infinitesimally small electrode. In this configuration we then have a charge $Q_0 = q$ on the electrode upon which the charge sits which results in a voltage $V_0$, while all the other electrodes are set to $V_i = 0$. Take now another electrostatic configuration without the charge $q$ and with all electrodes to ground potential except for one which we put at voltage $\bar{V}_1 = V_w$, reciprocity theorem tells that:

$$Q_0\bar{V}_0 + Q_1\bar{V}_1 = \bar{Q}_0 V_0 = 0 \quad \rightarrow \quad Q_1 = -q\frac{\bar{V}_0}{V_w} \tag{3.30}$$

The voltage $\bar{V}_0$ is the potential at that point in space generated by the electrode 1, since we removed $q$ and it is therefore called *weighting potential* $\psi_1(\mathbf{x})$. If the charge $q$ moves along a trajectory we find the induced current by derivating the above expression with respect to time:

$$I_n(t) = -\frac{dQ(\mathbf{x}(t))}{dt} = \frac{q}{V_w}\frac{d}{dt}\psi_n(\mathbf{x}(t) = \frac{q}{V_w}\nabla\psi_n(\mathbf{x})\mathbf{v}(t) = -\frac{q}{V_w}\mathbf{E}_n[\mathbf{x}(t)]\mathbf{v}(t) \tag{3.31}$$

This is the basic content of Ramo's Theorem and allows to compute the time evolution of the signal induced by the drifting particles on the electrodes of a gas detector. Practical situations are more complex than this since usually the electrodes are not grounded but they belong to an electronic network made of resistors, capacitors amplifiers, etc... It can be proved that to analyze this situation one has to follow these steps:

1. Compute the trajectories of the drifting particles due to the particular electric field configuration in the detector.
2. Calculate the induced currents on the grounded electrodes using Ramo's Theorem.
3. Place these currents as ideal current sources in the equivalent circuit diagram of the detector with an impedance matrix $z_{nm}$.

## 3.3 MicroMegas working principle

Micromegas is a parallel-plate gaseous detector with a narrow amplification gap near the electrodes, typically between 50 and 100 $\mu\mathrm{m}$ [37]. This region is defined by the anode, where the electrons drift to, and a thin metallic mesh, few tens of microns thick, acting as a cathode. An electric field usually above $30\,\mathrm{kV\,cm^{-1}}$ is applied between the anode and the mesh, significantly larger than the field applied in the drift region. In such conditions an *avalanche effect* is reached when drifting electrons gain enough kinetic energy to ionize other atoms in a chain reaction, providing a multiplication of the number of drifting electrons and therefore the amplification of the signal to a level that the electronics can work with. The reason behind the use of such a small gap is due to the behavior of many gas mixtures at atmospheric pressure, that presents a maximum of the gain as a function of the amplification gap width around 50-100 $\mu\mathrm{m}$.

The main technological difficulty of Micromegas is to maintain a constant gap size across all of the mesh surface, especially for large areas, and for this reason insulating pillars are deposited on the anode or the cathode using a technique called photolithography. The electrode is laminated with a photoresistive film of the right thickness and the mesh itself at high temperature. Photoresistive materials harden when exposed to UV light so, by placing a mask with the pillar pattern on top of the mesh, the reaction only occurs in correspondence with the pillars' positions. The mask is then removed together with the non-hardened film leaving only the pillars [38].

After this process, the application of the mesh can be done in two ways. The mesh can be embedded into the pillars so that it cannot be removed anymore; we refer to Micromegas built with this technique as *bulk Micromegas*. Another possibility is to have the mesh only rested on the pillars, a layout known as *floating*

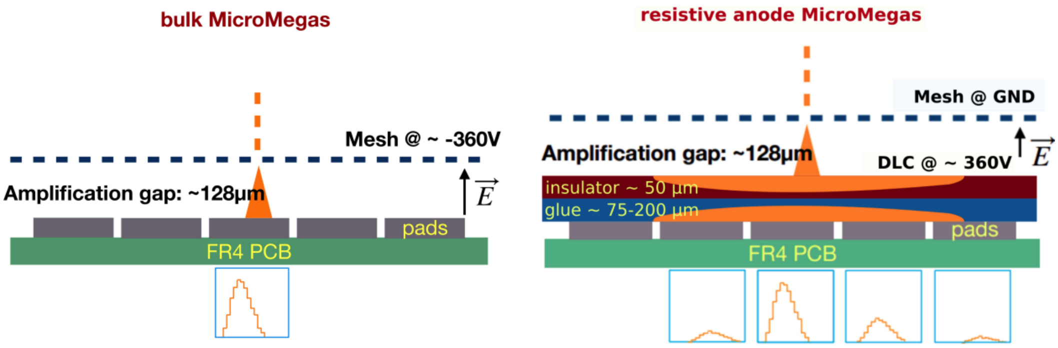


**Figure 3.6.** (Left) Schematic illustration of the working principle of a standard Micromega detector. (Right) Scheme of a Resistive Anode Micromegas, a detail of the spread of the signal to the neighbouring anode elements as a function of time is also shown [39].

*mesh Micromegas*. This construction process allows to disassemble the mesh from the anode in order to perform detector maintenance and cleaning.

Micromegas are also *position sensitive detectors*, so it is possible to know where the incident particle hit the detector and its direction. This is achieved by segmention of the anode into strips or pads so that, depending on the position of the ionization, the drifting charges are collected by different anode elements. A schematic drawing of a Micromegas detector can be seen in the leftmost part of Figure 3.6.
The signal on the anode elements and on the cathode mesh comes from the induced current due to the drifting charges moving in the detector volume as already discussed in detail section 3.2. Since ions and electrons have different mobilities, the first being around $10^3$ times smaller than the second, the charge signal is mainly due to the ions while electrons are responsible for a faster current signal with a time around or less $1\,\mathrm{ns}$. To see this it is sufficient to remember the definition of current $I = dQ/dt$, from which we can see that particles with an higher drift velocity (and hence an higher mobility) will produce an higher current because the same amount of charge flows in a smaller time to the electrodes. Typical values for the gain are of the order of $10^4$ so, in the case of a single electron for example, the avalanche will produce a charge $\sim 10^{-15}$ C . Therefore, if the drift time of these electrons is around $1\,\mathrm{ns}$, the current will have a value of the order of $0.1\,\mu$A which can be handled by the amplifier electronics.

A newer type of Micromegas, the so-called *Resistive Anode Micromegas*, have an additional insulating layer on top of readout elements and covered by a thin resistive foil. This serves two main purposes: firstly, the presence of a resistive elements spreads the deposited charge on neighboring anode elements, greatly improving the nominal spatial resolution due to the uniform distribution ($\sigma = pitch/\sqrt{12}$). In fact the resistive layer acts as a 2D RC-circuit in which the deposited charge spreads with time following a Gaussian distribution. For a charge deposited at $t = 0$ and $r = 0$, the charge density is given by:

$$\rho(r,t) = \frac{RC}{4\pi t} e^{\frac{-r^2 RC}{4t}} \tag{3.32}$$

In this context $R$ is the resistivity per unit area of the resistive layer, and $C$ is the capacitance between the resistive layer and the anode, ultimately controlled by the insulating layer thickness and material. Secondly it reduces the formation of sparks because in the presence of an intense avalanche, the voltage locally drops, effectively quenching the discharge. Moreover the separation of the resistive layers from the anode elements, ensure their protection against sparks, since the signal is induced on them through capacitive coupling [40]. For a visual comparison between the operational principle of standard and resistive Micromegas see Figure 3.6.

## 3.4 The PADME Micromegas detector design

As anticipated in section 2.4, for Run IV PADME needs a new detector with tracking capabilities, with very well-defined properties:

- High rejection efficiency to neutral final states
- Low material budget (below few $\%X_0$)
- High precision in reconstruction of spatial coordinates ($\sim 80 - 100$ $\mu$m)
- Compatibility with PADME acquisition window ($\sim 1\mu$s)

The chosen design, developed in collaboration with the LNF-ATLAS group, is shown in Figure 3.7. It is a floating-mesh resistive Micromegas with a $10$ cm long drift gap, and a $0.128$ mm wide amplification gap on both sides. The transverse dimensions of the chamber are $65 \times 65$ cm$^2$, in order to completely cover the ECal acceptance region. The drift gap is separated from the amplification regions by a stainless steel mesh kept at positive voltage.

The drift region is divided into two identical $5$ cm sections by a third stainless steel mesh, which serves as the negative voltage cathode. The meshes have an 18$\times$45 pattern, which means that the wire of which it is composed have an $18\mu$m diameter and are spaced by $45\mu$m.
To fill the chamber a mixture of $ArCF_4$Iso, in the proportions 88:10:2, has been chosen due to its high drift speed ($\sim 10.5$ cm/$\mu$s), mainly influenced by the fraction of carbon-tetrafluoride which is the fastest component in the mixture. $CF_4$ has been studied extensively for operation of gaseous detectors because of its low diffusion and the property not to form polymers on the electrodes, and even removing them due to its etching capabilities. Isobuthane acts instead as a quencher, absorbing photons coming from the Argon de-excitations, allowing for operation at high gain operation and more stability [32]. This mixture also provides an high cluster density (the inverse of the mean free path $\lambda$) of roughly $3$ ionizations/ mm, which helps in

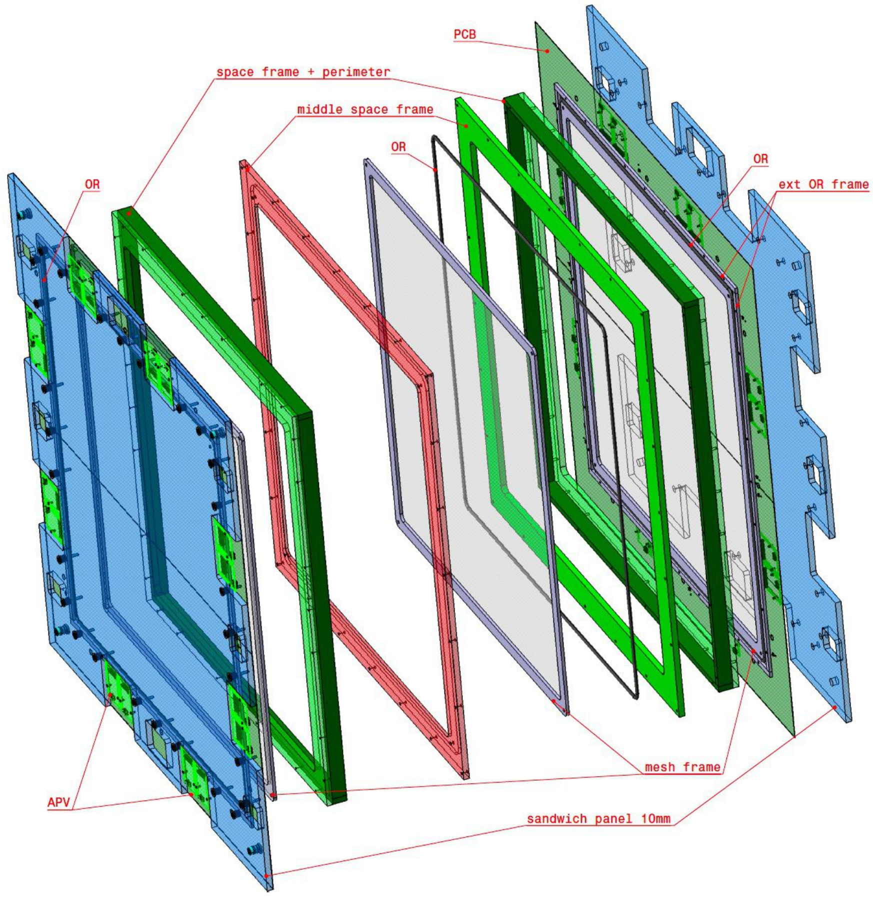


**(a)**

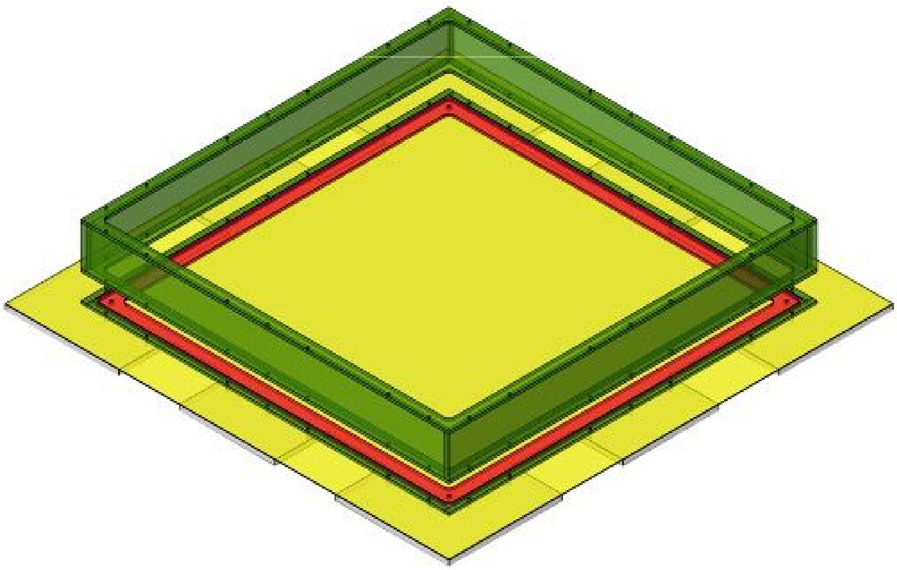

**(b)**

**Figure 3.7.** (a) Strip-based readout plane scheme. The strip can be seen as the horizontal white lines. (b) Rhomboic strip based readout plane scheme. The strips for the y coordinate are green, while the one for the x coordinate are purple.

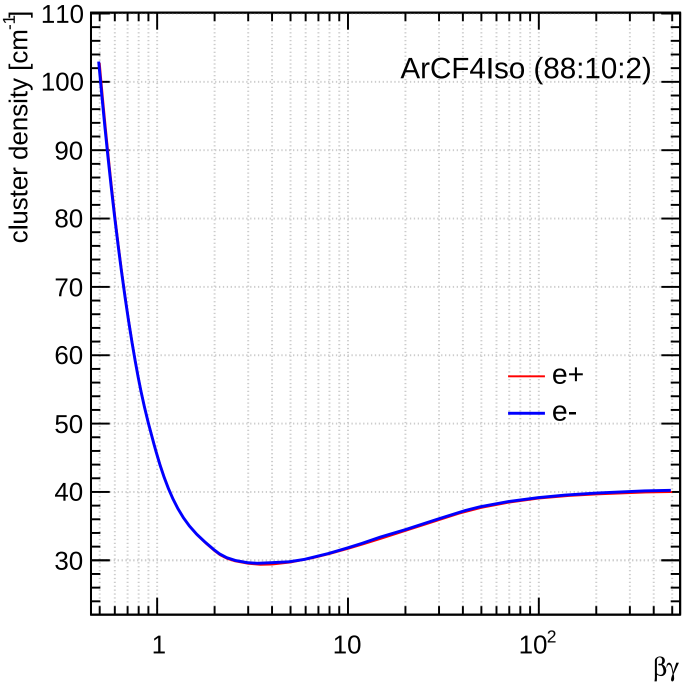


**Figure 3.8.** The cluster ionization density for $ArCF_4Iso$ as a function of $\beta\gamma$ for both electrons and positrons.

collecting a large number of points per track, improving spatial resolution. This value was double-checked using a *Garfield*++ simulation (see Figure 3.8).

The gas mixture will be operated slightly above atmospheric pressure, in order not to contaminate the mixture in the case of a loss. The drift speed of the mixture, together with the chosen size for the drift gap, assures a signal collection time of around $0.5\mu$s for perpendicular tracks, which optimally fits in the PADME acquisition window.

The anode is made of two readout panels, one on the frontal face and one on the rear face of the chamber, each one with two orthogonal readout coordinates. A cathode mesh is placed in the middle of the $10$ cm gas gap to separate it into two drift regions. Each readout panel collects the charges drifted inside one of the two $5$ cm gaps and amplified in the $128$ $\mu$m amplification region defined by a metallic mesh.

The panels are composed by the following elements, ordered starting from the outermost element to the innermost one:

- Copper shield (18 $\mu$m): used due to its high Z mainly to limit the passage of $\gamma$ and x-rays in the detector active volume.
- FR4 ($0.5$ mm) + Nomex ($1$ cm): these layers furnish stiffness to the Micromegas structure, avoiding mechanical deformation. The use of honeycomb Nomex

also guarantees a minimal amount of material in between the particles trajectory.

- FR4 ($0.5$ mm): used as the basis for printing the actual readout layers circuit.
- Copper (2 $\times$18 $\mu$m): These layers form the segmented anodes for measuring the x and y coordinates, and are separated by a $50\mu$m layer of Kapton, which acts as insulation between the two copper layers, preventing discharges by lowering the electric field between them.
- Carbon ($4\mu$m): this forms the Micromegas resistive layer and is separated from the previous conductive layer by a $50\mu$m kapton layer.

The readout layers have been designed with two different segmentation styles:

1. *Strips-based*: Each readout layer is made of parallel Copper strips with $0.4$ mm pitch (see Figure 3.9a). This is a very well-known technology that can reach spatial resolution of $\sim 300$ $\mu$m on the layer facing the amplification gap. On the second coordinate, however the resolution rises to the level of $1$ mm. This effect is caused by the induced charge from the strips of the upper layer (towards the chamber).
2. *Rhomboic strips-based*: This is a new technology relying on rhomboidal shaped strips with $1.1$ mm pitch (see Figure 3.9b). The $x$ and $y$ layers will be shifted so that their rhomboids do not overlap. This solution is developed to minimize the capacitive coupling between the two layers and have the same resolution of $\sim$ $300$ $\mu$m on both coordinates. The pads have different areas, around $0.49$ mm$^2$ for the $x$ coordinate and $0.25$ mm$^2$ for $y$. This is done to equalize their different capacitive coupling to the resistive layer, due to the increased amount of Kapton foils in between.

A prototype of the strip-based detector design, featuring a 5 cm drift gap and a single readout plane with a single layer of strips was tested during two tests beam at the Beam Test Facility of Frascati National Laboratories. This will be discussed in detail in the next chapter. Since no prototype of the rhomboidal-strip design was available at the time when tests were carried out, it will not be discussed in the following.

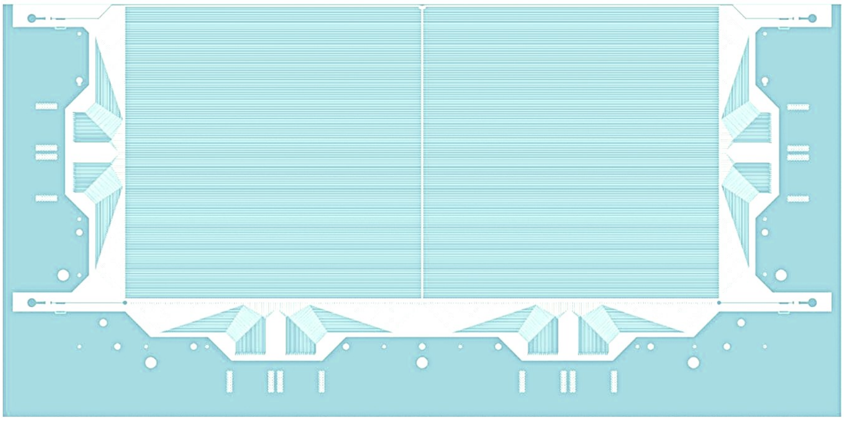

**(a)**

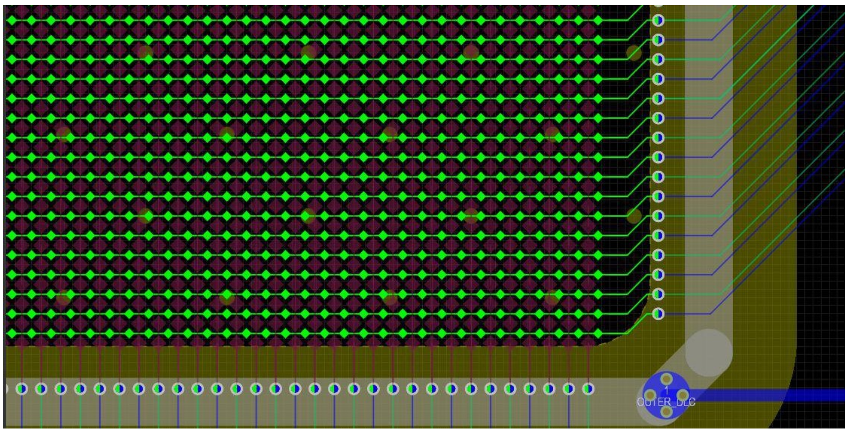

**(b)**

**Figure 3.9.** (a) Strip-based readout plane scheme. The strip can be seen as the horizontal white lines. (b) Rhomboic strip based readout plane scheme. The strips for the y coordinate are green, while the one for the x coordinate are purple.

# Chapter 4

# The padMMe Tracker

Prior to the construction of *padMMe* (MicroMegas for PADME), a prototype of the strip-based layout (see 3.4) was built and tested during two tests beam at LNF-BTF in November 2023 and May 2024. The objective of these tests was to demonstrate the detector's cability to operate in micro-TPC mode, examine the characteristics of the gas mixture, evaluate the resolution in the drift coordinate $z$, and identify the optimal detector working point in terms of its amplification and drift voltages. In this context, I was engaged in experimental activities pertaining to the configuration of Micromegas and DAQ systems, as well as the subsequent analysis of the collected data.

This chapter will focus on the experimental activities conducted to test the detector and the readout. Subsequently, the description of the analysis of the collected data and of the software I developed for this task will be presented. Finally the results of the analysis will be described.

## 4.1 Test Beam at LNF

The prototype of the PADME Micromegas was tested during two one-week long tests beam at the Beam Test Facility of Frascati National Laboratories with a $\sim 500$ MeV electron beam in single-electron mode, i.e. with very low multiplicity. A very narrow beam was used with a beam spot of the order of the millimeter. The experimental setup is shown in Figure 4.1 and is composed of two different chambers:

- A *Test MicroMegas*, to which we will refer to as *TMM*, used as a reference. It is a $10 \times 10$ cm$^2$ bulk Micromegas with a $5$ cm drift gap. The readout plane is composed of two layers of parallel strips (with $250$ $\mu$m pitch), oriented in perpendicular directions to measure both $x$ and $y$ coordinates. The chamber is positioned so that its face is orthogonal to the direction of the incoming beam.
- The prototype chamber, will be called in the following *ExMe* (Exchangeable Mesh), since it is produced with the floating-mesh technique. The ExMe is

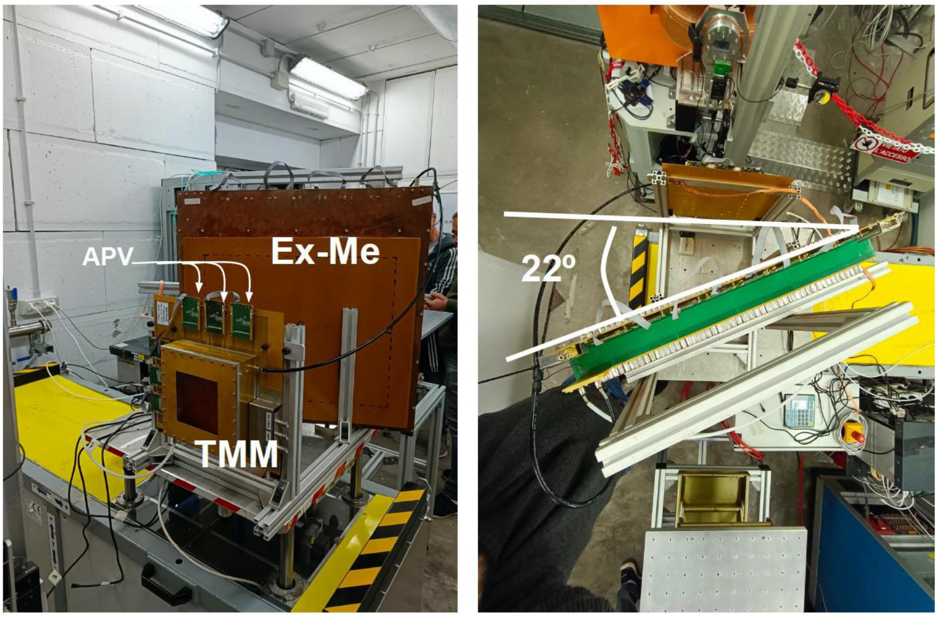


**Figure 4.1.** A photo of the setup taken during November 2023 Test Beam. The TMM is in the foreground and perpendicular to the incoming beam. The ExMe is in the background and tilted by 22° around its vertical axis.

a resistive Micromegas with an area of $50 \times 40$ cm$^2$ and a $5$ cm drift gap, so it represents one half of the final padMMe detector. The readout plane is composed of a single layer of vertical strips, with a pitch of $0.4$ mm, which are used to measure the $x$-coordinate. The detector is situated at a distance of $\sim 10$ cm behind the TMM, at an angle of $\sim 22°$ with respect to the TMM face.

The ExMe chamber is tilted to study the capability of the detector to reconstruct inclined tracks through a technique called *micro-TPC* ($\mu$TPC), which aims at using the small gap of the MicroMegas as a miniaturized Time Projection Chamber. This allows to reconstruct the 3D trajectory of the particles in the detector by combining the spatial information on the $x$ and $y$ coordinates given by the segmentation of the readout plane with the information on the $z$ coordinate, obtained by measuring the time needed for the drift electrons to reach the readout plane and multiplying it by the drift velocity.

Two datasets have been collected to study detector properties:

1. *High-Voltage Scan*: 10 runs at different values of the ExMe amplification voltage in the range $[350, 510]$ V to study the dependence of the efficiency on the amplification voltage and find the optimal working point.

2. *Drift Voltage Scan*: 6 runs at different values for the ExMe drift gap voltage within the range $[2500, 4000]$ V to study the drift field dependence of the drift speed.

Each run has a statistics of around $\sim 50k$ electrons impinging on the setup to keep the statistical error under control, around the percent level. Most of the illustrative plots shown in this section were obtained using run 2124 of May 2024 Test Beam, which was taken using an amplification voltage of 490 V and a drift 3000 V, which were later on found to be near the optimal working point of the detector.

## 4.2 Readout chain

Both chambers are read with a setup based on the *Scalable Readout System* (SRS), developed by RD51 CERN collaboration as a versatile Data Acquisition (DAQ) solution compatible with a large variety of front-end electronics and detector complexities [41]. An illustrative drawing of the SRS layout is shown in Figure 4.2.

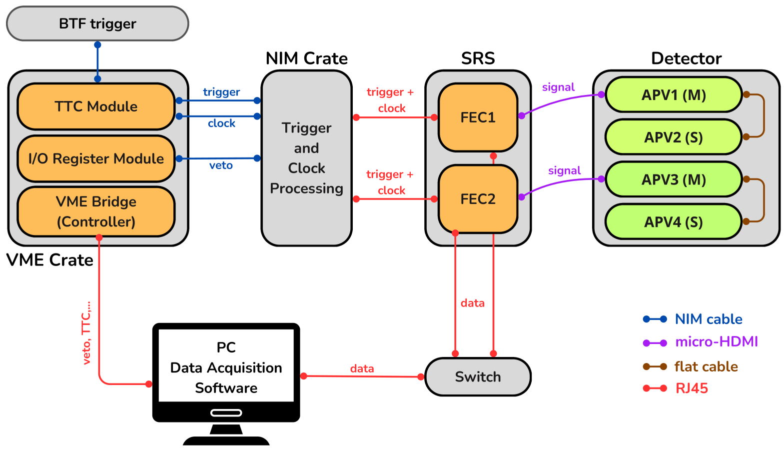


**Figure 4.2.** Schematic picture of the Scalable Readout System.

In our case, the front-end electronics is based on the APV25 chip. This chip comprises 128 readout channels, each incorporating a low noise charge preamplifier with a 50 ns CR-RC shaping circuit and a 192 pipeline of switched capacitor elements, used to store the output of the amplifier, sampled at a 40MHz rate [42]. Each channel is dedicated to a different strip, thus requiring the use of six APVs for the readout of the TMM and eight for the ExMe. APVs are usually used in a *Master-Slave* configuration where the slave is connected to the master with a flat cable, while the master is connected to the SRS using a micro-HDMI cable. This configuration allows reading a higher number of channels with a reduced number of cables. The HDMI cables coming from the front-end are connected to an FPGA-based card called *Front-End Card* (FEC)[43]. The trigger to the system comes from the BTF itself and it is then clocked by a TTC module included in a VME crate. The trigger and clock are then processed by the NIM crate, which delivers in output the trigger and the clock signal to each FEC card separately. The VME crate also contains an I/O register module which deals with the vetoing operation, namely it checks if the acquisition

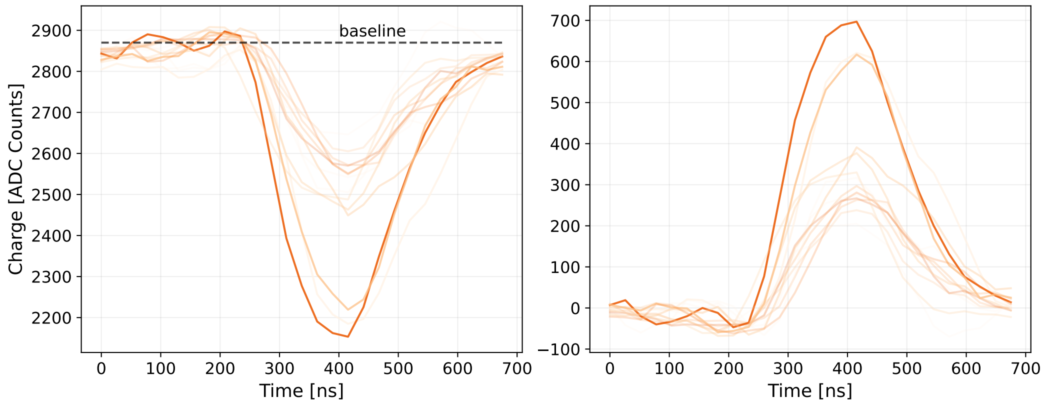


**Figure 4.3.** Some example signals with different amplitudes as sampled by the APV25 chip before (left) and after (right) baseline subtraction performed by the DAQ software.

system has finished to process the previous trigger and is ready to accept a new one. It communicates with the PC, and hence with the acquisition software, through its internal Controller module. The detector data collected from the APV and sent to the FEC, are then processed by a network switch, which eventually sends the data to the PC. The collected data are written to a ROOT file by the mmDAQ data acquisition software. The software allows to load a *Pedestal*[1] file, which contains the average noise and the standard deviation for each strip.

This file is used to perform real-time baseline subtraction and is saved for backup in the output ROOT file. The output file contains: the list of strips which recorded a signal during an event, accompanied by the name of the chamber they belong to and the charge profile in ADC counts (analog-to-digital converter) in the form of a 27 bins histogram, in which every bin corresponds to a 25 ns interval. A collection of sample signals is shown in Figure 4.3 both before and after noise subtraction. A cross-talk correction is also applied directly from the data acquisition software to compensate for induced signal on non-hit strips due to stray capacitances.

## 4.3 Reconstruction software

To analyse the test beam datasets I developed from scratch a reconstruction software based on Python language. The programming language choice guarantees cross-platform support, and allowed to develop the software in a relatively short amount of time. However a well-known Python flaw is its higher execution time, for this reason, the most computationally expensive tasks were accelerated using the *Numba* library, which translates Python functions to optimized machine code at runtime. All the relevant parameters for the chamber description and for analysis

[1]The pedestal is a run performed with the beam-off, in order to evaluate the noise level of the detector.

cuts are included into a YAML (*Yet Another Markup Language*) configuration file, to be easily accessible and modified by the user.

### 4.3.1 Signal Processing

For each strip the quantities of interest are two: the time of the hit and the deposited charge. The time of the hit was extracted by fitting the 27 bins charge profile with a Fermi-Dirac distribution in the range between the start of the event and the highest bin:

$$f_{FD}(t) = A\left(1 + e^{-\frac{(x-t_{half})}{s}}\right)^{-1} + B \tag{4.1}$$

where $A$ and $B$ are two constants representing the maximum height of the distribution and its vertical displacement respectively. $t_{half}$ is the time at half height of the distribution and is taken as the time of the hit on the strip. The parameter $s$ describes the slope of the distribution. This part of the analysis was carried out using a ROOT macro to exploit the higher speed of C++, due to the very large number of fit to be performed. The charge associated with the hit was evaluated as the content of the highest bin in the fitted range. An example of a fitted signal with the described procedure can be seen in Figure 4.4. Only strips with an error on

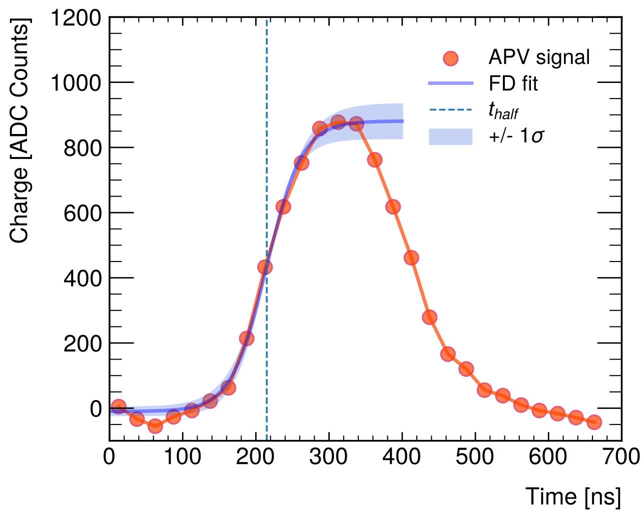


**Figure 4.4.** The signal of one strip and the fitted Fermi-Dirac function. Each marker is the value of one of the 25 ns samples. The blue dashed line indicates the value of $t_{half}$ returned by the fit procedure.

$t_{half}$ smaller than 10 ns are kept for the subsequent analyses. The time and charge distributions of all strips, obtained from run 2124, taken with a drift voltage of 3000 V and an amplification voltage of 490 V, are shown in Figure 4.5. The charge distribution for the ExMe, in orange in Figure 4.5a, has an asymmetric shape with a long tail at high charge values and shows a mean charge value of $468$ ADC counts. The long tail follows from the fact that the collected charge is proportional to the energy loss in the gas, which is described for thin detectors by the Landau distribution (see Equation 3.5). We can also notice the presence of a peak at around $2000$ ADC counts, which is due to saturation effects. Whenever the deposited charge is too high to be converted by the ADC, it is interpreted as the maximum value that the ADC can provide. This causes a sharp edge in the charge distribution at the saturation point. In the figure, no such sharp edge is observed because of baseline subtraction, which has a different value for each strip. Regarding the time distribution of Figure 4.5b, we can clearly see how the reconstructed times for the ExMe are centered in the $0 - 500$ ns region, which is compatible with the value expected by dividing the $5$ cm drift gap size by the drift speed of ArCF$_4$Iso (88:10:2) obtained using a *Garfield++* simulation, which is around $10.5$ cm$/\mu$s.

The time distribution for the ExMe has a characteristic double-peak shaped spectrum, with one bump at around $50$ ns and a second, smaller one, around $450$ ns. This can be due to the finite thickness of the chamber walls through which the beam enters and exits. Such a shape is not observed in the TMM on the other hand, which presents only the peak at the beginning of the spectrum since, as can be seen in Figure 4.1, the front face of the chamber has a thin Mylar window at its entrance, opposite to the face containing the readout plane. Hence the beam interacts more with the face containing the readout plane, made of heavier materials, causing the first peak. Another interesting aspect can be highlighted from the TMM spectra. The distribution for $x$ coordinate clearly has a tail extending to higher times with respect to $y$ coordinate, due to the induced charge effect from the former coordinate, described in section 3.4.

### 4.3.2 Clustering algorithm

The passage of a particle in the chambers generates a signal in more than one strip. This is especially true if the chamber is tilted, as in the case of the ExMe. Each track will therefore produce a signal in several strips, so it is necessary to group strips associated with the same particle into a *Cluster*. Several clustering algorithms exist, but the one implemented in the software we used is based on DBSCAN (*Density-Based Spatial Clustering of Applications with Noise*)[2].

This algorithm identifies clusters as areas with an high density of points to cluster separated by low-density areas. The definition of what is considered high density is determined by two parameters: `min_samples` and `eps`. They key concept at the basis of DBSCAN is the one of *core samples*. A cluster is defined as a set of *core samples*, which is a sample that has at least a number `min_samples` of samples within a distance `eps` from them (see Figure 4.6). If the distance of a sample from every other core sample it's greater than `eps`, the sample is classified

[2] `https://scikit-learn.org/stable/modules/clustering.html#dbscan`

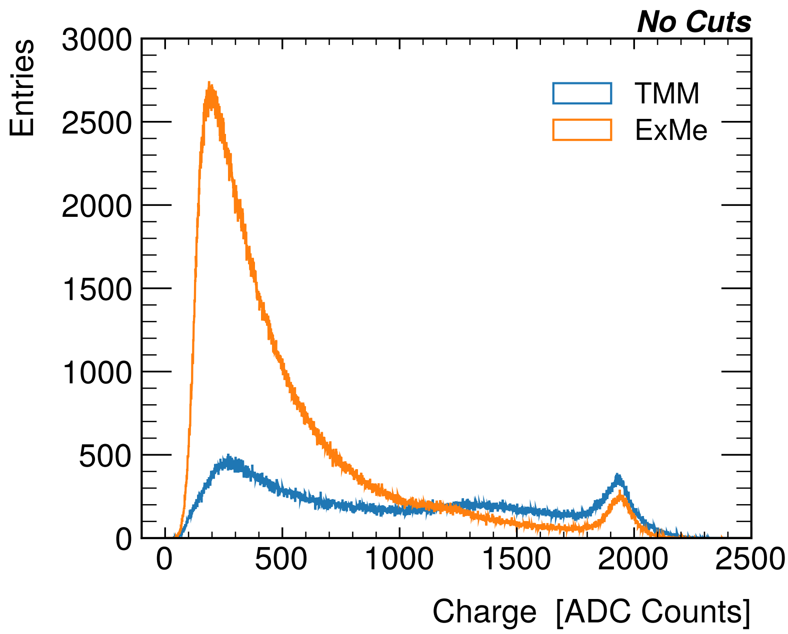


**(a)**

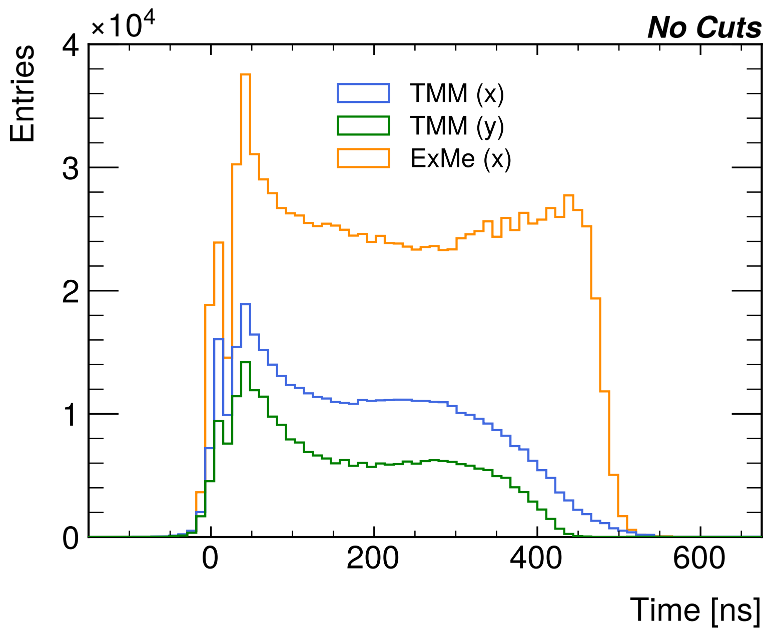


**(b)**

**Figure 4.5.** (a) The charge distributions for the TMM and ExMe $x$ coordinate. The peak around 2000 ADC counts is due to saturation. (b) The distribution of strip hit times for both coordinates of the TMM chamber and the $x$ coordinate of the ExMe chamber.

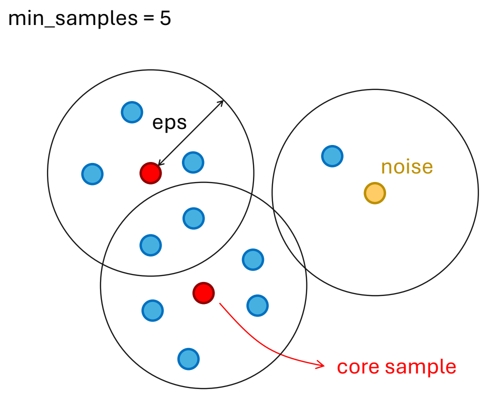


**Figure 4.6.** A schematic drawing of the working principle of the DBSCAN clustering algorithm.

as noise and not included in any cluster. In our case a sample is a strip producing a signal.

For the present analysis we required `min_samples` $= 1$ and `eps` $= 1$, which translates in the requirement of a maximum of one consecutive hole in a cluster. Whenever two or more consecutive strips did not generate any signal, the clusterization is interrupted. The minimum number of samples primarily controls the algorithm's tolerance to noise. Setting this value to 1 does not fully exploit the ability of the DBSCAN algorithm to use the information on the density of active strips, which could prove beneficial in the rejection of spurious strips. Consequently, an in-depth study of the algorithm's response to different parameter values could prove highly insightful. The clusters are then kept or discarded depending on user-defined cuts on the minimum number of strips per cluster and the minimum charge of the cluster.

### 4.3.3 Charge centroid and $\mu$TPC techniques

Once the strips have been grouped into clusters, two different methodologies are employed to assign a position to each cluster: the charge centroid method and the $\mu$TPC method. A schematic drawing of the techniques is shown in Figure 4.7 The first one assigns a coordinate to the reconstructed cluster by weighting the position of the strips by their charge through the relation:

$$x_C = \frac{\sum_i q_i \cdot x_i}{\sum_i q_i} \tag{4.2}$$

As one can easily guess, this technique is particularly effective for almost perpendicular tracks, while its goodness degrades as the inclination of the track increases. For tracks with a significant inclination, the $\mu$TPC algorithm is more appropriate. In addition to the information on the transverse coordinates coming from the strip

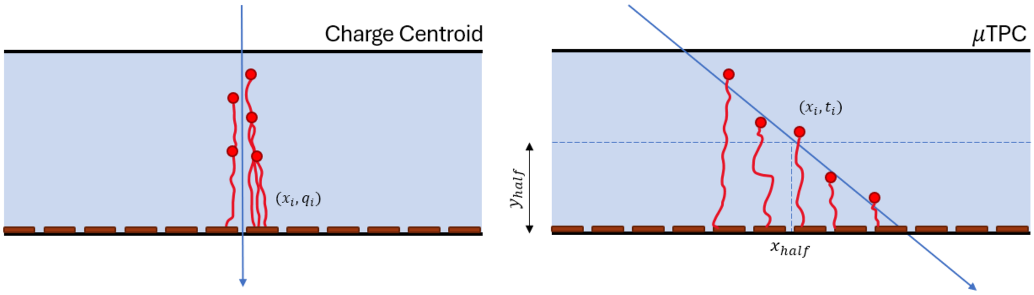


**Figure 4.7.** Schematic drawings of the charge centroid (on the left) and $\mu$TPC methods (on the right).

position, the time of the hit is also used to reconstruct the $z$ coordinate using the known drift velocity:

$$z_i = v_{drift} \cdot t_i \tag{4.3}$$

A linear fit is then performed to extract the track angle, together with a parameter called $x_{half}$, representing the $x$ position at the tracklet half-height $y_{half}$:

$$x_{half} = \frac{y_{half} - q}{m} \tag{4.4}$$

where $m$ and $q$ are the slope and intercept of the linear fit. For the TMM chamber clusters we used the charge centroid method, while the $\mu$TPC technique was used on the ExMe.

## 4.4 Efficiency Measurement

A fundamental study of the performance of any detector is to quantify its detection efficiency. In other words, we are interested in measuring how many times, in the presence of a crossing particle, the detector correctly identifies its passage. This process is inherently binomial, as there are only two possible outcomes: detection or non-detection. If we define the fraction $n$ of correctly identified events and the total number of events $N$, the efficiency has the following expression:

$$\epsilon = \frac{n}{N} \tag{4.5}$$

the probability distribution of this random variable will be [44]:

$$\mathcal{P}(\epsilon, N) = \binom{n}{n\epsilon} p^{n\epsilon}(1-p)^{n(1-\epsilon)} \tag{4.6}$$

whose expected value and standard deviation are:

$$E[\epsilon] = p \qquad\qquad \sigma[\epsilon] = \sqrt{\frac{p(1-p)}{N}} \tag{4.7}$$

The parameter $p$ represents the efficiency, and for a single efficiency measurement its best estimator is given by $\epsilon$ in Equation 4.5.

### 4.4.1 Cluster Efficiency

Cluster efficiency is an overall detector performance metric, defined as the ratio between the number of events correctly identified by the ExMe and the number of events recorded by the TMM :

$$\epsilon = \frac{N_{ExMe}}{N_{TMM}} \tag{4.8}$$

To compute the efficiency of the ExMe chamber the algorithm implemented in the reconstruction software is the following:

1. Select only events with one cluster in the TMM $x$ coordinate.
2. If the charge centroid of the TMM cluster lies in the part of the chamber illuminated by the beam, $N_{TMM}$ is incremented by one unit. In particular, for every run a $3\sigma$ range around the average position of the charge centroid computed on the entire run was used.
3. Search for a cluster in the ExMe chamber such that its charge centroid lies in a window of $\pm 25$ mm around the TMM cluster centroid position.
4. Fit the cluster using the $\mu$TPC method and, if the p-value of the fit is higher than $5\%$, increment $N_{ExMe}$ by one unit.
5. After all events have been processed the efficiency and its uncertainty are computed using Equation 4.5 and Equation 4.7

To better demonstrate how an event looks like, Figure 4.8 shows the output of the software event display. The size of the marker is directly proportional to the

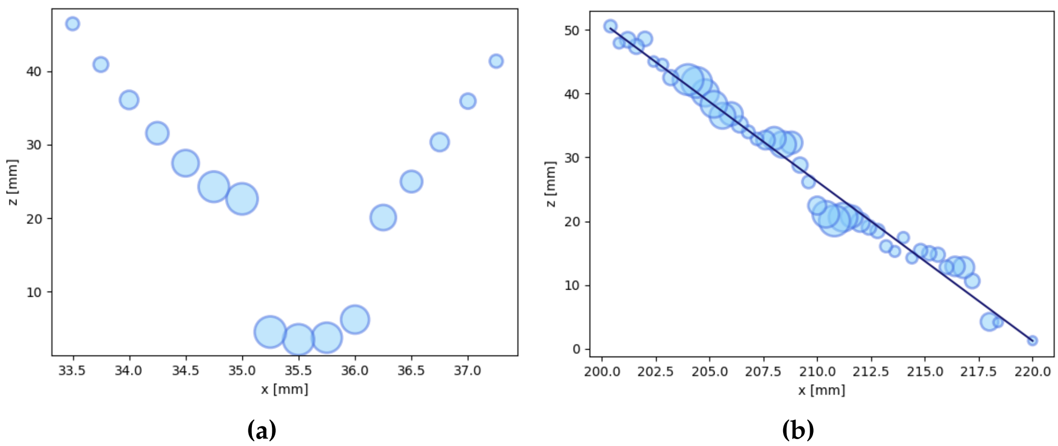


**Figure 4.8.** (Left) A cluster on the TMM $x$ coordinate readout plane. The characteristic "V"-shape due to charge induction is clearly visible (Right) A cluster on the ExMe chamber with its linear fit superimposed. The marker size is proportional to the charge deposited on each strip.

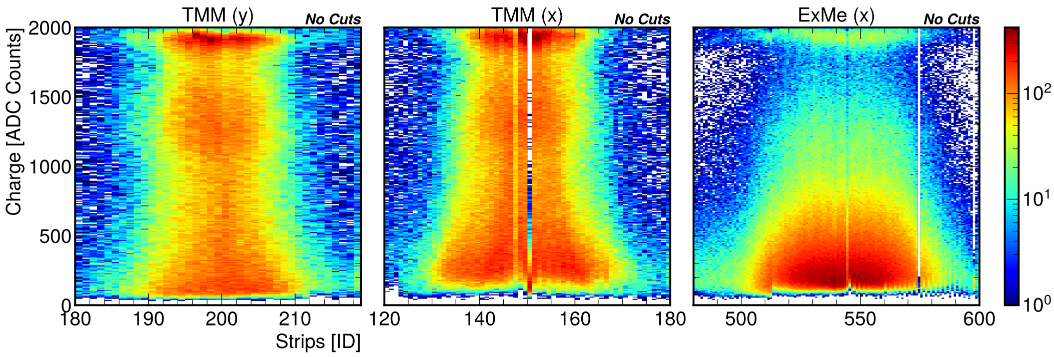


**Figure 4.9.** 2D histogram of charge vs strip ID for both TMM views and for the ExMe. The jagged profile in the low charge region of the ExMe histogram after strip number 550 is evident, indicating the presence of faulty strips.

charge deposited on each strip. On the left, a TMM cluster that passed the selection cuts can be seen (Figure 4.8a). The "V" shape of the cluster is a direct consequence of the capacitive coupling between the $x$ and $y$ readout layers, an effect we have mentioned several times before but is clearly visible here. As time passes, the signal traveling on the strips of the first layer induces a signal on increasingly distant strips in the underlying layer. By fitting the two halves of the V-shaped TMM signal, a charge spreading velocity of around $4.7 \times 10^{-3}$ mm/ns is found, corresponding to $4.5\%$ of the drift velocity. On the right, the inclined ExMe track associated with the one in the TMM is shown with a superimposed linear fit (Figure 4.8b).

Not all ExMe clusters were as definite and clear as the one in Figure 4.8. In fact, after the test beam was finished, it was realized that the beam was centered on a malfunctioning APV chip. As can be seen in Figure 4.9 the region between strips 550-600 shows a jagged profile, indicating that some strips demonstrate a difference in responsiveness to charge compared to others.

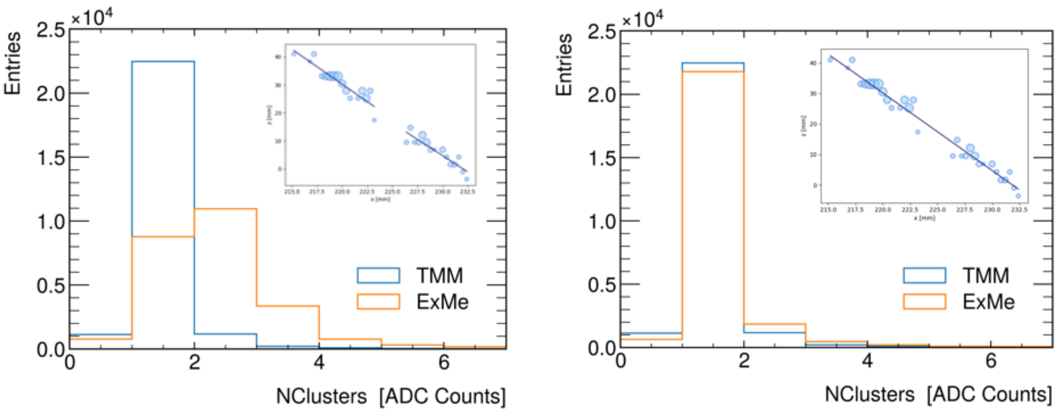


**Figure 4.10.** The distribution of the number of clusters per event for the TMM $x$ coordinate and for the ExMe. On the right a higher number of consecutive inactive strips is allowed to cope with the faulty strips. An example of the effect of this procedure on the track reconstruction is shown as an inset in the plots.

For this reason many ExMe tracks showed a lower number of active strips than expected. As a consequence many clusters belonging to the same track were reconstructed and fitted separately. To cope with this effect it was sufficient to allow a larger number of consecutive holes in ExMe clusters in such a way to bring the average of the distribution of the number of cluster per event around 1 (see Figure 4.10). The algorithm for the computation of cluster efficiency was applied to all the runs of the *High Voltage Scan* to study its dependence on the amplification voltage. The higher the gain, the higher is the charge amplification, resulting in a higher efficiency with a typical sigmoid-shaped "activation function". The results obtained are reported in Figure 4.11 and show a good agreement with the expected trend, with the efficiency reaching a plateau for values of the high voltage $> 490$ V. The highest value was obtained for $V_{amp} = 500$ V:

$$\epsilon_{500} = 0.9416 \pm 0.0015 \tag{4.9}$$

To check how the faulty APV affected the results, the cluster efficiency was also computed for run 2019 ($V_{drift} = 3000$ V, $V_{amp} = 490$ V) of November 2023 test beam, where the beam was centered on a working chip.

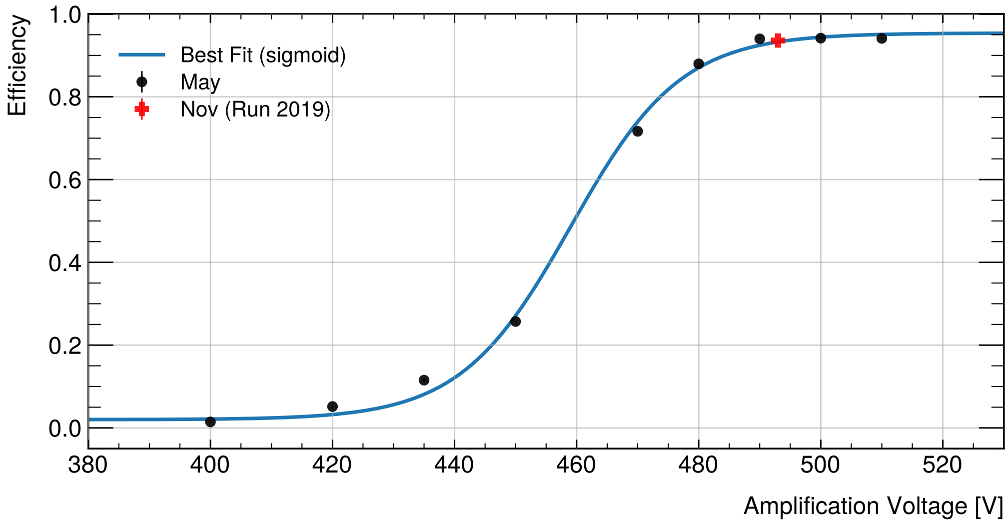


**Figure 4.11.** Cluster efficiency as a function of increasing ExMe amplification voltage. The experimental points have been fitted with a sigmoid activation function. Error bars are present but are too small to be appreciated. The cluster efficiency for run 2019 of November test beam is indicated with a red marker.

### 4.4.2 Hit Efficiency

While cluster efficiency depends on the cluster definition, hit efficiency refers to individual strips, and therefore to the bare detector performance. It represents the percentage of events in which a strip that should have produced a signal did, in fact, do so. For each event in which an inclined track is successfully identified and reconstructed in the ExMe, a linear fit is repeatedly performed on the same cluster, each time excluding a different strip between its first and last strip. If the fitted line passes through the excluded strip, we check whether it produced a signal or not. Then, to find the average hit efficiency of a run, a fit with an horizontal line was performed between strip number 490 and 510 to avoid strips belonging to the faulty APV while still staying near the beam center to collect enough statistics, as shown in Figure 4.12.

Using hit efficiency instead of cluster efficiency allows to get rid of the bad APV, since no clustering is needed.

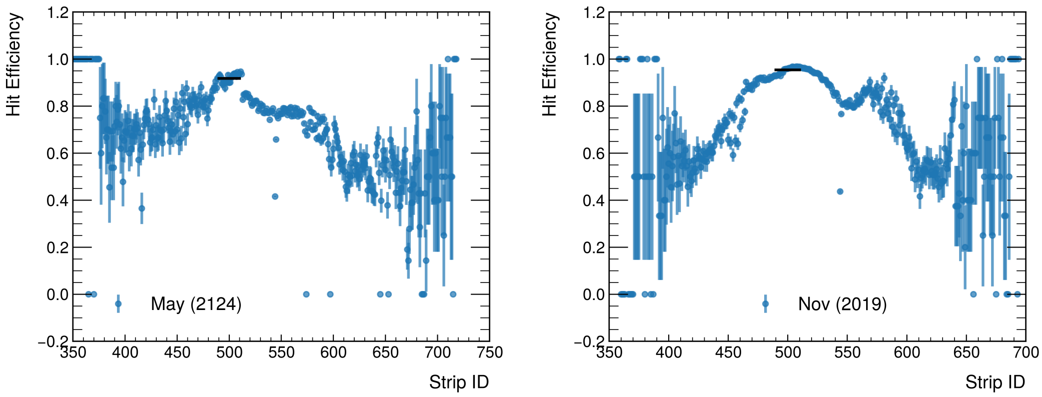


**(a)** **(b)**

**Figure 4.12.** Hit efficiency for run 2124 of May test beam (a) and for run 2019 of November test beam (b). The straight horizontal line fit between strip number 490 and 510 is shown as a black solid line.

This procedure was performed on every run of the *High Voltage Scan* to cross-check the results on cluster efficiency. The obtained results are reported in Figure 4.13; for run 2019 of November 2023 test beam the hit efficiency at $V_{amp} = 490$ V was found to be:

$$\epsilon_{Nov}^{hit} = 0.955 \pm 0.003 \tag{4.10}$$

During May 2024 test beam, at the same amplification voltage value, we obtained instead:

$$\epsilon_{May}^{hit} = 0.918 \pm 0.004 \tag{4.11}$$

This value is roughly $4\%$ lower than the hit efficiency measured at the same voltage for November test beam. This is both due to the overall lower performances of the detector due to the beam centered on the faulty APV and to the lower statistics. The maximum value of the hit efficiency measured during May 2024 test beam was found at $V_{amp} = 510$ V and it is:

$$\epsilon^{hit} = 0.956 \pm 0.002 \tag{4.12}$$

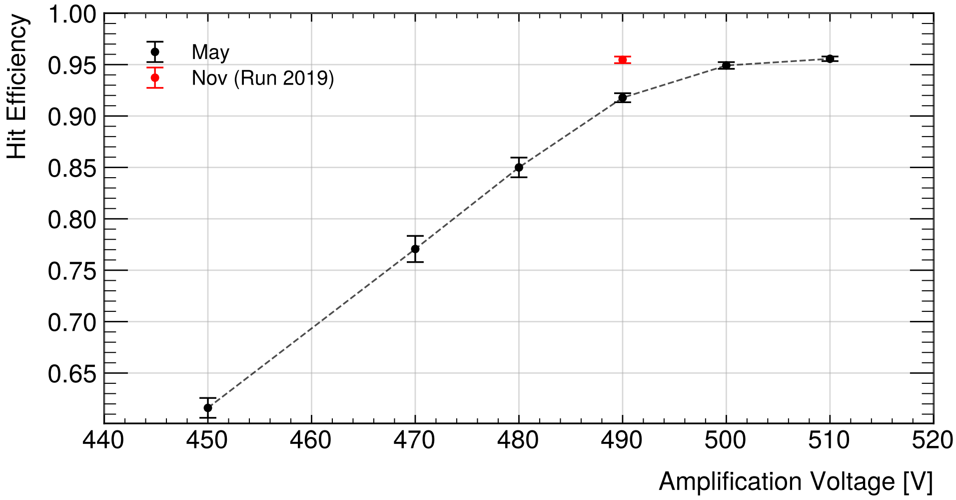


**Figure 4.13.** Hit efficiency as a function of amplification voltage. The value for run 2019 of November test beam is also shown with a red marker.

## 4.5 Drift Velocity measurement

As we already mentioned in subsection 3.1.2, drift velocity is defined as the macroscopic average velocity at which electrons and ions produced by ionization by a particle crossing the detector travel in the gas under the influence of the electric field. A common way to compute drift velocity is by fitting the strip times distribution with a double Fermi-Dirac distribution:

$$f_{2FD}(t) = A\left(1+e^{-(x-t_1)/s_1}\right)^{-1}\cdot\left(1+e^{(x-t_2)/s_2}\right)^{-1}+B \tag{4.13}$$

This approach minimizes the sensibility to the spikes of the time distribution. The drift velocity is then defined as:

$$v_{drift} = \frac{d}{t_2 - t_1} \tag{4.14}$$

where $d$ is the drift gap size, the sum of the thicknesses of the amplification region ($0.128$ mm) and the drift region ($50$ mm). The associated uncertainty is given by:

$$\sigma_v = v\sqrt{\left(\frac{\sigma_d}{d}\right)^2+\left(\frac{\sigma_{\Delta t}}{\Delta t}\right)^2} \qquad \sigma_{\Delta t} = \sqrt{\sigma_{t_1}^2+\sigma_{t_2}^2} \tag{4.15}$$

The uncertainty on $t_1$ and $t_2$ was obtained from the fit parameters, while the error on the drift gap size ($\sigma_d$) was taken to be equal to $1$ mm. Such a conservative choice was dictated by the lack of accurate measurements of the ExMe chamber thickness. In Figure 4.14 an example of the result of this procedure for run 2124 of May test beam is shown. Once the drift velocity for all runs in the *Drift Voltage*

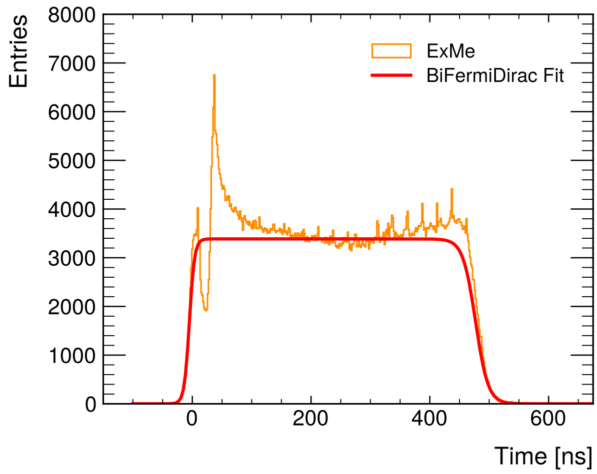


**Figure 4.14.** A double Fermi-Dirac fit of the strip time distribution for run 2124 of May test beam.

*Scan* has been computed, it was compared with the simulated values obtained from *Garfield++*. From Figure 4.15, a good agreement between data and simulation is found, with a maximum deviation of around $5\%$. All the points seem to be slightly

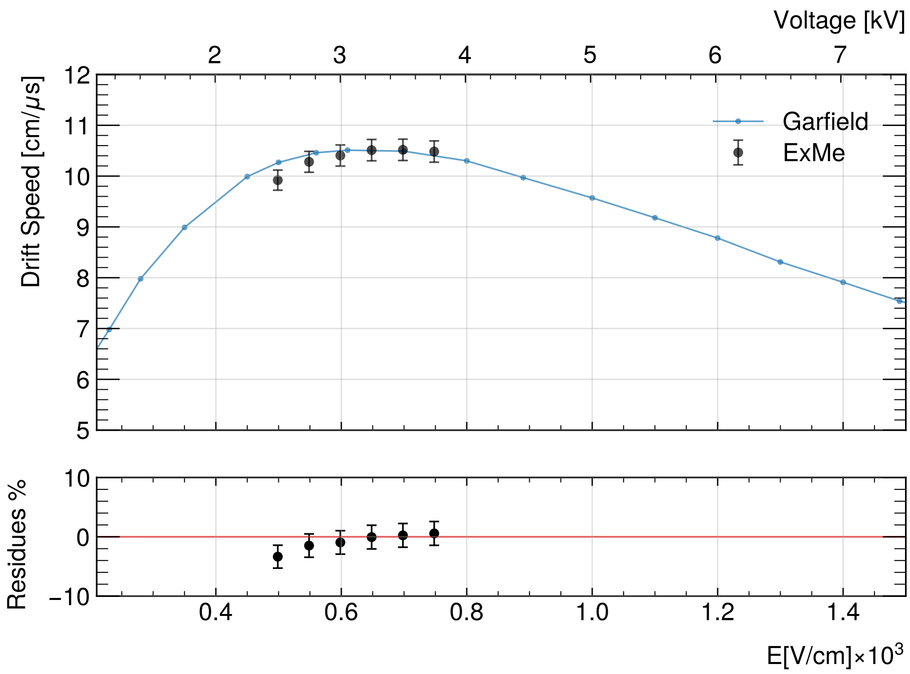


**Figure 4.15.** Comparison of the experimentally measured drift speeds, shown with black markers, and the values predicted by a Garfield++ simulation, shown with a solid line. The bottom panel shows the percentage deviation between data and prediction.

shifted to the right with respect to the simulated values. This could be due to the imperfect knowledge of the drift gap size, which is needed to compute the value of the electric field from the value of the voltage. The value of the drift gap thickness that maximizes the agreement between data points and the simulated values is roughly $50.608$ mm, that is inside the $1\sigma_d$ interval around the nominal gap size ($50.128$ mm).

## 4.6 Drift coordinate resolution

The resolution in the $z$ coordinate, namely the one parallel to the electric field direction, is related to the time resolution of the detector. For PADME purposes a $z$ resolution at least as low as $1$ mm is required to have sufficiently good precision in reconstructing the particle trajectory. To study this property, a subset of the events with a p-value higher than $0.9$ was used, in order to only analyze events with well definite tracks in the ExMe chamber. The distribution of residuals between the measured $z$ coordinate and the value coming from the fit is shown in Figure 4.16. A

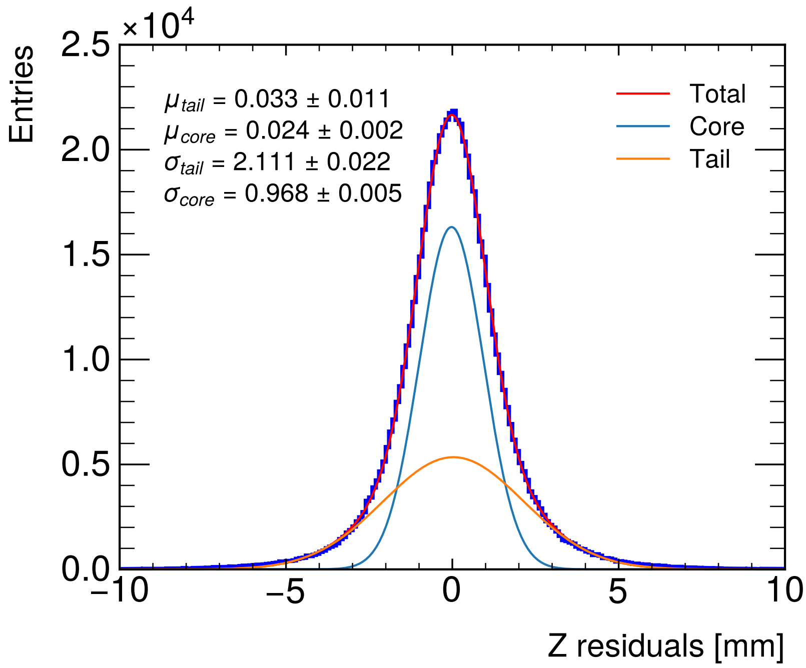


**Figure 4.16.** Distribution of residuals between $z$ coordinate obtained from the strip hit and the $z$ coordinate extrapolated from the linear fit. The fit is done using a double Gaussian function to account for the presence of long tails.

double Gaussian fit is superimposed to account for the presence of long tails, which are connected to the charge dependence of the residuals distribution. We obtained the following results:

$$\mu_{core} = 0.024 \pm 0.002 \text{ mm} \quad (4.16)$$

$$\sigma^z_{core} = 0.968 \pm 0.005 \text{ mm} \quad (4.17)$$

$$\mu_{tail} = 0.033 \pm 0.011 \text{ mm} \quad (4.18)$$

$$\sigma^z_{tail} = 2.111 \pm 0.022 \text{ mm} \quad (4.19)$$

The $z$ resolution was taken to be equal to the RMS of the core gaussian. Figure 4.17a shows the 2D histogram of strip charges against $z$ residuals. It can be noticed that the spread in the residual diminishes as the deposited charge increases. In fact, it is straightforward to understand why this happens: signals characterized by a high charge deposition can be better reconstructed and therefore allow a more precise evaluation of the time of the hit. For this reason the study of the $z$ resolution was also carried out as a function of charge. The two-dimensional plot was sliced in 50 horizontal bands, and for each of them a double gaussian fit was performed, like the one reported in Figure 4.17b.

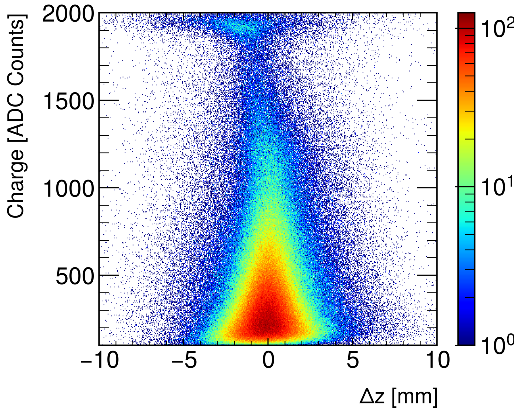


**(a)**

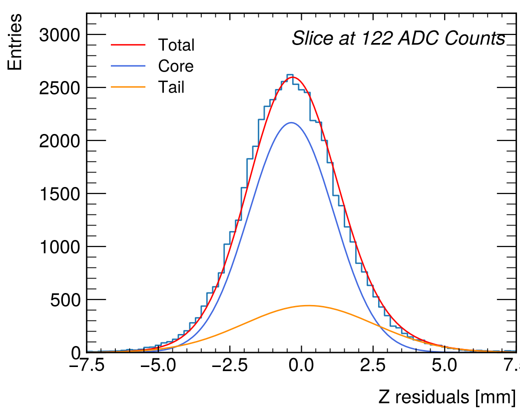


**(b)**

**Figure 4.17.** (a) 2D histogram of strip charge versus $z$ residuals (b) Illustrative double gaussian fit for the slice at 122 ADC counts.

The RMS values of the core gaussians for all slices have then been fitted with an empirical function (see Figure 4.18a). In particular, we are interested in evaluating the $z$ resolution at the average charge value, which is 468 ADC counts (see Figure 4.5a):

$$\sigma_z = 0.882 \pm 0.003 \text{ mm} \quad \text{at 468 ADC counts} \quad (4.20)$$

corresponding to a time resolution of :

$$\sigma_t = 8.474 \pm 0.025 \pm 0.169 \text{ ns} \quad \text{at 468 ADC counts} \quad (4.21)$$

where the first contribution to the uncertainty is due to the error on the fit parameters, while the second comes from the uncertainty on the drift velocity taken from

Figure 4.15. The agreement between the fitted function and data points is good up to 800 ADC counts. After this point the fit worsen due to the lower statistics in the high charge region. Long tails observed in the integrated $z$ residuals distribution, do not only depend on the widening of the resolution at small charges, but also on the charge dependence of the mean of the residuals. This can be appreciated both from the argued shape of the charge versus $\Delta z$ 2D histogram of Figure 4.17a and from Figure 4.18b that shows the mean value of core and tail fitted gaussians for different charges. The mean of the core distribution is stable around zero in the average charge region, and then starts to drift towards positive values. On the other hand the tail gaussian has a non-zero mean centered around 0.3 mm.

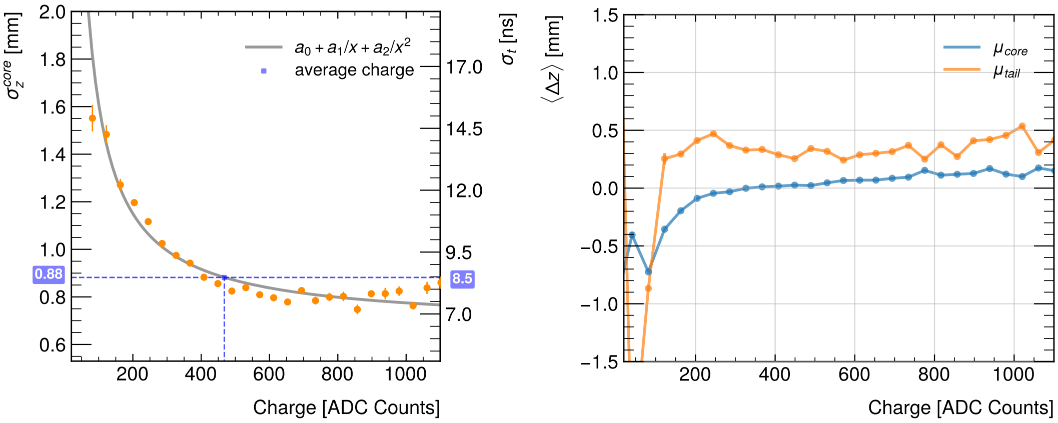


**(a)** **(b)**

**Figure 4.18.** (a) RMS of the core gaussian as a function of the charge. (b) Mean of core and tail gaussians as a function of charge.

The resolution on strip time, and therefore the one on the $z$ coordinate does not only depend on the charge. The path of the drifting ions towards the readout plane is not a straight line but it is affected by the random collisions happening against the gas molecules. This spreads the arrival time of the drifting electron, a phenomenon known as *longitudinal diffusion*. The greater the distance a drifting electron has to travel, the more collisions it will encounter, resulting in increased diffusion. To see how much this effect contributes to the time resolution of the Micromegas, the $z$ position reconstructed from the drift time was plotted against its residual with respect to the linear fit to the track. Figure 4.19a shows the 2D histogram of these two quantities. The histogram has then been sliced into 50 horizontal bands, each fitted using a double gaussian. The RMS of the core distribution for each slice as a function of $z$ is shown in Figure 4.19b.

No dependence of the $z$ resolution on the $z$ coordinate is observed as confirmed by the result of a linear fit to data:

$$a_0 = -1.0 \pm 1.5 \times 10^{-4} \tag{4.22}$$

$$a_1 = 0.903 \pm 0.004 \text{ mm} \tag{4.23}$$

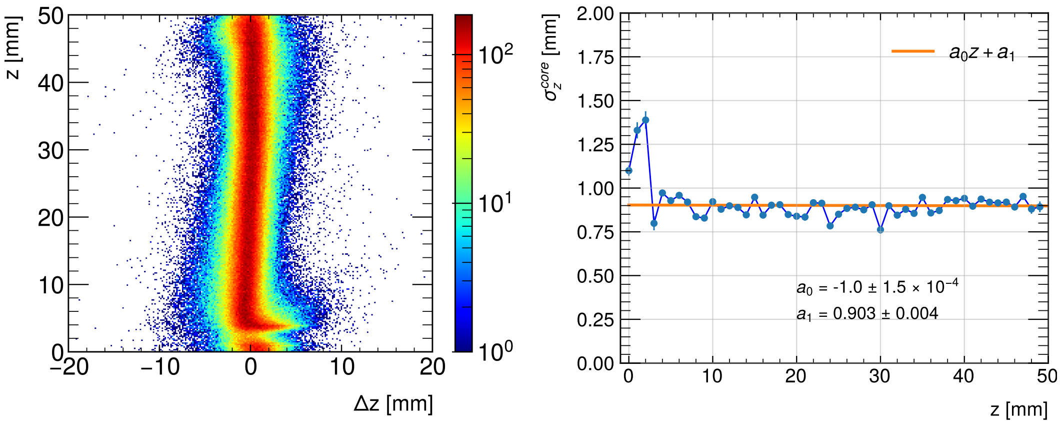


**Figure 4.19.** (a) 2D histogram of $z$ coordinate versus $z$ residuals (b) RMS of the core gaussian as a function of the charge.

in fact, the slope $a_0$ is compatible with zero between one standard deviation. This confirms that in our detector the effect of longitudinal diffusion on time resolution is negligible.

## 4.7 Spatial resolution

As we mentioned in subsection 4.3.3, the centroid method is better suited for determining the center of a cluster in the case of almost perpendicular tracks. Figure 4.20 shows the distributions of the charge centroid for both TMM coordinates and for ExMe $x$ coordinate. A Gaussian function was used for fitting, yielding the following estimate for the spatial resolution:

$$\sigma_y^{TMM} = 1.16 \pm 0.01 \text{ mm} \qquad \text{(centroid)} \tag{4.24}$$
$$\sigma_x^{TMM} = 1.73 \pm 0.02 \text{ mm} \qquad \text{(centroid)} \tag{4.25}$$
$$\sigma_x^{ExMe} = 4.68 \pm 0.05 \text{ mm} \qquad \text{(centroid)} \tag{4.26}$$

The resolution of the ExMe can be seen to be worse by more than a factor 2 with respect to TMM. This is due to the fact that the ExMe chamber is tilted, so that a crossing particle produces clusters consisting of a large number of strips, which therefore have a higher spatial extension. To evaluate the spatial resolution for inclined tracks we will use a different method based on the previously defined quantity $x_{half}$. In this case we will use data from a run of the November 2023 test beam, where the two chambers were tilted by the same angle. The $\mu$TPC method is applied to both chambers and $x_{half}$ is computed. The distribution of $x_{half}$ for the two chambers is shown in Figure 4.21. The fit is performed using a double Gauss

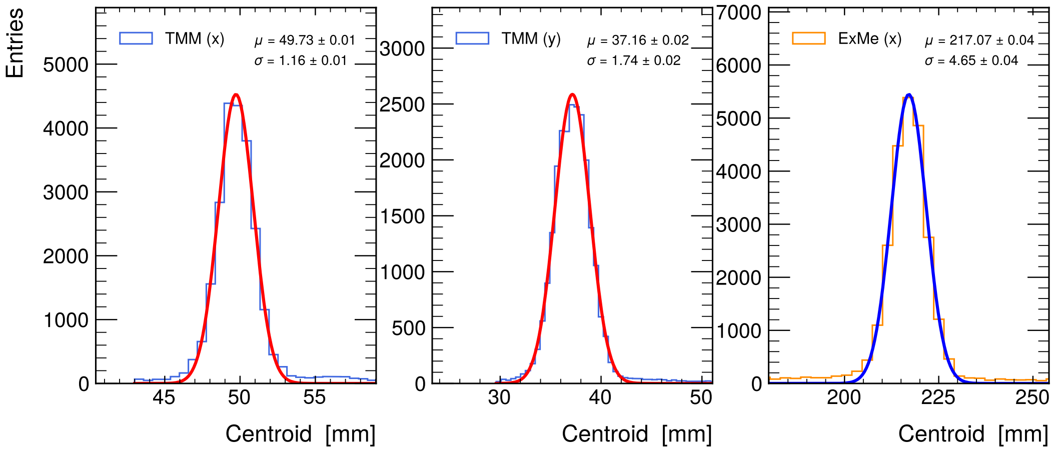


**Figure 4.20.** Centroid distributions for the $y$ coordinate of TMM (left), $x$ coordinate of TMM chamber (center) and $x$ coordinate of ExMe (right).

function to disentangle the contribution of the beam spread to the resolution, which is evaluated as the RMS of the core distribution.
We obtain the following results:

$$\sigma_x^{TMM} = 2.30 \pm 0.17 \text{ mm} \qquad (\mu\text{TPC}) \tag{4.27}$$
$$\sigma_x^{ExMe} = 2.74 \pm 0.71 \text{ mm} \qquad (\mu\text{TPC}) \tag{4.28}$$

As expected the spatial resolution for non-perpendicular tracks can be better estimated with the use of the $\mu$TPC method. The performance of the detector can

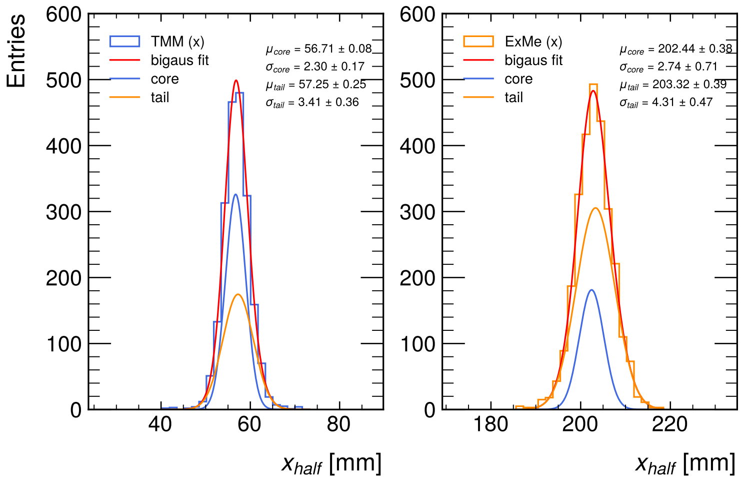


**Figure 4.21.** Distribution of $x_{half}$ for the $x$ coordinate of TMM (left) and ExMe (right). The double gaussian fit is shown in red, together with the separate contribution of core and tail distributions.

also be expressed in terms of angular resolution. The precision in reconstructing angles is of particular importance for PADME, because some of the analysis cuts used to isolate the X17 signal are based on the direction of the final state particles, to match the kinematics of a two body process (see Figure 2.10a). The estimate of angular resolution was performed on a subset of data, where additional cuts had been imposed to discard all spurious and badly reconstructed events. In particular, a tighter cut on the minimum number of strips per cluster was used to discard small groups of strips that mimicked the passage of a particle in the detector. The requirement for the p-value of the linear fit on the cluster was also tightened (> 0.90) for the same reason. A cut on strip hit time was also introduced, keeping only strip whose time lies in the interval $100 - 400$ ns, to exclude from the linear fit the ionizations happening near the chamber walls. These edge points seemed to cause a shift of the reconstructed angle towards larger values, resulting in an asymmetry of the angular distribution which is still visible in Figure 4.22. The need to exclude points near the chamber's edge from the fit comes from the presence of border effects due to the readout planes of the chamber. This effects can be appreciated in Figure 4.19a for example, where a systematic shift in the mean value of $\delta z$ residuals at small $z$ is present. A similar effect is also present at $z \simeq 50$ mm, but in the opposite direction, giving to the distribution a slightly "S"-shaped appearance. This means that for charge deposits with $z < 10$ we reconstruct a value of $z$ higher than the correct one, and for this reason we will measure an angle slightly larger than the real one.

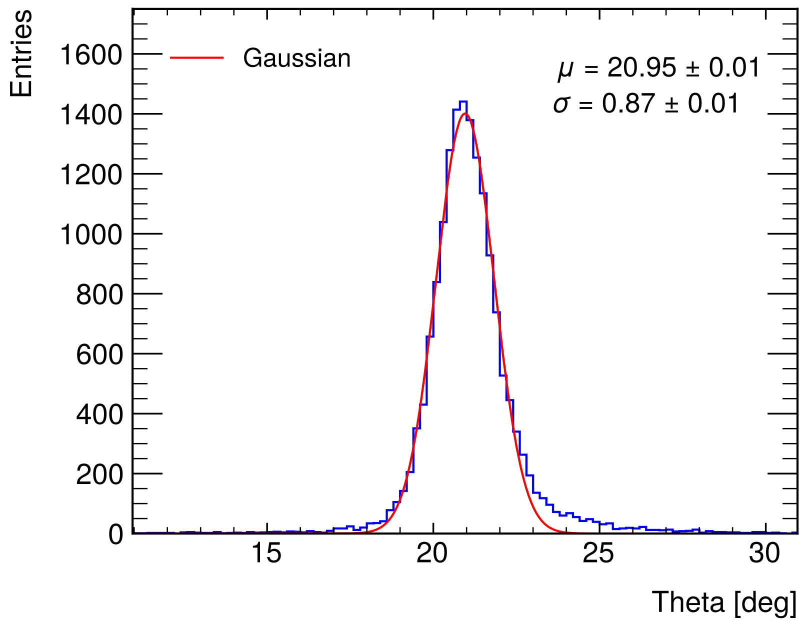


**Figure 4.22.** Angular distribution of the angle $\theta$ between the ExMe chamber and the electron beam. A asymmetry towards larger values can be seen, which was mitigated by fitting only the charge deposits in the region 10 mm < $z$ < 40 mm of the ExMe chamber.

The results obtained by fitting the reconstructed angle distribution with a Gaussian function are:

$$\mu = 20.95^\circ \pm 0.01^\circ \tag{4.29}$$

$$\sigma_\theta = 0.87^\circ \pm 0.01^\circ \tag{4.30}$$

$$= 15.2 \pm 0.2 \text{ mrad} \tag{4.31}$$

The resolution has been taken to be the RMS of the fitted function. However, the value presented here should be taken as an overestimate of the true angular resolution of the detector. In fact, it is affected by both the multiple Coulomb scattering that occurs in the reference chamber before the particles reach the ExMe and the original BTF beam spread.

## 4.8 Double-peak separation

As we said, the test beam was conducted using a low-multiplicity beam, significantly reducing the probability of having two tracks hitting the same strip during the same event. This condition is crucial for justifying our procedure for reconstructing strip time, as we disregarded the possibility of having multiple peaks in the strip signal. However, under actual PADME operating conditions, this scenario could occur. Therefore, we need to determine the minimum distance between the two peaks that can be reasonably resolved. To do this we isolated a sample of strip signals from run 2124 of May test beam ($V_{drift} = 3000$ V, $V_{amp} = 490$ V) that had one and only one peak. Peak finding was performed using the `scipy.signal` Python library. Signals in this sample were then randomly added in pairs, introducing an artificial time separation between the two peaks. An example of summed waveform is shown in Figure 4.23a. The separating power was quantified by introducing the quantity $r = h/H$, which represents the ratio between the minimum height between the two peaks $h$ and the height of the smallest of the two peaks $H$. Values of $r$ near $0$ mean that the two peaks can be easily distinguishable. As $r$ approaches $1$, $h$ becomes almost equal to $H$, preventing the separation of the two peaks. Since we reconstructed strip times using the time at half height of the Fermi-Dirac signal, we chose $r = 0.5$ as the maximum acceptable value of $r$ allowing the reconstruction of the two peaks. Figure 4.23b shows the 2D histogram of the values of $r$ against the true time separation between the two peaks. For small values of $\Delta t$, less than $200$ ns, $r$ is close to $1$, so the two peaks are too near to each other, and their width does not allow to separately measure the time of the two signals.

In the figure the bin we highlighted the bin at $\Delta t = 325$ ns , which is the minimum time separation between the two peaks that allows at least $95\%$ of the signals to have a value of $r < 0.5$ (indicated with a white marker), thus enabling effective reconstruction of the two peaks.

The double-peak separation power primarily depends on the width of the strip signals, which is controlled by the rise time $\tau$ of the APV25 RC-CR shaper, around

50 ns. A back-of-the-envelope calculation suggests that, taking as rise time for the signal roughly $3\tau$, in order to resolve the two peaks they should be shifted by around:

$$\Delta t_{min} = 2 \times 3\tau \simeq 300ns \tag{4.32}$$

which agrees with the value we obtained through the previous, more detailed, analysis.

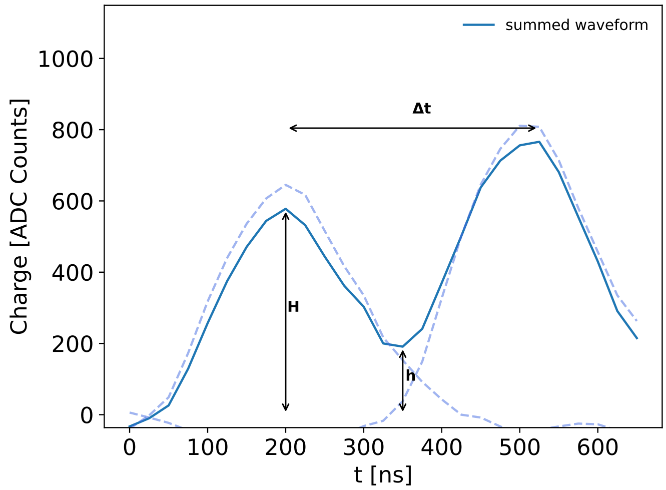


**(a)**

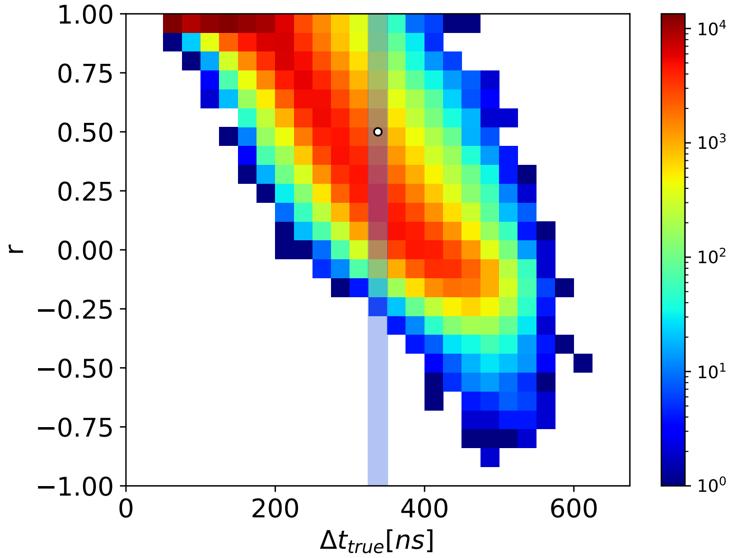


**(b)**

**Figure 4.23.** (a) Two signals contained in the single peak sample added together introducing an artificial time delay $\Delta t$ between the two peaks. (b) 2D histogram of $r$ values against the true time difference introduced between single peak signals.

# Chapter 5

# GEANT4 Simulation

The following chapter is dedicated to the description of the simulation of the PADME Micromegas tracker, which I developed using the GEANT4 package. During the early stages of the detector design process, some projectual decisions needed to be based on the properties of the PADME experimental setup. For example, different amplification voltages were needed in different regions of the readout planes. For example, the central region is affected by a higher flux of particles, primarily coming from the non-interacting portion of the beam, and therefore requires a lower gain to avoid saturating the detector response. On the contrary, the outer region needs to be sensitive to single particles in order to identify potential good $e^+e^-$ final states.

The chapter is organized as follows: section 5.1 and section 5.2 provide some generalities on GEANT4 and on the structure of PADME MonteCarlo simulation framework. section 5.3 describes the development of the simulation of PADME Micromegas tracker while section 5.5 presents the results of the studies conducted with the use of this simulation.

## 5.1 The GEANT4 simulation package

The GEANT4 package is a toolkit for the simulation of radiation interaction with matter, first introduced in 1998 and written in C++[1]. The package can provide the generation of primary particles of any species and also supports the definition of custom particles to study physics beyond the Standard Model. Programs built using GEANT4 can also accurately model detector geometries and their constituent materials, providing the tracking of primary particles inside of them. A complete list of physics processes is also included, for strong, weak and electromagnetic interactions, starting from the milli-electronvolt scale, up to the level of hundreds of TeV. Physical quantities of interest can be recorded both for source and secondaries particles.

[1] https://geant4.web.cern.ch/

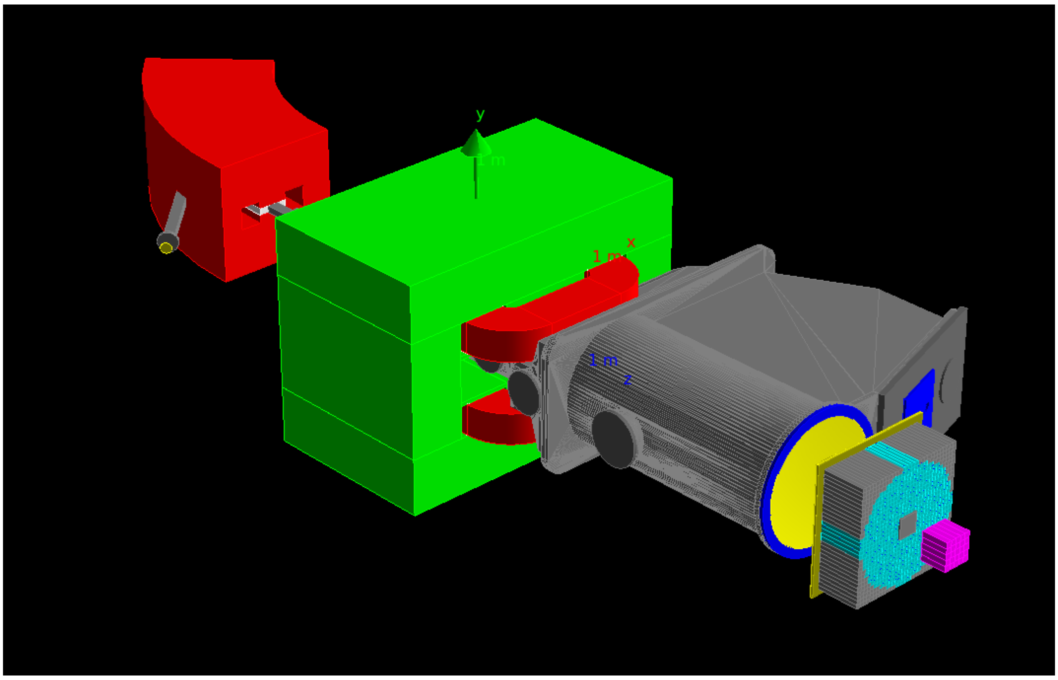


**Figure 5.1.** The PADME GEANT4 simulation. All the various subdetectors can be seen from this view. The SAC is shown in purple and the ECal crystal in cyan. The ETag is represented in yellow, together with the TimePix array in blue, partially hidden. The last part of the beam line is also visible, as the red dipole magnet on the upper left of the figure.

## 5.2 PADMEMC : The PADME MonteCarlo Framework

Since the early stages of PADME, a complete GEANT4 simulation of the experimental setup has been developed and maintained in order to closely follow the evolution of the real experiment [45]. The current version of the software is publicly available as a GitHub repository at PadmeMC. The interaction of the beam inside the active target and the subsequent event kinematics are based on the use of the *QGSP_BERT* physics list, included inside the GEANT4 package. It contains the majority of low-energy electromagnetic processes, such as multiple Coulomb scattering, ionization, Bremsstrahlung emission, two photon annihilation, synchrotron radiation emission, and optionally optical photons tracking. The simulation of specific reactions, like $e^+e^- \to \gamma A'$ and three-gamma events $e^+e^- \to \gamma\gamma(\gamma)$ are performed outside GEANT4, using the *CalcHep* software, dedicated to the evaluation of tree-level Feynman diagrams. Each subdetector is fully modeled and simulated, with relevant parameters tunable through datacards, i.e., a container file in which all the quantities that one wishes to change are collected. This allows a simple and straightforward way to study the impact on physics results of different design and engineering choices. In Figure 5.1, a rendering coming from the visualization editor of GEANT4 can be seen. In particular the view is taken from the ECal position in the direction of the target.

The simulation of each detector is divided into several task-specific sections, each embedded in its own class:

1. *Geometry* : based on a singleton pattern, acts as a container for all the geometric properties of a subdetector.
2. *Detector* : manages the detector construction, defining its shape, size and constituent materials.
3. *Hit* : defines the relevant physical quantities of the interaction of particles with the detector materials, for example the energy, position and time of the interaction.
4. *SD* : makes the detector sensitive, which in GEANT4 jargon means that the detector is treated as an active material, thereby enabling the tracking of interactions occurring within it.
5. *Digitizer* : processes the hit to extract the signal in a form as similar as possible to the one of the real experiment.
6. *Digi* : defines the relevant physical quantities to be saved from the output of the digitization process.
7. *RootIO* : manages the input/output of hit and digi to external ROOT files, used later for analysis.
8. *Messenger* : defines the parameters of the subdetectors that can be changed through datacards.

### 5.2.1 Beam line simulation

The original GEANT4 simulation of PADME did not include any form of modeling of the beam line. Primary positrons were generated just before the target, with their initial angular and energy distribution tuned to mimic the measured properties of the real BTF incoming beam. However, during Run I, a non negligible beam-related background was observed. To study its origin, the last $\sim 15$ m of the BTF transfer line were added to the simulation, starting from dipole 1 at the LINAC exit (see 2.1), including the two quadrupole pairs, the collimators and the last dipole before the PADME target [46]. The simulation helped to identify as the main source of the observed background a $250\mu$m thick beryllium window positioned at the exit of dipole 1 and used to separate the vacuum of the BTF transfer line from the vacuum of PADME. Having full control over the beamline materials also led to the identification of the best material and thickness for a new window, which turned out to be a $125\mu$m MYLAR foil, positioned much upstream before the dipole.

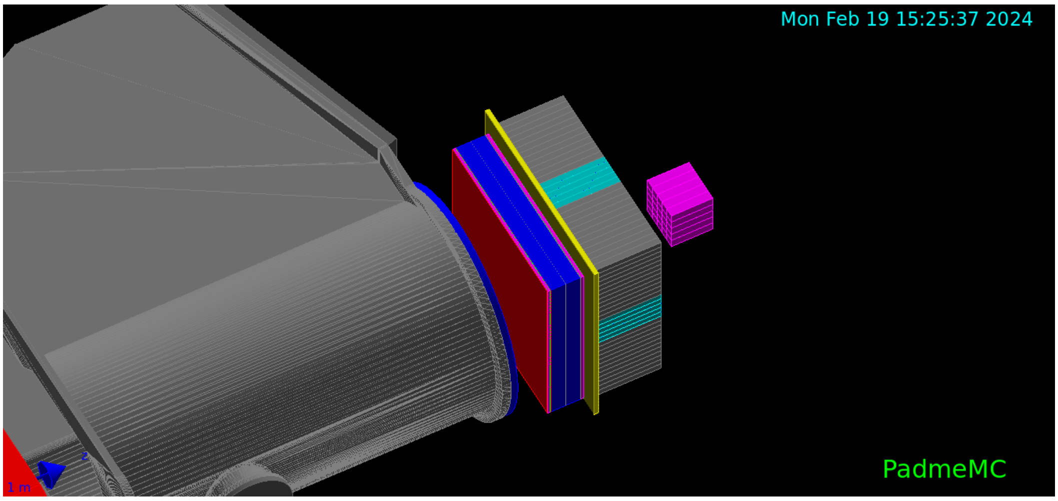


**Figure 5.2.** The PADME Micromegas detector realized in GEANT4, placed on the front face of the ECal.

## 5.3 Micromegas Detector Geometry

As we said, all subdetectors in PADME respect a standard layout for their code, divided into different classes to perform specific jobs, and the Micromegas is no exception. The *Geometry* class takes as input all the design dimensions as taken from mechanical drawings of the chamber. Values stored in this class are for example the size of the detector, the dimensions of drift and amplification gaps, and the thicknesses of all the readout panels materials listed in section 3.4. All of these informations are then used to effectively build the chamber in GEANT4, which can be seen in Figure 5.2. Each layer of the readout plane is simulated, following exactly the description of section 3.4 to accurately mimic the effect of the chamber material on the particles arriving on it, in particular the Coulomb scattering which is crucial to obtain a good spatial resolution. The simulation of each anodic strip as a distinct active volume would have considerably slowed down the overall simulation process. In fact, for the strip-based layout, the detector would comprise more than 4,000 strips. For this reason the segmentation of the copper anodes was modeled as an "effective" density, keeping into account the empty space between a strip and the other. For the strip-based design:

$$\rho_S^{eff} = \rho_{Cu} \times \frac{w}{d} \simeq 6.72\,\mathrm{g\,cm^{-3}} \tag{5.1}$$

where $\rho_{Cu} = 8.96\,\mathrm{g\,cm^{-3}}$ is Copper density, $w$ the strip width and $d$ the pitch.

## 5.4 Micromegas Detector Digitization

The information on the interactions of particles crossing the detector geometry in GEANT4 (deposited energy, time and position of the deposit, etc...) need to be processed in order to obtain something as similar as possible to the output signal of the real detector, a process known as "digitization". For the PADME Micromegas, the *Hit* class stores only the physical informations of the interactions happening in the gas volume:

- Track type (electron, positron, ...)
- Track ID (a number uniquely associated with each particle)
- Time of the energy deposit
- Deposited energy
- Position of the deposit

These quantities are transformed into the detector output using a simple data-driven algorithm to model the ionisation process and the transport of drift electrons, which follows the structure sketched below:

1. The number $N$ of ionisations along the track is randomly drawn from a Poissonian distribution with mean equal to the length of the track $L$ times the expected number of ionisations per unit distance $n \simeq 3$ mm$^{-1}$ ($N = nL$).
2. The $N$ ionisations are uniformly distributed along the track length. This approximation is reasonable if the distance between ionisations is smaller or at least comparable with the strip pitch.
3. The projected positions of the ionisations on the readout planes tell which strips have been hit.
4. The charge of each strip is assigned according to the charge distribution measured during the test beam (Figure 4.5a).
5. The time of each strip is the time of the first deposit. It should be noted that this leads to systematic underestimation of strip times. To include the effect of detector resolution, this value is smeared with a gaussian distribution with zero mean and RMS depending on the strip charge according to the function in Figure 4.18a.

In Figure 5.3 the strip charge and strip time distributions are shown, obtained by sending $10k$ $e^+$ on the Micromegas chamber, with all the other subdetectors of PADME turned off. The chamber was tilted by $\simeq 22°$ to mimic the test beam conditions. We can see that the distributions coming from the simulation capture the essential features of their experimental counterparts. In particular, the time distribution shows a peak at the start of the spectrum similar to the one in Figure 4.5b, even if with smaller prominence, caused by the interaction of the beam with the Micromegas readout planes.

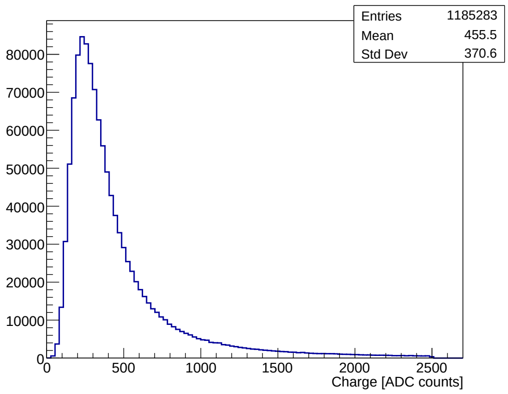


**(a)**

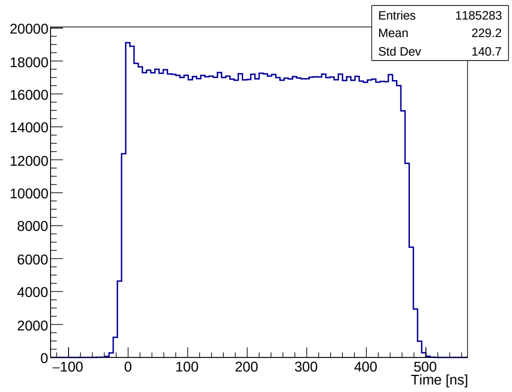


**(b)**

**Figure 5.3.** Strips charge (a) and time distributions (b) obtained from the PADME Micromegas GEANT4 simulation with the chamber tilted by 22°, mimicking the test beam conditions.

Two paths could be followed for the future development of the simulation. The first would be to use PADME's GEANT4 framework for particle generation and their interactions, interfacing it with Garfield++, which would handle the transport of drift electrons and signal generation. This option, however, is difficult to implement and time-consuming. The second option would be to continue using a data-driven approach and rely on experimentally measured distributions for the relevant quantities (such as collected charge, spatial resolution, etc.). This second approach is computationally less expensive and easier to implement.

## 5.5 Monte Carlo studies

### 5.5.1 Particle rate simulation and definition of HV regions

As mentioned earlier when the real detector will be placed inside PADME's experimental apparatus, different parts of it will be exposed to a different particle flux. The occupancy in the central region will be higher, since this is the region where the non-interacting part of the positron beam concentrates. On the other hand the external part of the readout planes will be subject to a lower rate of particles. In resistive anode Micromegas the resistive circuit can be realised in such a way that different parts of the detector have different amplification voltages. By attenuating the amplification voltage in the central region of the Micromegas readout planes it is therefore possible to avoid saturation of the electronics. Therefore, to decide the structure of the resistive circuit, 500 bunch with 6000 $e^+$ each were simulated and the impact point of final state particles on the front face of the tracker was recorded. The two-dimensional distribution of impact points is shown in Figure 5.4a while the x-projection of the same histogram is reported in Figure 5.4b. It can be clearly seen that the occupancy in the center differs from the occupancy at the edge of the detector roughly by a factor of 1000. To equalize the tracker response over all of its extension, the resistive circuit will be divided into three regions with different gain:

1. *Beam region* : it includes the region with a radius between 0 and 60 mm and has a gain attenuation factor of $10^3$.
2. *Corona*: it includes the region between a radius of 60 and 100 mm, and has a gain attenuation factor of $10^2$.
3. *Outer region*: it extends from 100 mm radius outwards. The gain attenuation factor is 1 since here the occupancy is already below 1.

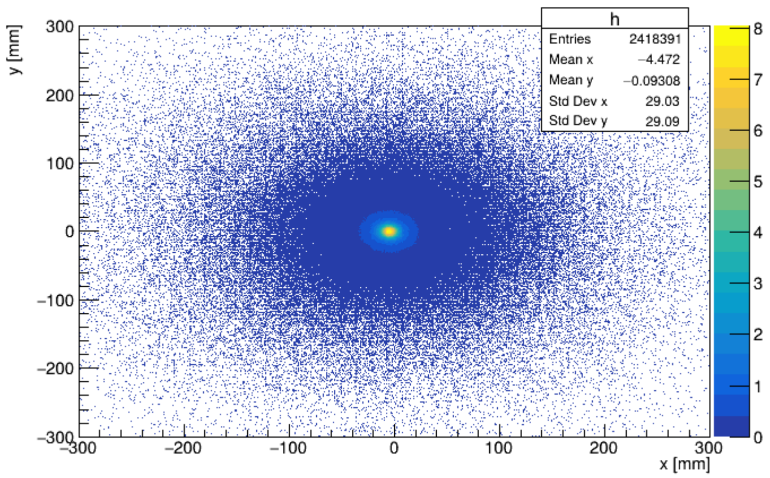


**(a)**

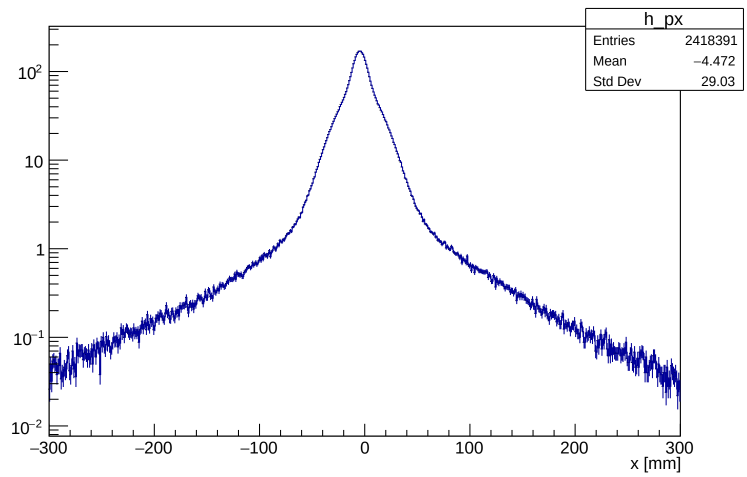


**(b)**

**Figure 5.4.** (a) 2D histogram of impact point of final state particle on the front face of the tracker. (b) X projection of the 2D histogram.

The technical drawing of the resistive layer is shown in Figure 5.5.

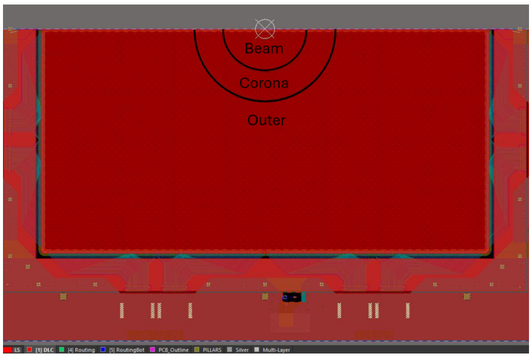


**Figure 5.5.** Technical drawing of PADME Micromegas resistive layer.

### 5.5.2 MC detector spatial and angular resolution estimates

PADME's Micromegas GEANT4 simulation was also used to estimate the spatial and angular resolution of the detector once it will be placed in its final position inside the experiment apparatus. For doing this $10k$ positrons were generated at PADME target position (with PADME target removed) with an angle between 20 mrad and 70 mrad in the $x - z$ plane, to stay inside the detector geometrical acceptance. The tracks inside the tracker were reconstructed using the same software developed for the test beam and described in the previous chapter.

#### Chamber reconstruction resolution (Material Chamber)

As a first step, all PADME subdetectors were turned off, except for the Micromegas. For each event, a linear fit was performed on tracks in the detector, and the tracklet angle, $x_{half}$ and charge centroid were extracted. The distribution for these three quantities were then fitted with a gaussian function (Figure 5.8–5.10), whose RMS was used to estimate the resolution. The angle distributions always peaked at a slightly lower value than the nominal one. This has to do with the way strip times are assigned in the simulation, which is different from the one of the real experiment. As we said, in the simulation the time is taken to be the time of the first deposit; while in the real experiment the time at half-height on the rising edge of the strip signal is used. This leads to an underestimation of strip times, which results in an underestimation of the drift coordinate $z$ and therefore in a smaller reconstructed angle. A sketch of this effect is shown in Figure 5.6. To fix this, in the reconstruction phase, a time correction constant was introduced, corresponding to $\delta t = 25$ ns, half of the APV RC-CR shaper $\tau$. The spatial and angular resolutions obtained with this procedure are shown in Figure 5.7. From Figure 5.7a we can see that the centroid method resolution increases with the track angle. The more inclined the track is, the more strips will be contained in clusters. Since the charge

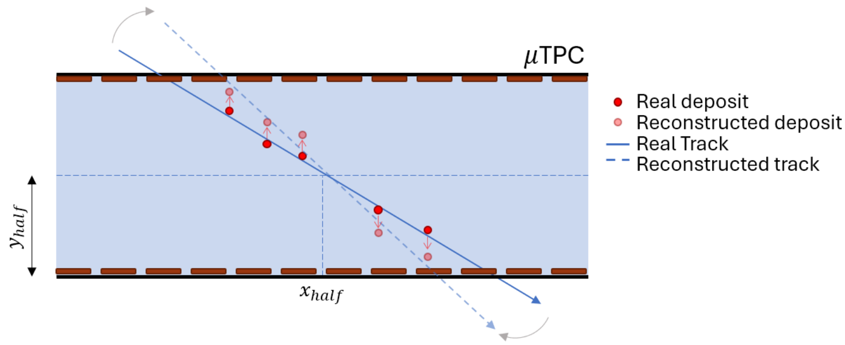


**Figure 5.6.** Sketch of the effect of the underestimation of strip times on reconstructed track angle.

release along the track length is random, the more strips are hit, the more the charge centroid can fluctuate, worsening the resolution. Instead the $\mu$TPC method gives a better resolution at all angles under study. However in this case, we expect the resolution to improve at larger angles, since in that case we have a larger number of points to fit, while we observe a flat trend instead. The same trend is also observed in the angular resolution in Figure 5.7b, which we would also expect to decrease for higher angles. This effect tells us that a dominant contribution to spatial resolution may come from multiple coulomb scattering in the tracker's materials.

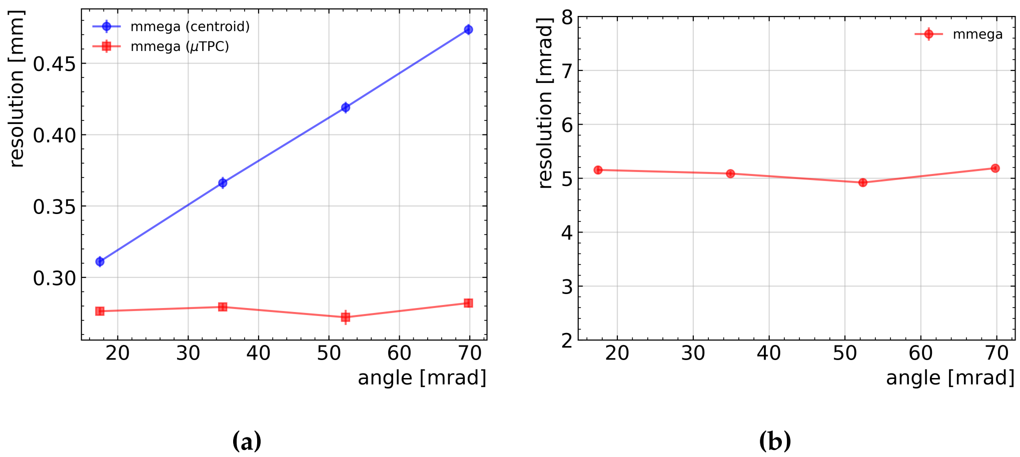


**Figure 5.7.** (a) Spatial resolution as a function of the angle using the centroid (blue) and $\mu$TPC (red) method with only PADME tracker active in the simulation. (b) Angular resolution as a function of the angle with only PADME tracker active in the simulation.

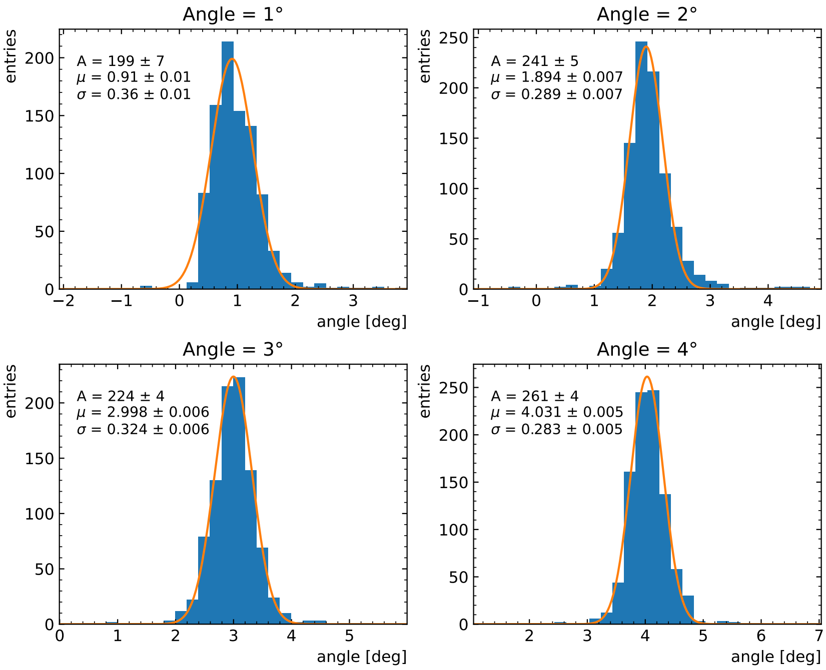


**Figure 5.8.** Gaussian fit for different track inclinations for the distributions of track angle.

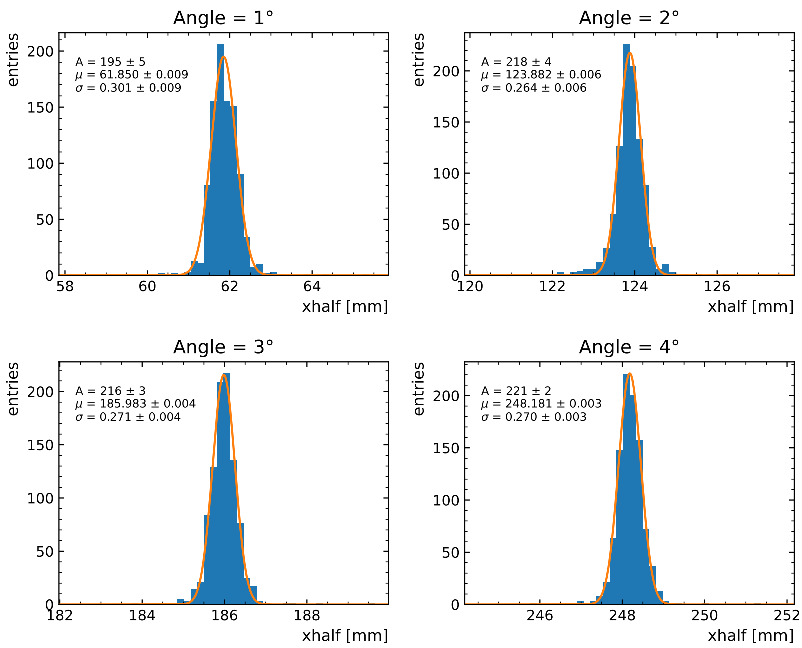


**Figure 5.9.** Gaussian fit for different track inclinations for the distributions of $x_{half}$.

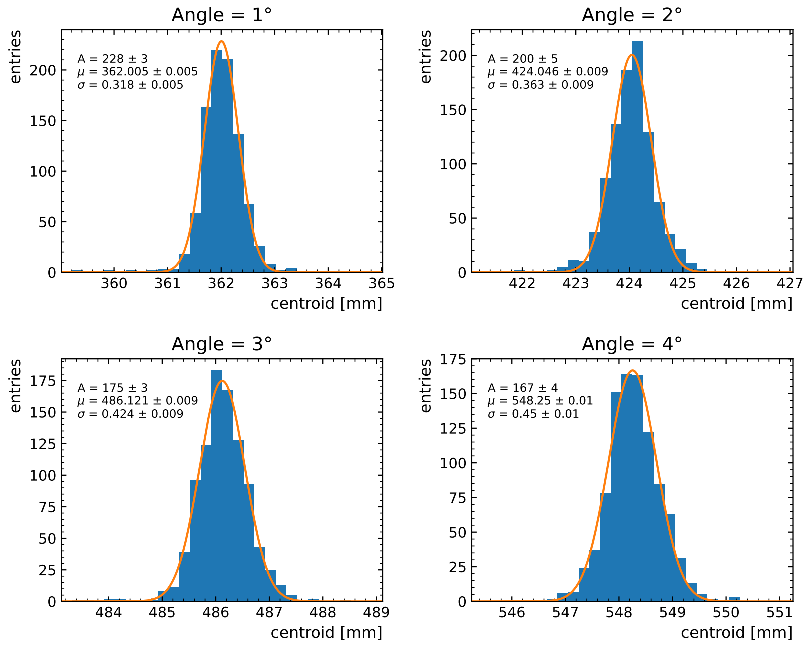


**Figure 5.10.** Gaussian fit for different track inclinations for the distributions of charge centroid.

### Experiment reconstruction resolution (Material Experiment)

In the previous section we analyzed the resolution due to the tracker detector only, but in the real experiment the Micromegas resolution will also depend on the effect of material present in different parts of the experiment. In particular, before reaching the tracker, particles coming from the target region have to cross a $2.5$ mm thick carbon fiber window (described in section 2.2). To study the contribution of other parts of the experiment to the resolution, the analysis of the previous section was repeated using the complete detector description in the simulation. The results can be seen in Figure 5.11. The spatial resolution for centroid and $\mu$TPC have worsened compared to the Micromegas-only case and are now almost the same. From this we understand that the contribution to resolution of PADME materials is dominant with respect to the one of the Micromegas itself. Also the angular resolution worsens and is now around $8$ mrad, $60\%$ higher with respect to Micromegas-only case.

As already said, the worsening of the resolution is dominated by the multiple Coulomb scattering inside the carbon fiber window, placed at the end of the PADME vacuum chamber. One possible workaround considered for future PADME upgrades is to fill the vacuum chamber with Helium gas at atmospheric pressure. This allows to make the window separating air from Helium as thin as possible (ex. $100\mu$m Mylar), reducing multiple scattering. Moreover, due to the very high Helium radiation length ($\simeq$ $5.7$ km), the 3m region between the target and the

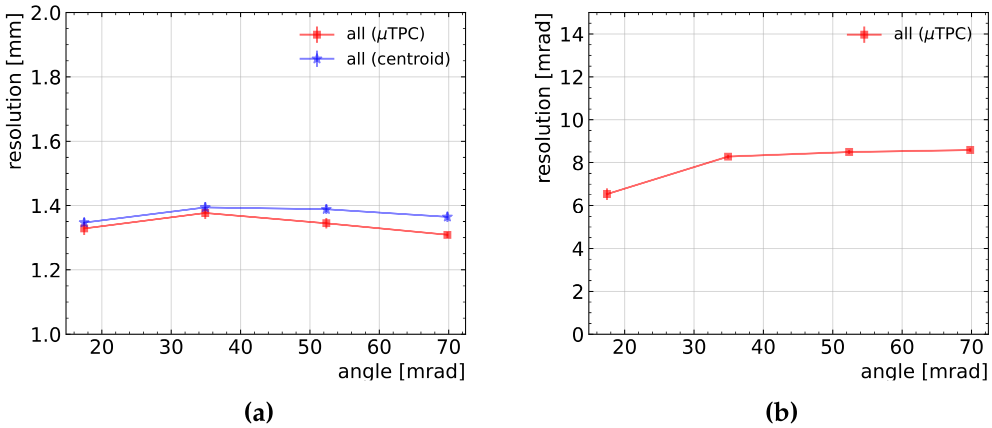


**Figure 5.11.** (a) Spatial resolution as a function of the angle using the centroid (blue) and $\mu$TPC (red) with the full PADME apparatus active. (b) Angular resolution as a function of the angle with the full PADME apparatus active.

tracker corresponds only to $0.05\% X_0$. In comparison, carbon has a radiation length of $\simeq 19.32$ cm, so the $2.5$ mm window thickness corresponds to $1.3\% X_0$ [2].

### 5.5.3 Invariant mass resolution

In a fixed-target experiment, such as PADME, the invariant mass of a two-body system can be measured from both the initial and final state through the following equations:

$$\sqrt{s_i} = \sqrt{2E_{beam}m_e} \tag{5.2}$$

$$\sqrt{s_f} = \sqrt{4E_1E_2\sin^2\left(\frac{\Delta\Theta}{2}\right)} \tag{5.3}$$

where $m_e = 0.511$ MeV is the electron mass and $E_{beam}$ is the energy of the positron beam. $E_1$ and $E_2$ are the energies of the two particles in the final state, while $\Delta\Theta = \theta_1 + \theta_2$ is the angle between them. Notice that the two equations hold in the $m_e \ll E_1, E_2$ limit, which is always satisfied in the PADME experiment. Moreover, in the specific case of PADME, the angles $\theta_1$, $\theta_2$ of the particles lying in the calorimeter acceptance are small ($< 100$ mrad), so Equation 5.3 can be further simplified:

$$\sqrt{s_f} \simeq \sqrt{E_1E_2\Delta\Theta^2} = \sqrt{E_1E_2\frac{(\vec{r_1}-\vec{r_2})^2}{z^2}} \tag{5.4}$$

where $\vec{r_i} = (x_i, y_i)$ is the impact point of the i-th particle on the calorimeter face and $z$ is the distance between the interaction vertex and the calorimeter. However, to use

[2] Informations on materials' radiation lengths have been taken from : `https://pdg.lbl.gov/2024/AtomicNuclearProperties/index.html`

this equation it is necessary to assume that the final state particles are produced at the target position, fixing $z$ equal to the target-ECal distance. With the introduction of the Micromegas inside PADME apparatus, the impact point of the final state particles can be determined with a precision almost 10 times higher with respect to the ECal, due to its readout planes high granularity. To study the resolution in

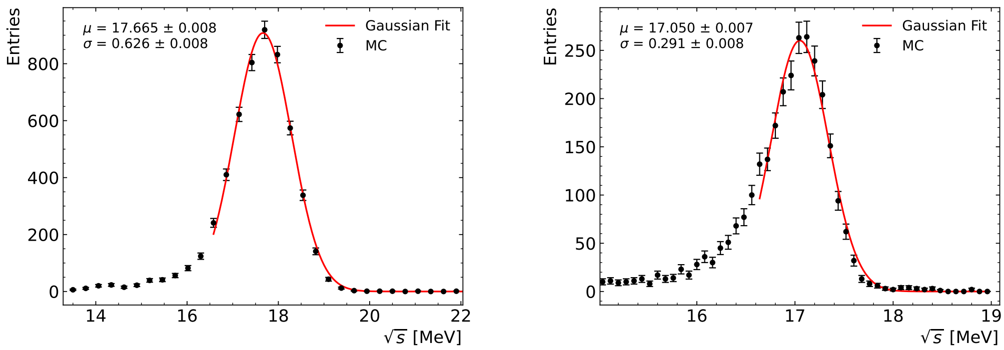


**(a)** **(b)**

**Figure 5.12.** Reconstructed invariant mass of BhaBha events measured with (a) ECal (b) Micromegas using $\mu$TPC method.

invariant mass, 10k BhaBha events were simulated within PADME acceptance with a positron beam energy of $E_b = 289$ MeV using the full MonteCarlo simulation. The energies of the final electron and positron were computed using a *Constant Radius* algorithm to clusterize energy deposits in the ECal crystals, while the impact points on the calorimeter face were computed with a *energy weighted average* of the centers of the crystals belonging to the same cluster. To compute the invariant mass using the Micromegas detector, the impact points were determined by extrapolating the tracks' fit, obtained with the $\mu$TPC method, to the rear face of the chamber. This method was preferred to the charge centroid since it was shown in subsection 5.5.2 to have a better spatial resolution. The results are shown in Figure 5.12. The Gaussian fit has been performed in the region around the peak of the distribution to exclude the tail at lower values of the invariant mass, caused by energy losses in the ECal and by the crystal clustering procedure.

The resolutions were taken to be the RMS of the fitted functions and they were found to be:

$$\sigma_{\sqrt{s}}^{ECal} = 0.626 \pm 0.008 \text{ MeV} \tag{5.5}$$

$$\sigma_{\sqrt{s}}^{MM} = 0.291 \pm 0.008 \text{ MeV} \tag{5.6}$$

Using the Micromegas detector to measure the invariant mass provides a resolution twice as good as the one obtained from the measurement done only with the calorimeter. However, the incorporation of the Micromegas tracker into the apparatus enables the direction of the final state particles to be determined directly through the use of the $\mu$TPC method, thus eliminating the need for any assumptions regarding the interaction point. The distribution obtained in this way is shown in Figure 5.13a, and the found resolution on invariant mass is:

$$\sigma_{\sqrt{s}}^{\mu TPC} = 2.7 \pm 0.1 \text{ MeV} \tag{5.7}$$

The resolution on $\sqrt{s}$ achieved with the ECal is more than four times better than the one obtained using the $\mu$TPC angles. Nevertheless, it is important to highlight

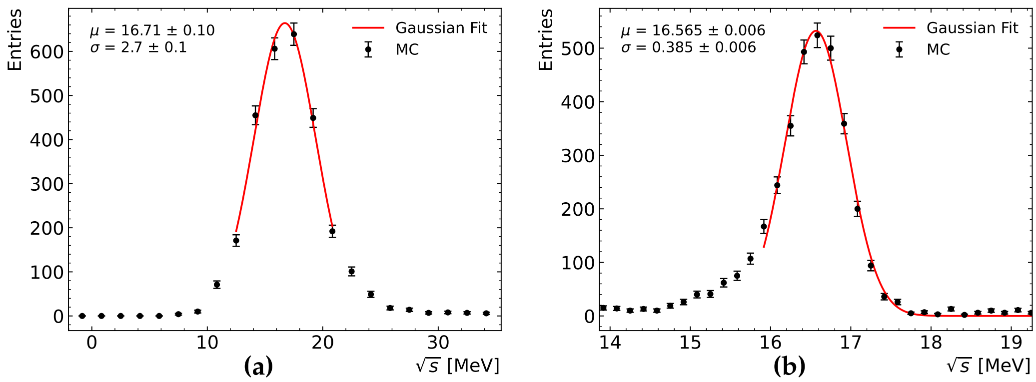


**Figure 5.13.** Reconstructed invariant mass of BhaBha events measured with Micromegas using the direction coming from the $\mu$TPC fit (a) including (b) excluding the materials of the readout planes from the simulation.

that the former strongly depends on the prompt decay assumption. This is not true for instance in the context of the search for long-lived particles, where the vertex position cannot be assumed to be known. The removal of the carbon fiber window would result in an improvement in resolution of approximately $30\%$, although it should be noted that the most significant enhancement would be achieved through the optimization of the readout plane materials within the chamber. For instance, a simulation performed without the readout planes showed a resolution of $0.39$ MeV, which is better than the current resolution achieved with the ECal (see Figure 5.13b).

### 5.5.4 MC vertex resolution estimates

Adding a tracker to the PADME experiment is also useful in the context of its search for long-lived particles. It allows us to reconstruct the position of the interaction vertex of the final state $e^+e^-$ pair and, therefore, identify possible displaced vertices. To study the capability of PADME tracker to reconstruct the interaction vertex, a sample of $10k$ BhaBha events with final $e^+e^-$ lying inside the Micromegas acceptance was generated in *CalcHep* and used as a particle generator in the complete experiment GEANT4 simulation. An example of how a typical BhaBha scattering final state looks like in the ECal and the Micromegas is shown in Figure 5.14. To measure the interaction vertex two different methods have been studied:

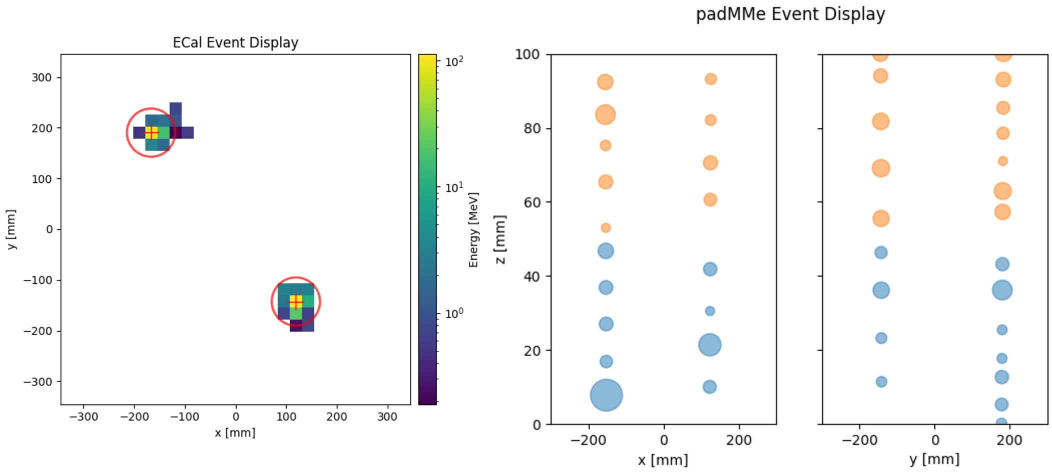


**(a)** **(b)**

**Figure 5.14.** (a) ECal event display and (b) PADME Micromegas event display of a BhaBha scattering final state. In blue the deposits in the first half of the chamber are shown, in orange the deposits in the second half. Size of markers is proportional to charge.

1. *Point of closest approach method* : this approach is based solely on the Micromegas chamber. The final state particles are tracked using the $\mu$TPC method, and then the point of minimum distance between the two tracks is computed.

2. *Invariant mass method* : Equation 5.4 can be used to compute the $z$ coordinate of the interaction vertex, if one assumes the value of the invariant mass as known from the initial state through Equation 5.2. This method does not give information on the beam spot, namely the $x$ and $y$ coordinates of the vertex.

### Point of closest approach method

The point of closest approach method is based on the following procedure:

1. All tracks in the $x$-$z$ and $y$-$z$ planes of the tracker are linearly fitted separately.

2. To assign a track in the $x$-$z$ to the one in $y$-$z$ corresponding to the same particle, tracks in the two views are combined until the distance between the estrapolated exit point from the tracker and one of the ECal deposits is minimum.

3. For each particle the fits in the $x$-$z$ and $y$-$z$ are transformed into a single line in 3d space. A line in 3D space is described by a vector equation of the form:

$$\vec{r} = \vec{r_0} + \vec{d} \cdot t \tag{5.8}$$

The two vectors $\vec{r_0}$ and $\vec{d}$ can be expressed in terms of the intercepts (q) and angular coefficients (m) of the $x$ and $y$ projections:

$$\vec{d} = \left(\frac{1}{m_x}, \frac{1}{m_y}, 1\right) \qquad \vec{r_0} = \left(-\frac{q_x}{m_x}, -\frac{q_x}{m_x}, 0\right) \tag{5.9}$$

4. For events in which two tracks were reconstructed the POCA between the two tracks is computed. The point of closest approach is computed using the following expression:

$$t_{POCA} = -\frac{(\vec{d_2} - \vec{d_1}) \cdot (\vec{r_{02}} - \vec{r_{01}})}{|\vec{d_2} - \vec{d_1}|^2} \tag{5.10}$$

   and substituting $t$ with $t_{POCA}$ in Equation 5.8.

This procedure has been repeated in 4 different configurations to understand the contribution of the materials of the experiment on the vertex resolution : complete experiment active; carbon fiber window removed, carbon window and chamber readout planes removed, only tracker gas volume and ECal active. The results are shown in Figure 5.15.

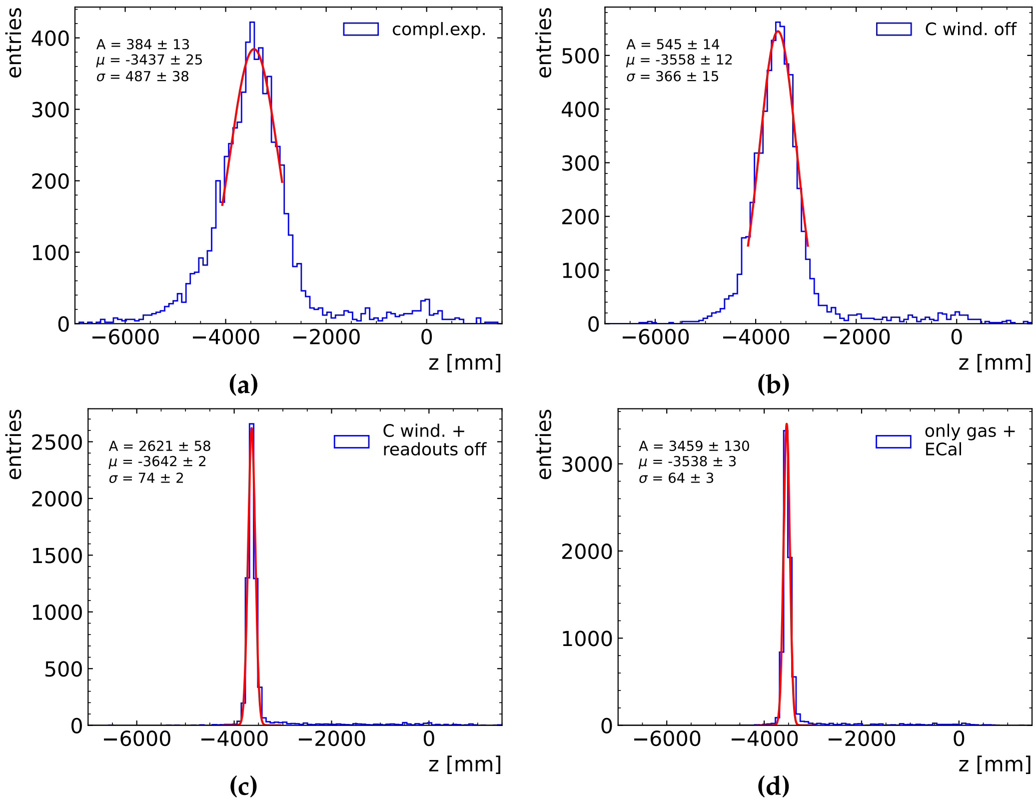


**Figure 5.15.** $z$ coordinate of the point of closest approach between $e^+$ and $e^-$ tracks for different configurations: (a) complete experiment, (b) carbon window removed, (c) carbon window and tracker planes removed, (d) tracker gas volume and ECal only.

The vertex $z$ coordinate distributions peak at around $\sim -3500$ mm, which is compatible with the position of the target in the simulation ($-3501.451$ mm) with respect to the front face of the chamber. Also in this case, the strip time correction $\delta t$ introduced before to correctly reconstruct the track angle is important to obtain the correct vertex position. The removal of the carbon fiber window from the apparatus, improves the $z$ vertex coordinate resolution, by $\sim 25\%$ (see Figure 5.15b). However, resolution is most significantly influenced by the readout planes of the chamber. As demonstrated in Figure 5.15c, the removal of these planes results in a significant enhancement, providing an almost 5 times better resolution. In this configuration the resolution is very similar to the case in which only the tracker gas volume and the ECal are left active (see Figure 5.15d), so the contribution to the resolution given by other parts of the experiment is negligible. Values of the resolution of the vertex $z$ coordinates obtained with the different configurations are summarized in Table 5.1.

**Table 5.1.** Values of the fitted resolutions for the vertex $z$ coordinate in the different configurations.

| Mode | $\sigma_z$ vertex [mm] |
|---|---|
| compl. exp | $487 \pm 38$ |
| C wind. off | $366 \pm 15$ |
| C wind. + readouts off | $74 \pm 2$ |
| only gas + ECal | $64 \pm 3$ |

### Invariant mass approach

If we solve Equation 5.3 for $z$, we can compute the vertex $z$ coordinate with the following expression:

$$z = -\frac{\sqrt{E_1 E_2 (\vec{r_1} - \vec{r_2})^2}}{\sqrt{s}} \tag{5.11}$$

where we can use substitute to $\sqrt{s}$ the invariant mass computed from the initial state through Equation 5.2. The minus sign has been added in the formula since we are taking as the origin of our $z$ axis the position of the final particles impact points. In Figure 5.16 the distributions of the vertex $z$ coordinate obtained in this way are shown; with the impact points taken at the front face for the ECal (left) and on the rear face for the Micromegas (right).

Also in this case the Micromegas gives twice as good performances with respect to the use of the calorimeter alone, with the two resolutions being:

$$\sigma_z^{vtx} = 115 \pm 2\,\text{mm} \qquad \text{(ECal)} \tag{5.12}$$

$$\sigma_z^{vtx} = 64 \pm 2\,\text{mm} \qquad \text{(MM)} \tag{5.13}$$

If instead of the impact point on the Micromegas rear face we use the angles obtained

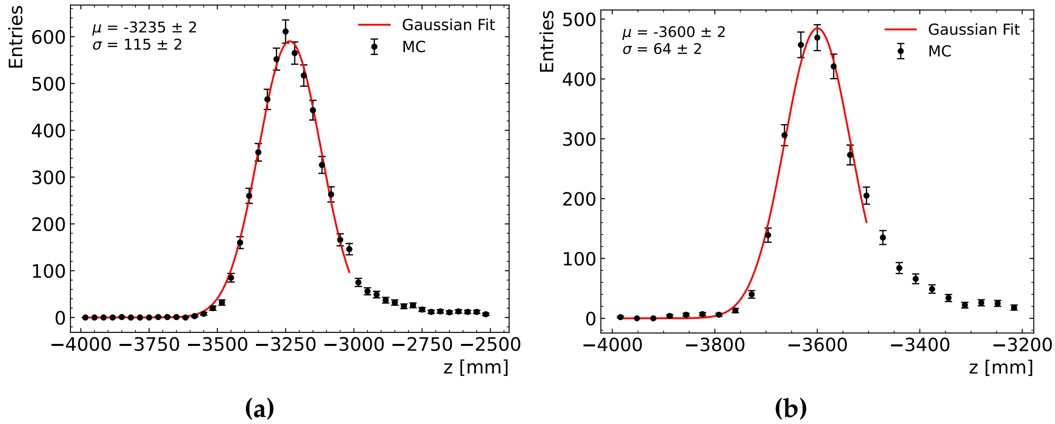


**Figure 5.16.** Vertex $z$ coordinate measured assuming the knowledge of the initial state invariant mass with : (a) ECal (b) Micromegas using $\mu$TPC method.

with the $\mu$TPC fit we obtain (see Figure 5.17):

$$\sigma_z^{vtx} = 551 \pm 28 \text{ mm} \qquad (\mu\text{TPC}) \tag{5.14}$$

that, as we could have expected, is compatible with the value obtained in section 5.5.4 using the point of closest approach, which only relied on the chamber measurement without the need for the calorimetric information.

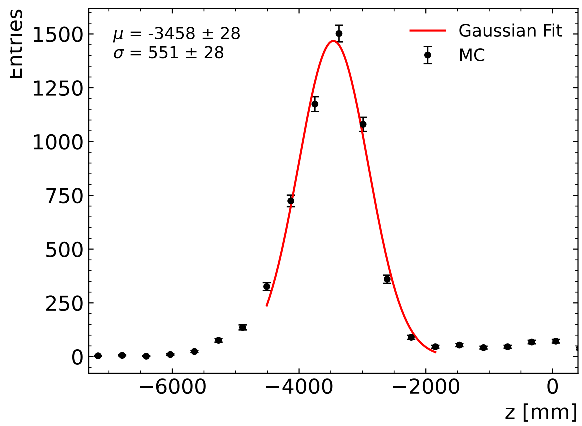


**Figure 5.17.** Vertex $z$ coordinate measured assuming the knowledge of the initial state invariant mass using the Micromegas. The angles are computed from the $\mu$TPC fit of the tracks.

### 5.5.5 Beam spot resolution

The reconstructed vertex $z$ coordinate is not the only important parameter in vertex reconstruction. To ensure that the two $e^+e^-$ tracks originate from the same point we should also study how well the $x$ and $y$ coordinates of the interaction vertex can be reconstructed. This can be accomplished with the point of closest approach method. The knowledge of the transverse coordinates allows to understand if the reconstructed particle track is coming from a point compatible with the position of the target. Tracks with a beam spot outside the target have low-compatibility with the hypothesis of being produced inside the target and can therefore be rejected. The 2D histograms of the reconstructed $x$ and $y$ reconstructed vertex coordinate are shown in Figure 5.18 for the same four configurations listed in the previous section while the fitted resolution are reported in Table 5.2.

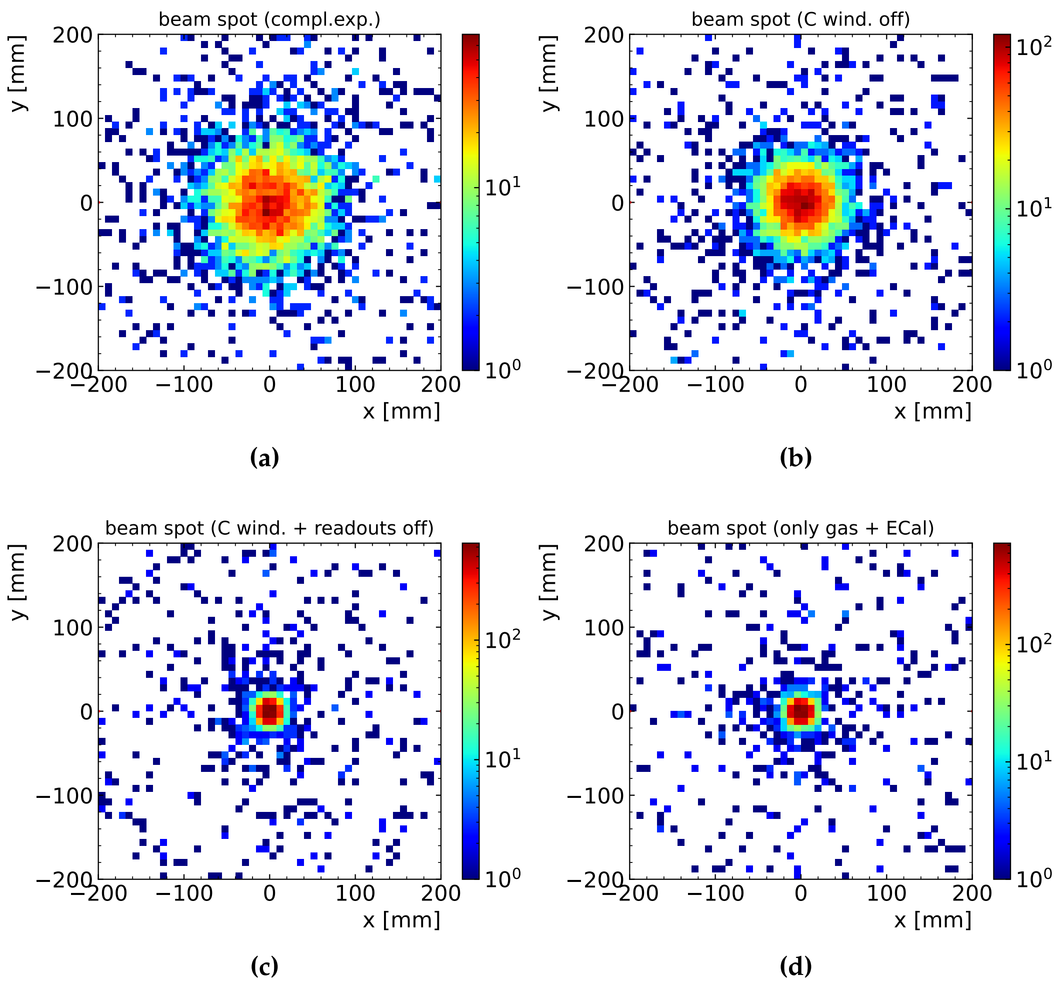


**Figure 5.18.** 2D distributions of the $x - y$ coordinates of the point of closest approach of $e^+$ and $e^-$ tracks for different configurations : (a) complete PADME experiment active, (b) Carbon fiber window removed, (c) Carbon fiber window and tracker readout planes removed, (d) Only tracker gas volume and ECal active.

As for the vertex $z$ coordinate, also for the beam spot the biggest contribution to the broadening of the resolution comes from multiple Coulomb scattering inside the readout planes of the tracker. However, in this case, removing the carbon fiber

**Table 5.2.** Values of the fitted resolutions for the vertex $x$ and $y$ coordinates in different configurations.

| Mode | $\sigma_x$ vertex [mm] | $\sigma_y$ vertex [mm] |
|---|---|---|
| compl. exp | $37.25 \pm 0.77$ | $38.15 \pm 0.73$ |
| C wind. off | $24.96 \pm 0.38$ | $25.32 \pm 0.41$ |
| C wind. + readouts off | $7.81 \pm 0.11$ | $8.59 \pm 0.10$ |
| only gas + ECal | $8.59 \pm 0.16$ | $8.22 \pm 0.11$ |

window at the vacuum chamber exit would bring the resolution to the level of $2.5$ cm which is comparable with the transverse size of PADME target ($2$ cm $\times$ $2$ cm) and can therefore help to identify tracks not originating from the target region.

# Chapter 6

# Conclusions

For Run IV, foreseen for January 2025, PADME plans to search for $X_{17}$ through resonant production by impinging a positron beam on a diamond target. To confirm the existence of $X_{17}$ PADME will look for an excess in the ratio between $e^+e^-$ and $\gamma\gamma$ final states versus $\sqrt{s}$. This measurement requires excellent tagging efficiency to distinguish charged leptons from photons. Due to its low segmentation, the current ETag detector was not suitable for this purpose, especially with a view to PADME intensity increase. For this reason, a new gaseous tracker of the Micromegas type has been designed to be added in front of the electromagnetic calorimeter. A prototype of the detector was tested during a one-week long test beam at the LNF-BTF. The feasibility of the $\mu$TPC method was successfully demonstrated, reaching a precision of less than $1^\circ$ in track angle reconstruction. The drift velocity of the ArCF4Iso (88:10:2) gas mixture, was measured for different values of the drift field and found to be 10.4 cm/$\mu$s at 3 kV, in agreement with *Garfield*++ simulations. The cluster efficiency of the tracker prototype was also measured for different amplification gap voltages and was maximum at 500 V, where it reached $\sim 95\%$. The resolution on the drift coordinate was shown to be under $1$ mm, which was PADME specific request, reaching the level of $880$ $\mu$m at the average strip charge value. The capability of the chamber to reconstruct multiple hits on the same strip was also studied, yielding a minimum time between hits on the same strip to enable double-peak separation of $\sim 325$ ns . Alongside the experimental activities, a complete simulation of the new PADME tracker, based on the GEANT4 package, was developed and included into the pre-existing PADME Monte Carlo simulation framework. The simulation was used to help the design process, in particular to decide the structure of the detector resistive layer, which will be divided into three regions with increasing radius to cope with the higher flux of particles in the central part of the detector. The use of the simulation also allowed to estimate the detector spatial and angular resolution, and identify the contribution of the different materials present in the PADME experiment to those quantities. The intrinsic tracker spatial resolution was found to be around $0.4$ mm, while the angular resolution around $5$ mrad. The effect of PADME carbon fiber window worsens the spatial and angular resolutions to $1.35$

mm and $8$ mrad, respectively. However it was found that the dominant contribution to it comes from the materials composing the detector readout planes. The detector capability to reconstruct the coordinates of the interaction vertex was quantified. A resolution of $49$ cm was found for the vertex $z$ coordinate, and of $\sim 3.8$ cm for the $x$ and $y$ coordinates. Lastly, the resolution in invariant mass was also estimated, finding a value of 2.2 MeV. This value is worse than the one obtained with the ECal which has the disadvantage of relying on the assumption that the decay occurs at the target position.

All of the quantities under study would benefit from replacing the PADME carbon fiber window with a lighter material, a possibility already considered by the collaboration. However, to take full advantage of the intrinsic chamber performances, which have been shown to be very satisfactory, the area that would lead to the most tangible improvement would be to reduce the material budget introduced by the readout planes of the tracker. In this way a vertex resolution of approximately 7 cm and a beam spot resolution < $1$ cm, within the transverse area of the PADME target, could be achieved. This could have a critical impact on rejecting final particles not originating from the target region. In addition, the resolution in invariant mass would reach the level of $0.39$ MeV, which is less than the current precision achieved with the calorimeter alone, while also having the further advantage of not making any assumptions about the interaction vertex. In a more general scenario, the performance of the Micromegas chamber would benefit a lot from higher beam energy compared to the one used in X17 dedicated run. In this condition the full potential of the new tracker could be exploited, since higher energies would mitigate the influence of multiple scattering and increase the flight distance of a hypothetical long-lived particle, making it easier to look for a displaced vertex.

# Acknowledgements

Now that all the physics has been left in the conclusions, it's time to talk about the people without whom this thesis (or to be more precise, the work behind it) would have been certainly harder and less enjoyable.

First of all, I would like to thank Prof. Mauro Raggi, who had the patience to be my supervisor "squared" and effortlessly checked what I wrote. He is such an eruption of ideas that it is almost impossible to always keep up with all his suggestions. But to the extent that I was able to keep up with the speed of his thoughts every one of them was precious. A big, heartfelt thank you goes to Dr. Giada Mancini, who was a fantastic co-advisor, providing me with unwavering help and support. Together we shared a nine-month "labor", mine to write this thesis, hers to carry her beautiful newborn baby. Then I must mention and thank Dr. Emanuele Leonardi, who shared with me his programming tips I'll always apply from now on. One above all *"it's evident that you're not a programmer, you should name your files with the year first, then the month and only in the end the day"*. I cannot thank Dr. Paola Gianotti enough, a true gem at Frascati National Laboratories. Her guidance has been priceless in navigating the bureaucratic jungle of INFN. Speaking of the Frascati National Laboratories, I want to thank Dr. Chiara Arcangeletti and Dr. Leonardo Vannoli, for making me feel part of the team straight away and making my first test beam as instructive and enjoyable as it could be.

But the real driving force that made everything easier day by day, twenty-four hours a day, was due to the wonderful people I had the chance to share my journey with in the Physics Department. I'd like to thank Danilo, Andrea, Camilla, Leonardo, Marco, Niccolò, Susanna, Luana, Elisa, Ottavia, Irene and Lorenzo. You all made this place the best I could wish to spend these years in. It was a lot of fun to see how each of our theses evolved and are evolving, and to have countless conversations on how to solve each other's problems, even if we now belong to completely different areas of Physics.

Finally, I need to thank my family. Mom and Dad, you made the journey seem so simple. With you having the chance to study what I like seemed always granted.

# Bibliography


[1] F. Zwicky, "Die rotverschiebung von extragalaktischen nebeln," *Helv. Phys. Acta*, vol. 6, pp. 110–127, 1933.

[2] V. C. Rubin *et al.*, "Rotational properties of 21 SC galaxies with a large range of luminosities and radii, from NGC 4605 /R = 4kpc/ to UGC 2885 /R = 122 kpc/," *The Astrophysical Journal*, vol. 238, 1980, ISSN: 0004-637X. DOI: 10.1086/158003.

[3] D. Clowe *et al.*, "A direct empirical proof of the existence of dark matter," *The Astrophysical Journal*, vol. 648, pp. 109–113, 2006.

[4] D. N. Spergel and P. J. Steinhardt, "Observational evidence for self-interacting cold dark matter," *Physical Review Letters*, vol. 84, no. 17, 2000, ISSN: 10797114. DOI: 10.1103/PhysRevLett.84.3760.

[5] N. Aghanim *et al.*, "Planck 2018 results: VI. Cosmological parameters," *Astronomy and Astrophysics*, vol. 641, 2020, ISSN: 14320746. DOI: 10.1051/0004-6361/201833910.

[6] M. Tegmark *et al.*, "Cosmological parameters from sdss and wmap," *Physical Review D - Particles, Fields, Gravitation and Cosmology*, vol. 69, no. 10, 2004, ISSN: 15502368. DOI: 10.1103/PhysRevD.69.103501.

[7] J. L. Feng, "The wimp paradigm: Theme and variations," *SciPost Physics Lecture Notes*, vol. 71, 2023, ISSN: 25901990. DOI: 10.21468/SciPostPhysLectNotes.71.

[8] M. Raggi and V. Kozhuharov, "Results and perspectives in dark photon physics," *Rivista del Nuovo Cimento*, vol. 38, no. 10, pp. 449–505, Oct. 2015, ISSN: 18269850. DOI: 10.1393/ncr/i2015-10117-9.

[9] A. Filippi and M. De Napoli, "Searching in the dark: the hunt for the dark photon," Jun. 2020. DOI: 10.1016/j.revip.2020.100042. [Online]. Available: http://arxiv.org/abs/2006.04640%20http://dx.doi.org/10.1016/j.revip.2020.100042.

[10] M. E. Rose, "Internal pair formation," *Phys. Rev.*, vol. 76, pp. 678–681, 5 Sep. 1949. DOI: 10.1103/PhysRev.76.678. [Online]. Available: https://link.aps.org/doi/10.1103/PhysRev.76.678.

[11] J. Gulyás *et al.*, "A pair spectrometer for measuring multipolarities of energetic nuclear transitions," *Nuclear Instruments and Methods in Physics Research Section A: Accelerators, Spectrometers, Detectors and Associated Equipment*, vol. 808, pp. 21–28, 2016, ISSN: 0168-9002. DOI: `10.1016/j.nima.2015.11.009`. [Online]. Available: `https://www.sciencedirect.com/science/article/pii/S0168900215013716`.

[12] J. Agarwala *et al.*, "Construction and test of the sm1 type micromegas chambers for the upgrade of the atlas forward muon spectrometer," *Nuclear Instruments and Methods in Physics Research, Section A: Accelerators, Spectrometers, Detectors and Associated Equipment*, vol. 1040, Oct. 2022, ISSN: 01689002. DOI: `10.1016/j.nima.2022.167285`.

[13] A. J. Krasznahorkay *et al.*, "Observation of anomalous internal pair creation in be 8: A possible indication of a light, neutral boson," *Physical Review Letters*, vol. 116, no. 4, Jan. 2016, ISSN: 10797114. DOI: `10.1103/PhysRevLett.116.042501`.

[14] A. J. Krasznahorkay *et al.*, "New results on the 8be anomaly," in *Journal of Physics: Conference Series*, vol. 1056, Institute of Physics Publishing, Jul. 2018. DOI: `10.1088/1742-6596/1056/1/012028`.

[15] A. J. Krasznahorkay *et al.*, "On the creation of the 17 MeV X boson in the 17.6 MeV M1 transition of 8 Be," Tech. Rep., 2017.

[16] A. J. Krasznahorkay *et al.*, "New evidence supporting the existence of the hypothetic x17 particle," Oct. 2019. [Online]. Available: `http://arxiv.org/abs/1910.10459`.

[17] D. S. Firak *et al.*, "Confirmation of the existence of the x17 particle," *EPJ Web of Conferences*, vol. 232, p. 04 005, 2020. DOI: `10.1051/epjconf/202023204005`.

[18] A. J. Krasznahorkay *et al.*, "New anomaly observed in supports the existence of the hypothetical x17 particle," *Physical Review C*, vol. 104, no. 4, Oct. 2021, ISSN: 24699993. DOI: `10.1103/PhysRevC.104.044003`.

[19] J. L. Feng *et al.*, "Dynamical evidence for a fifth force explanation of the atomki nuclear anomalies," *Physical Review D*, vol. 102, no. 3, Aug. 2020, ISSN: 24700029. DOI: `10.1103/PhysRevD.102.036016`.

[20] A. J. Krasznahorkay *et al.*, "Observation of the x17 anomaly in the decay of the giant dipole resonance of $^{8}$be," Aug. 2023. [Online]. Available: `http://arxiv.org/abs/2308.06473`.

[21] G. A. Fisher *et al.*, "Giant e1 resonances in be from the reaction li(p, $\gamma$) be," Tech. Rep. 1, 1976.

[22] D. S. Alves *et al.*, *Shedding light on X17: community report*, Mar. 2023. DOI: `10.1140/epjc/s10052-023-11271-x`.

[23] M. Raggi and V. Kozhuharov, "Proposal to Search for a Dark Photon in Positron on Target Collisions at da Φ NE Linac," *Advances in High Energy Physics*, vol. 2014, 2014, ISSN: 16877365. DOI: 10.1155/2014/959802.

[24] M. Raggi *et al.*, "The padme experiment technical proposal," Dec. 2016. DOI: 10.15161/OAR.IT/77033.

[25] F. Oliva, "Operation and performance of the active target of PADME," *Nuclear Instruments and Methods in Physics Research Section A: Accelerators, Spectrometers, Detectors and Associated Equipment*, vol. 958, p. 162 354, Apr. 2020, ISSN: 0168-9002. DOI: 10.1016/J.NIMA.2019.162354.

[26] G. Piperno, "The PADME electromagnetic calorimeter," in *Journal of Physics: Conference Series*, vol. 1162, Institute of Physics Publishing, Apr. 2019. DOI: 10.1088/1742-6596/1162/1/012031.

[27] E. Leonardi *et al.*, "Evaluation of clustering algorithms at the < 1 gev energy scale for the electromagnetic calorimeter of the padme experiment," in *Journal of Physics: Conference Series*, vol. 898, Institute of Physics Publishing, Nov. 2017. DOI: 10.1088/1742-6596/898/7/072019.

[28] A. Frankenthal *et al.*, "Characterization and performance of padmes cherenkov-based small-angle calorimeter," *Nuclear Instruments and Methods in Physics Research Section A: Accelerators, Spectrometers, Detectors and Associated Equipment*, vol. 919, pp. 89–97, Mar. 2019, ISSN: 0168-9002. DOI: 10.1016/J.NIMA.2018.12.035.

[29] F. Oliva, "The charged particle veto system of the PADME experiment," *Nuclear Instruments and Methods in Physics Research Section A: Accelerators, Spectrometers, Detectors and Associated Equipment*, vol. 936, pp. 259–260, Aug. 2019, ISSN: 0168-9002. DOI: 10.1016/J.NIMA.2018.10.147.

[30] S. Ivanov *et al.*, "Profile Characterization of the PADME Experiments Positron Beam Using a TimePix3 Sensor Array," *Journal of Physics: Conference Series*, vol. 2668, no. 1, p. 012 009, Dec. 2023, ISSN: 1742-6596. DOI: 10.1088/1742-6596/2668/1/012009. [Online]. Available: https://iopscience.iop.org/article/10.1088/1742-6596/2668/1/012009%20https://iopscience.iop.org/article/10.1088/1742-6596/2668/1/012009/meta.

[31] L. Darmé *et al.*, "Resonant search for the X17 boson at PADME," *Physical Review D*, vol. 106, no. 11, p. 115 036, Dec. 2022, ISSN: 24700029. DOI: 10.1103/PHYSREVD.106.115036/FIGURES/5/MEDIUM. [Online]. Available: https://journals.aps.org/prd/abstract/10.1103/PhysRevD.106.115036.

[32] F. Sauli, *Gaseous Radiation Detectors : Fundamentals and Applications*. Oxford University Press, 2015, vol. 36, ISBN: 978-1-009-29120-0. DOI: 10.1017/9781009291200.

[33] R. L. Workman *et al.*, "Review of particle physics," *PTEP*, vol. 2022, p. 083C01, 2022.

[34] L. D. Landau, "On the energy loss of fast particles by ionisation," *J. Phys. (USSR)*, vol. 8, D. ter Haar, Ed., 1944. DOI: 10.1016/b978-0-08-010586-4.50061-4.

[35] W. Blum *et al.*, *Particle detection with drift chambers*. Springer, 2008, p. 448, ISBN: 9783540766834.

[36] J. D. Jackson, *Classical Electrodynamics-Third Edition*. 1998.

[37] G. Charpak *et al.*, "Micromegas, a multipurpose gaseous detector," Tech. Rep., 2002, pp. 26–36.

[38] I. Giomataris *et al.*, "Micromegas in a bulk," *Nuclear Instruments and Methods in Physics Research, Section A: Accelerators, Spectrometers, Detectors and Associated Equipment*, vol. 560, no. 2, pp. 405–408, May 2006, ISSN: 01689002. DOI: 10.1016/j.nima.2005.12.222.

[39] T. Alexopoulos *et al.*, "Performance studies of resistive-strip bulk micromegas detectors in view of the ATLAS New Small Wheel upgrade," *Nuclear Instruments and Methods in Physics Research Section A: Accelerators, Spectrometers, Detectors and Associated Equipment*, vol. 937, pp. 125–140, Sep. 2019, ISSN: 0168-9002. DOI: 10.1016/J.NIMA.2019.04.050.

[40] L. Ambrosi *et al.*, "Characterization of charge spreading and gain of encapsulated resistive micromegas detectors for the upgrade of the t2k near detector time projection chambers," *Nucl. Instrum. Meth. A*, vol. 1056, p. 168 534, 2023. DOI: 10.1016/j.nima.2023.168534. arXiv: 2303.04481.

[41] S. Martoiu *et al.*, "Front-end electronics for the scalable readout system of rd51," pp. 2036–2038, 2011. DOI: 10.1109/NSSMIC.2011.6154414.

[42] M. J. French *et al.*, "Design and results from the apv25, a deep sub-micron cmos front-end chip for the cms tracker," *Nuclear Instruments and Methods in Physics Research Section A: Accelerators, Spectrometers, Detectors and Associated Equipment*, vol. 466, no. 2, pp. 359–365, Jul. 2001, ISSN: 0168-9002. DOI: 10.1016/S0168-9002(01)00589-7.

[43] S. Martoiu *et al.*, "Development of the scalable readout system for micro-pattern gas detectors and other applications," *Journal of Instrumentation*, vol. 8, no. 03, p. C03015, Mar. 2013. DOI: 10.1088/1748-0221/8/03/C03015. [Online]. Available: https://dx.doi.org/10.1088/1748-0221/8/03/C03015.

[44] G. d'Agostini *et al.*, *Laboratorio di Meccanica, Dispense A.A. 2021-2022*.

[45] E. Leonardi *et al.*, "Geant4-based full simulation of the padme experiment at the dane btf," *Journal of Physics: Conference Series*, vol. 898, no. 4, p. 042 025, Oct. 2017. DOI: 10.1088/1742-6596/898/4/042025. [Online]. Available: https://dx.doi.org/10.1088/1742-6596/898/4/042025.

[46] F. Bossi *et al.*, "The padme beam line monte carlo simulation," *JHEP*, vol. 09, p. 233, 2022. DOI: 10.1007/JHEP09(2022)233. arXiv: 2204.05616 [hep-ex].